An Insight into Gravitational Microlensing and the Search for Exoplanetary Systems

Giuseppe D'Ago

Physics department "E.R. Caianiello"

University of Salerno

Thesis submitted for the degree of

PhilosophiæDoctor

A.A. 2013/14

“Oh, let the sun beat down upon my face
With stars to fill my dream
I am a traveler of both time and space
To be where I have been”

Kashmir - Led Zeppelin

Contents

List of Figures

LIST OF FIGURES

List of Tables

LIST OF TABLES

Introduction

Nature always offers astonishing shows to the humankind. Gravitational lensing is one of the most intriguing effects which can be observed, and the astrophysical applications of such a phenomenon span from particle physics to cosmology, to the search for new worlds.

Although, since its formulation in the early 1900, gravitational lensing was underestimated and poorly investigated, in the last thirty years the observation of different phenomena related to gravitational lenses have revealed the real potentiality of the study of the effects of gravity on the light.

Our comprehension of the Universe has been largely improved since we have studied the cosmological implications of lensing by clusters of galaxies, lensing of quasars, or effects of microlensing by non-luminous objects. The structure of the Universe, constraints on its formation theories, the mass distribution, and even proofs of the nature of dark matter can be studied by investigating magnification patterns and the effects due to gravitational lenses.

Additionally, gravitational microlensing provides a unique tool to search for planetary systems in a region of the physical parameter space not probed by other methods. By observing microlensing effects to stars towards the Galactic bulge, we are able to look for small rocky planets orbiting stars in the Galactic disk or, more in general, along the line of sight. What we observe is the source lightcurve, i.e. the measured flux as a function of time. The presence of a foreground mass, or a system of masses, between the observer and a background source, causes an amplification of the source flux, so giving to the lightcurve specific features and shapes which can be attributed to different kinds of lens (single, binary, planetary, etc...). The study of this specific effect is likely to attain more promising results with the launch of space missions like EUCLID or WFIRST, since those telescopes will be able to detect Earth-like and smaller planets in their habitable zone, i.e. at a distance from their host star allowing the planet to have an equilibrium temperature at which liquid water can exist.

The first chapter of this thesis work is to introduce the reader to the physics and the geometry of gravitational microlensing. The terminology of the phenomenon will be presented and the different aspects and implications of the single lens and multiple lens as well will be treated.

The second chapter contains the original work at which this author has devoted his efforts during part of his graduate studies. The results achieved brought to the development of the first complete catalogue of the lightcurves arising from the microlensing by equal-mass binary systems. The work was aimed at probing the parameter space of the equal-mass binary lens and at classifying the variety of lightcurve morphologies which are theoretically observable when a source is magnified by such a lens. The final catalogue represents a unique tool for scientists working on modelling microlensing events, since it offers the possibility to set a reasonable and very efficient initial condition choice for the parameter space investigation.

The third chapter treats the use of microlensing as a method for searching new exoplanets, the phenomenology and a brief insight into the morphologies of lightcurves. We will also be speaking about the international community which participates in the observations and the importance of having an observing strategy which implies the use and the collaboration between several different observatories. Finally, we will present the Salerno University Observatory, explaining its role in the search for exoplanets, and give a brief summary of the events observed since 2012 to date.

In the fourth chapter we will be presenting the results of the analysis of an event from the 2013 observing season. OGLE-2013-BLG-1394 is an event we followed from our observatory and for which I am leading the modelling. By also making use of datasets from other telescopes, we found that the event was due to a binary source magnified by a single lens. High order effects due to the Earth motion (parallax) and to the relative motion between the two sources (xallarap) had to be taken into account for the correct fitting of the lightcurve.

The fifth chapter summarises the other methods used in order to discover and characterise new planets. Additionally, a brief summary of some exoplanets, characterised also by mean of transits observations which have been personally conducted by this author, will be presented.

The sixth chapter is left for final discussion and remarks.

1

Theory of gravitational microlensing

"This is Major Tom to Ground Control
I'm stepping through the door
And I'm floating in a most peculiar way
And the stars look very different today"

Space Oddity - David Bowie

1.1 Gravitational lensing basics

"*The refractivity necessary at every point of a gravitational field to produce the Einstein deflection is the ratio of the energy of a constant-mass particle fallen there from infinity to the energy of the same particle moving with the speed of light; but it is not permissible to say that the solar gravitational field acts like a lens, for it has no focal length*". This is what Sir Olvier J. Lodge stated in a Letter to Nature in 1919 (Lodge, 1919) at the dawn of the experimental verification by Prof. Eddington of Einstein's theory of General Relativity, about the light-path bending by the mass of the Sun, and it was the first time that the terms "gravitational" and "lens" were put together in print. *Gravitational lensing* is defined as the phenomenon of the light bending due to the gravitational field of a body. Since the deflection predicted by Einstein (1916) was $\hat{\alpha}(r) = 1''.75(M/M_{\odot})(R_{\odot}/r)$ (for a light ray passing at a distance r from a body with mass M), the gravitational field of the Sun was equivalent to a strongly astigmatic lens as the deflection depends on the inverse of the distance to the optical axis. The comment by Sir Lodge made indeed some sense, but it was just destined to be part of the big polemic born after the development of Einstein's theory and subsequent verifications.

It is fascinating to read along the *Discussion of the Theory of Relativity* (Eddington et al., 1919) arisen after the observation of the Sun total eclipse by Eddington on May 29, 1919, from Principe Island in the Gulf of Guinea, Western Africa (Eddington, 1919). At the same time, the eclipse was observed from Sobral, in Brazil. The results (Dyson et al., 1920) suprisingly verified Einsten's prediction, with a measured deflection angle of $1''.98 \pm 0''.18$ (Principe site) and $1''.61 \pm 0''.30$ (Sobral site). The discussion, after the evidence, was a struggle between the enthusiastic relativists and the community attached to the Netwtonian theory and the concept of ether, and the *Discussion* is a clear example of it.

Anyway, before Einstein, such phenomenon was studied by other scientists and philosophers (Valls-Gabaud, 2006). Newton first, in his *Opticks*, had proposed the idea: "*Do not the Rays of Light which fall upon Bodies begin to bend before they arrive at the Bodies?*" while he was investigating the diffraction. Documents by Henry Cavendish were found, where he stated "*To find the bending of a ray of light which passes near the surface of any body by the attraction of that body. Let* s *be the centre of the body and* a *a point of surface. Let the velocity of body revolving in a circle at a distance* as *from the body be equal to the velocity of light as* 1:u*, then will the sine of half bending of the ray be equal to* $1/(1 + u^2)$". Then, Cavendish was the first one who calculated the deflection angle of a light ray by making use of the Newtonian concept of gravity. This appears to be the first document that explicitly states that light could be bent by gravity, even if it was unpublished. The most famous calculation before Einstein was the one by Johann Soldner in 1801 (Soldner, 1801). He had found a deflection angle $\hat{\alpha} = 2GM/v^2 r$ (where v was the velocity of light) using the Newtonian theory and this yielded, for a ray grazing the Sun surface, $\hat{\alpha} = 0''.85$. The same wrong value was obtained by Einstein in a first attempt to calculate $\hat{\alpha}$ (Einstein, 1911). After the development of his theory of General Relativity, Einstein was able to calculate the correct value for $\hat{\alpha}$. The reason why Soldner's result was incorrect is because an additional factor of two arose when taking into account the spatial curvature which is not predicted by Newton's theory. The correct value obtained by Einstein for a ray grazing the Sun surface was (Einstein, 1916)

$$\hat{\alpha} = \frac{4GM_\odot}{c^2}\frac{1}{R_\odot} = 1''.75\,. \tag{1.1}$$

1.2 The lens equation

Microlensing occurs when a foreground star, or a discrete distribution of point-like objects, passes through the line of sight of a background source (which can also be a multiple system,

as we will see later).

To understand gravitational microlensing, a correct approach is to start with the simplest case of the single lens. In Figure 1.1 we describe the geometry of the system and we show how a foreground body with mass M acts like a lens (L) for a light ray emitted by a background source (S) passing at a distance r (or impact parameter) from the lens and received by the observer (O). Characteristic distances are defined as D_S (between source plane and observer plane), D_{LS} (between lens plane and source plane), and D_L (between lens plane and observer plane).

The physics of the lens lies in the equation

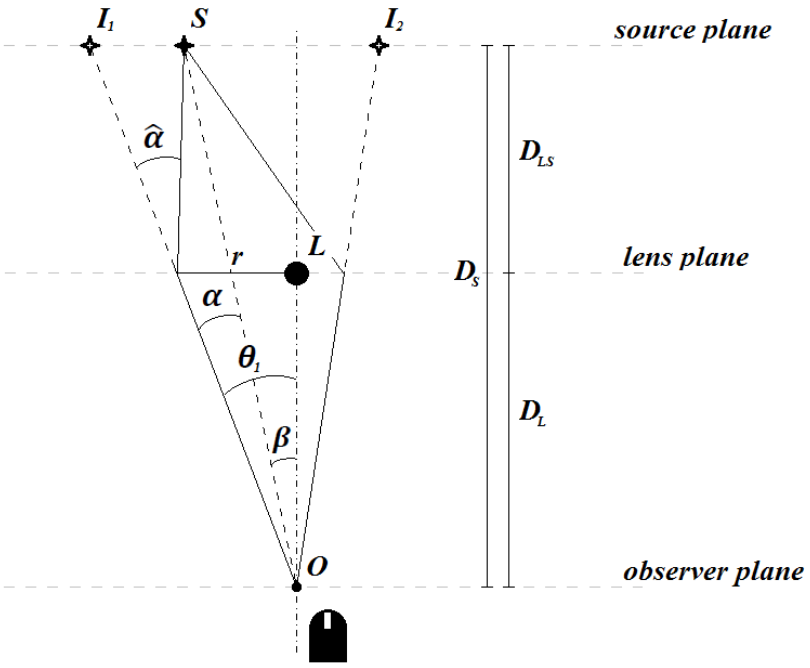

Figure 1.1: The scheme reproduces the geometry of the single lens microlensing. The dot-dashed line indicates the lens-observer axis, while dashed lines indicate the apparent light path of images $I_{1,2}$ and the source real position S. Solid lines draw the light path bent by the gravitational field of the lens L.

$$\theta D_L = \beta D_S + \hat{\alpha} D_{LS} \,, \tag{1.2}$$

where θ is the image position (the angular position where the source is observed), β is the actual angular position of the source, and $\hat{\alpha}$ is the deflection angle as in Equation (1.1), which

is generally defined by

$$\hat{\alpha} = \frac{4GM}{c^2}\frac{1}{r} \,. \tag{1.3}$$

Equation (1.2) is true for $\hat{\alpha} \ll 1$ and in the thin-lens approximation (i.e. the case where, given the typical distance scale, all the deflection can be assumed to occur in the lens plane, because the thickness of the lens is negligible compared to D_L, D_S, and D_{LS}). By using the relation between the impact parameter and the image position, $r = \theta D_L$, from Equations (1.2) and (1.3) it is possible to find the function $\beta(\theta)$

$$\beta(\theta) = \theta - \frac{D_{LS}}{D_L D_S}\frac{4GM}{c^2\theta} \,, \tag{1.4}$$

which, by defining the reduced deflection angle $\alpha(\theta) = \hat{\alpha} D_{LS}/D_S$, yields the lens equation

$$\beta(\theta) = \theta - \alpha(\theta) \,. \tag{1.5}$$

In the simplest case of perfect alignment between source, lens, and observer, $\beta = 0$ and the Equation (1.4) lead to define the *Einstein radius*

$$\theta_E \equiv \sqrt{\frac{D_{LS}}{D_S D_L}\frac{4GM}{c^2}} \,, \tag{1.6}$$

that is the radius of the so called *Einstein ring*. Even if not in the regime of microlensing, Figure 1.2 shows some examples of observed Einstein rings. Anyway, when the source is displaced by the distance β and writing all the angles in Einstein radius units, the lens equation takes the form

$$\theta^2 - \beta\theta - \theta_E^2 = 0 \,, \tag{1.7}$$

and can be solved for θ, giving the position where the images are formed:

$$\theta_{1,2} = \frac{\beta}{2} \pm \theta_E \sqrt{1 + \frac{\beta^2}{4\theta_E^2}} \,. \tag{1.8}$$

Both images lie along the line in the sky determined by the source and the lens positions and at opposite sides of the lens. The angular separation between the two images is given by

$$\Delta\theta = \theta_1 - \theta_2 = 2\theta_E \sqrt{1 + \frac{\beta^2}{4\theta_E^2}} \,, \tag{1.9}$$

which corresponds approximately to $2\theta_E$ for sources lying close to the lens-observer axis ($\beta < \theta_E$). Figure 1.3 describes the lensing by a single point-like lens. With typical Galactic distance

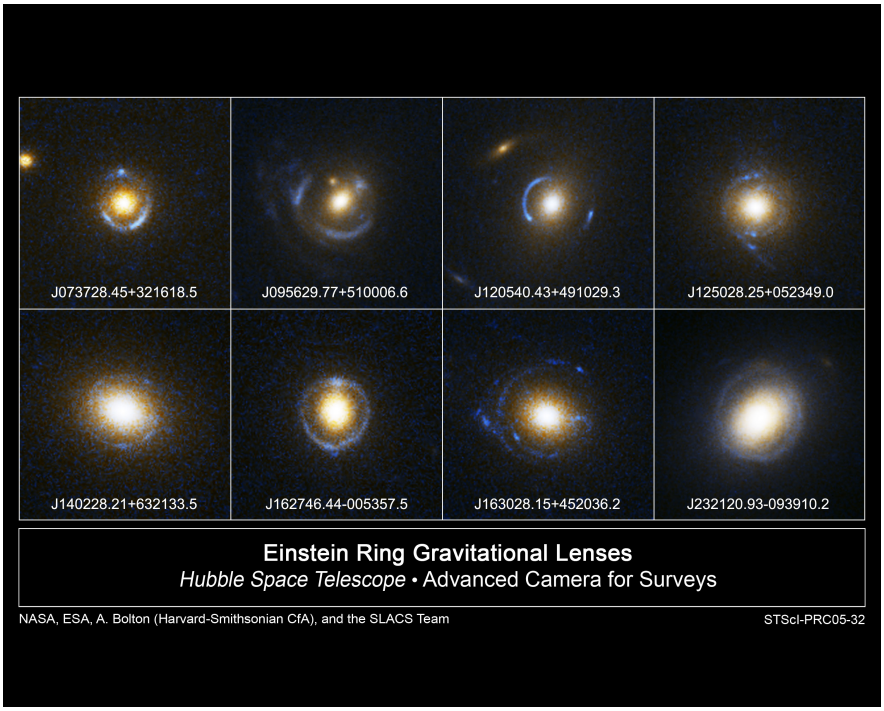

Figure 1.2: Examples of Einstein rings observed in the regime of strong lensing.

scales, an estimate of the Einstein angle is

$$\theta_E = 0.9 \text{ mas} \sqrt{\frac{D_{LS}}{D_L D_S} \frac{10 \text{ kpc}}{M_\odot} M}, \tag{1.10}$$

and it is clear that, if a star in the Galactic Bulge is lensed by a foreground star, the separation between the two images is impossible to be resolved with ground based and space telescopes, since the best resolution achieved to date for optical telescope is 0.1 arcsecs (Hubble Space Telescope). Any event in which lensing occurs and there is no way to resolve the produced images is classified as microlensing. Depending on the geometry of the system or on the mass and the nature of the lens, different typical effects, like *arcs*, *rings*, can be produced and are observable. Even multiple images of quasars are observable (one example is the Einstein cross). These cases fall in the macrolensing regime and will be not treated in this thesis.

1.2.1 Single lens amplification: the Paczyński curve

Microlensing is observed as the amplification of the flux of the source star. The plot of the flux as a function of the time is called Paczyński curve (Paczyński, 1986), and it is a bell-shaped

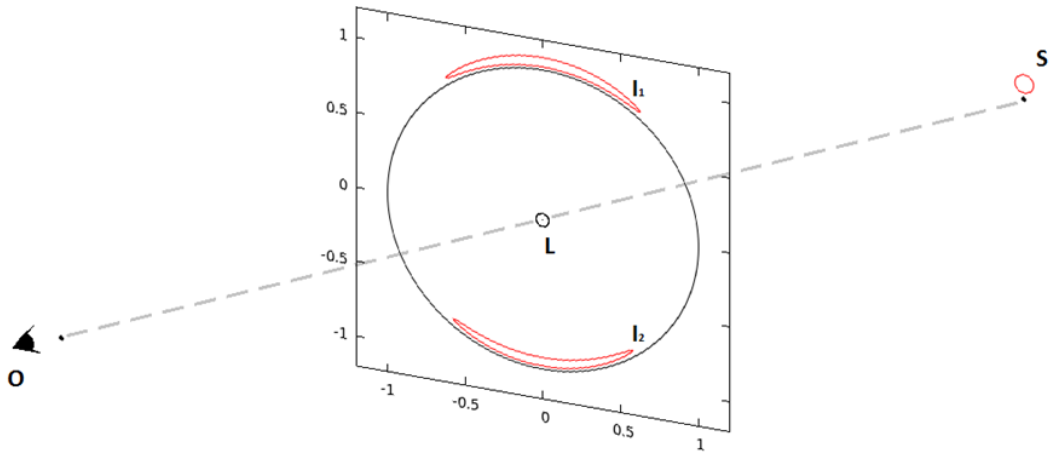

Figure 1.3: Production of images due to the presence of a single lens. The source plane is on the right, where the source contour is indicated by the red circle, and the lens plane is at the centre of the picture. The two images (red contour) lie one opposite to the other with respect to the lens and close to the Einstein ring (the black circle in the lens plane). Units are in Einstein angles.

curve, first analitically found by Einstein (1936), with the maximum at the time of closest angular approach between lens and source.

As a consequence of the Liouville theorem, applied to the photon beam emitted by the source, the surface brigthness along the trajectory light is conserved. Considering the fact that the differential deflection of light rays changes the shape and the solid angle ($d\Omega_0$) that a given source subtends, and since the flux received by the observer is the product of the surface brightness and the solid angle ($d\Omega$) on the lens plane, the result is that the flux emitted by the source is amplified, and it can be evaluated for each image as (see Mollerach &Roulet, 2002, for a rigorous derivation)

$$A_{1,2} = \frac{d\Omega_{1,2}}{d\Omega} = \frac{\theta_{1,2}}{\beta}\frac{d\theta_{1,2}}{d\beta} = \frac{1}{2} \pm \frac{\beta^2 + 2\theta_E^2}{2\beta\sqrt{\beta^2 + 4\theta_E^2}} . \tag{1.11}$$

Images 1 and 2 are said to have opposite *parity*. In fact, for the image appearing on the opposite side of the lens, at the angle θ_2, the ratio $d\Omega/d\Omega_0$ is negative. This means that the image is inverted and has negative parity. The total amplification is obtained by adding the absolute values of the magnification of the two images:

$$A = |A_1| + |A_2| = \frac{\beta^2 + 2\theta_E^2}{\beta\sqrt{\beta^2 + 4\theta_E^2}} . \tag{1.12}$$

If one defines the coordinates $u = \frac{\beta}{\theta_E}$ and $y = \frac{\theta}{\theta_E}$ as the dimensionless position of the source and the lens in Einstein radius unit, respectively, the lens equation takes the simple form

$$u = y - \frac{1}{y}\,, \tag{1.13}$$

and the total amplification can be written as a function of u and thus as a function of time, since the relative position between source and lens changes with time:

$$A(u) = \frac{u^2 + 2}{u\sqrt{u^2 + 4}}\,, \tag{1.14}$$

while

$$u(t) = \sqrt{u_0^2 + \left(\frac{t - t_0}{t_E}\right)^2}\,. \tag{1.15}$$

Equations (1.14) and (1.15) give the analytical form for the Paczyński curve (Figure 1.4). u_0 is the impact parameter at the time t_0 of maximum angular approach between lens and source, and t_E is the time needed by the source to draw one Einstein radius θ_E. t_E is called Einstein time and it is defined as $t_E \equiv \frac{\theta_E}{\mu_{rel}}$, where μ_{rel} is the lens-source relative proper motion.

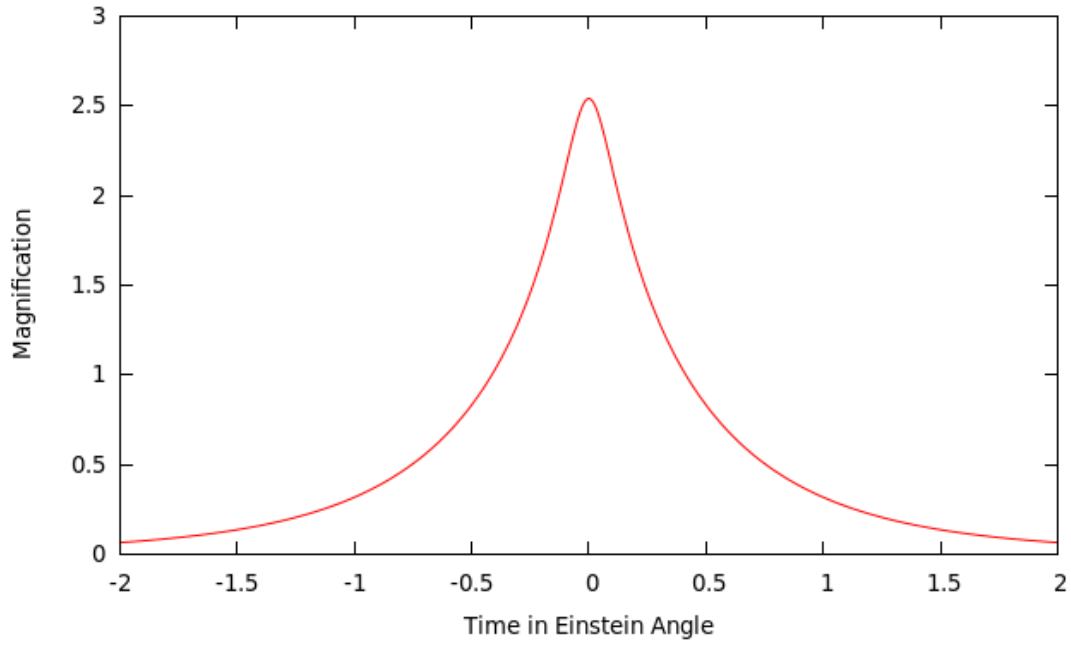

Figure 1.4: Paczyński curve for the lens system shown in Figure 1.3.

1.3 Binary and multiple lenses

When dealing with multiple lenses it is impossible to exploit the central simmetry which is valid in the case of the single lens. The lens equation has to be written in its vectorial form

$$\vec{\beta} = \vec{\theta} - \vec{\alpha}(\vec{\theta}) \,, \tag{1.16}$$

where $\vec{\alpha}(\vec{\theta})$ depends on the number N of the lenses and it is the sum of the effects of every single mass composing the lens:

$$\vec{\alpha}(\vec{\theta}) = \frac{4G}{c^2}\frac{D_S D_L}{D_{LS}} \sum_i^N m_i \frac{\vec{\theta} - \vec{\theta}_{m,i}}{|\vec{\theta} - \vec{\theta}_{m,i}|^2} \,. \tag{1.17}$$

Equation (1.17) (Schneider et al., 1992; Petters et al., 2001) is true when the lenses are static and their distribution along the line of sight is small in comparison with D_L, D_S, and D_{LS}. Masses and angular positions of the lenses are respectively m_i and $\theta_{m,i}$. As a consequence, the dimensionless positions of source and lens are $\vec{u} = (u_1, u_2)$ and $\vec{y} = (y_1, y_2)$, respectively. The components of $\vec{u}$ and $\vec{y}$ will be used, from now on, for all the two-dimensional plots depicting the lens and the source plane in dimensionless units.

It is convenient to define the complex coordinates (see Witt, 1990) as $\zeta = u_1 + iu_2$ and $z = y_1 + iy_2$ by using the components of u and y and write the lens equation as

$$\zeta = z - \sum_i^N \frac{\epsilon_i}{\bar{z} - \bar{z}_{m,i}} \,, \tag{1.18}$$

where $\epsilon_i = \frac{m_i}{\sum_i^N m_i}$ and $z_{m,i}$ is the position of the mass m_i.

1.3.1 Amplification

The vectorial lens equation (1.16) describes a two-dimensional mapping between the position of the images $\vec{\theta}$ and the actual position of the source $\vec{\beta}$. The amplification has been defined as the ratio of the solid angles at the source plane and at the lens plane, and by defining the Jacobian of the mapping as $J = \det(\partial\vec{\beta}/\partial\vec{\theta})$, it is also possible to relate a solid angle $\mathrm{d}\Omega_0$ in the source plane with the corresponding $\mathrm{d}\Omega$ in the lens plane, via the equation (Mollerach &Roulet, 2002)

$$\mathrm{d}\Omega = \frac{1}{J}\mathrm{d}\Omega_0 \,, \tag{1.19}$$

where the inverse of the Jacobian quantifies the amplification. When writing the lens equation in complex coordinates, the Jacobian becomes (Witt, 1990)

$$J = 1 - \frac{\partial\zeta}{\partial\bar{z}}\frac{\partial\bar{\zeta}}{\partial z}\,, \tag{1.20}$$

the amplification at the position z_j is given by

$$A_j = \frac{1}{J}\,, \tag{1.21}$$

while the total amplification is given, as for Equation (1.12), by the sum of the absolute value of the amplification of each image, $A = \sum_j |A_j|$.

As one can notice from Equation (1.21), there are specific positions z_j in the lens plane, at which the Jacobian is equal to zero and, then, the amplification diverges to infinite values. Those position in the lens plane are called *critical curves*, while the corresponding lines in the source plane are called *caustic curves* or *caustics*. The caustics are made up of regular curved lines called folds, connected by cusps (points in which the tangent vector vanishes). When the source enters a caustic, a new pair of images is produced. On the other hand, when it exits a caustic, two images are destroyed. In the case of the single lens, the caustic is just a point behind the lens, while the critical curve is the Einstein ring, and there are only two images which lie close to the ring. Thus, the amplification diverges when $u = 0$.

Figure 1.5 shows the images formation for a given source track in the case of the equal-mass binary lens. The corresponding lightcurve is in Figure 1.6.

The amplification tends to infinity only for poink-like sources. The extended size of the source causes a smoothing of the peaks of the lightcurve. This is called *finite-source effect* and, when it occurs, it is possible to retrieve more information about the lens system. High-order effects will be treated in the following sections and, from now on, only the finite source case will be considered.

1.3.2 Binary lens

When the lens consists of two point-like masses, the lens equation is (Witt &Mao, 1995)

$$\zeta = z - \frac{\epsilon_1}{\bar{z} - \bar{z}_{m,1}} - \frac{\epsilon_2}{\bar{z} - \bar{z}_{m,2}}\,, \tag{1.22}$$

which can be recast into a fifth-order complex polynomial in z that cannot be solved analitically. By using Laguerre's method it is possible to find the polynomial roots which, in the (complex)

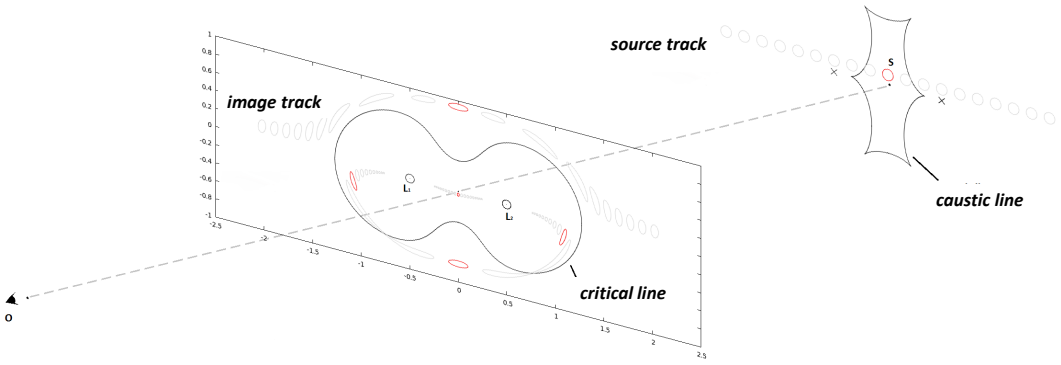

Figure 1.5: The scheme shows the five lensed images of the source as it moves on a linear path in the source plane. Source position (right side of the picture) and the corresponding five images (on the centre of the picture) are highlighted in red.

image plane, represent the image positions. Although, not all roots of the polynomial always represent a real image:

- when the source is outside the caustic, three lensed images are produced; this means that only three roots out of five are also solution of the lens equation;
- when the source is inside the caustic, all the five roots of the complex polynomial satisfy the lens equation and thus represent real image positions.

The simplest case is the one with a static distribution of the masses. In this thesis, and for the morphological classification of binary lightcurves, the binary lens and its interaction with the source are described by seven parameters:

1. the separation s between the two masses;
2. the mass ratio q between the lenses;
3. the distance u_0 of maximum approach between the source and the centre of mass of the lens;
4. the angle α_0 between the source trajectory and the lens axis;
5. the source radius ρ_*;

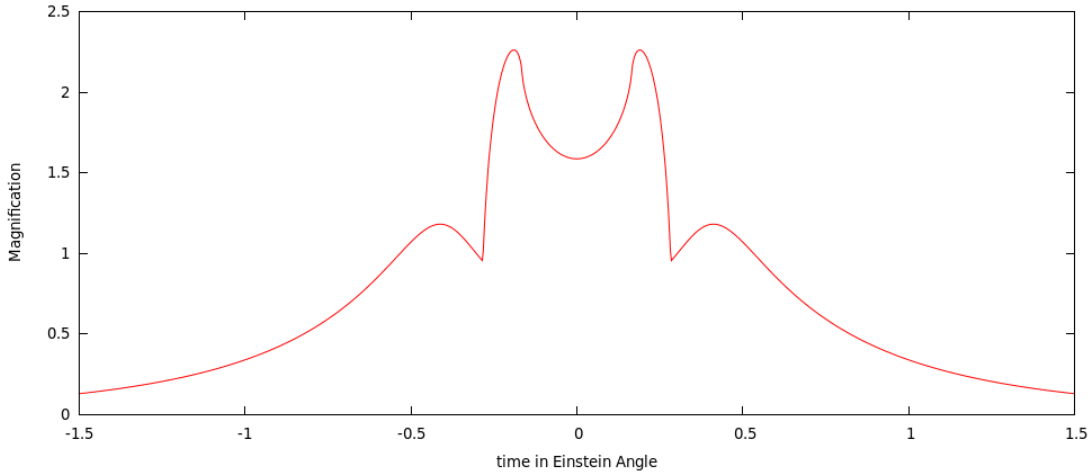

Figure 1.6: The lightcurve of an equal-mass binary microlensing event. The source is moving parallel to the lens axis as in Figure 1.5.

6. the Einstein time t_E, which indicates the duration of the microlensing event;

7. the time t_0 of maximum approach, which for a single lens means the time of the peak, in the case of multiple lenses it can take different meanings (i.e. the time corresponding to u_0).

The parameters s and q define the intrinsic topology of the lens, while the interaction between the source and the lens, and so the resulting lightcurve, depends on u_0, α_0, and ρ_*. All the angular parameters, except for α_0, are in units of θ_E. An example of the equal mass binary lens is in Figure 1.7.

Even if we do not have a single lens, in the case of binary or multiple lenses Einstein radius and Einstein time as well can be normalised according to the particular system. For example, the origin for the binary lens can be chosen as the centre of mass of the system or, when considering a lens consisting in a planetary system, the optimal choice is to fix the origin as the position of the host star and to normalise θ_E with the total mass of the system (Dominik, 1999b).

The parameters describing the non-static behaviour of the lens, like parallax and orbital motion effects, will be treated theoretically in the following sections and practically in the chapters dedicated to the modelling and to the event OB131394.

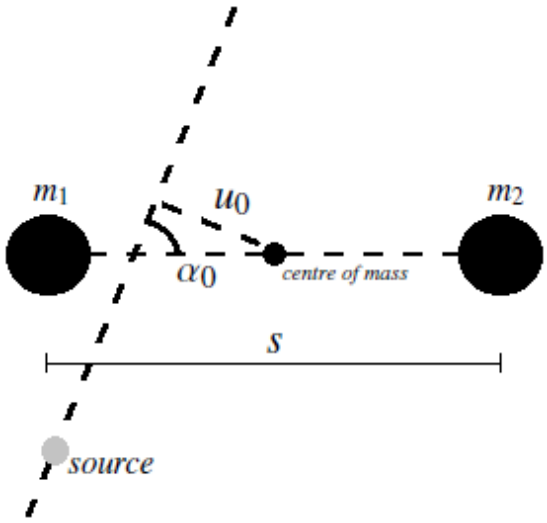

Figure 1.7: The geometry of the lens system, as will be treated in this work.

1.3.2.1 Topologies

The critical curve topology is characterised by s and q. The caustics of the binary lens appear as one to three non self-intersecting curves. According to the separation and the mass ratio, it is possible to individuate three different topologies: close, intermediate or resonant, and wide. For a fixed mass ratio, s_c and s_w represent the separations where the transitions from close towards wide topology occur (Erdl &Schneider, 1993; Dominik, 1999b):

$$\frac{q}{(1+q)^2} = \frac{(1-s_c^4)^3}{27 s_c^8}\,, \tag{1.23}$$

$$s_w = \sqrt{\frac{(1+q^{1/3})^3}{1+q}}\,. \tag{1.24}$$

The three topologies of the equal-mass binary lens are shown in Figure 1.8 and we will refer to them in the following chapters, when we present the morphological classification. For this kind of lens, $q = 1$ and the transition values are $s_c = \sqrt{2}/2$ and $s_w = 2$.

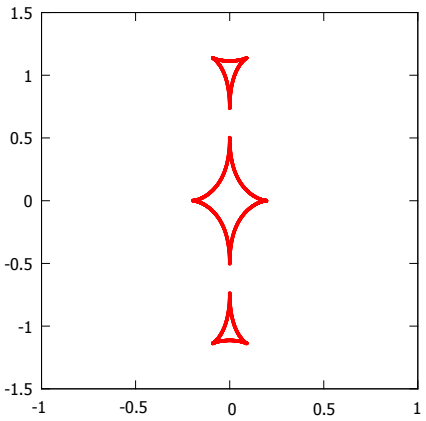

(a) Close topology caustic

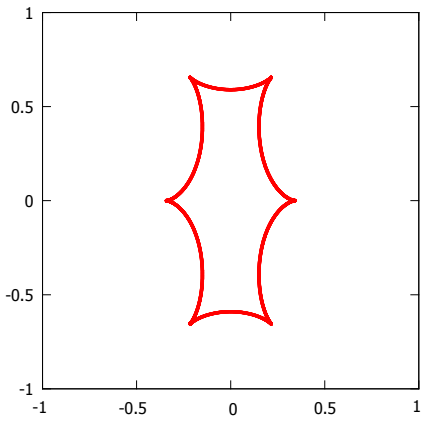

(b) Intermediate topology caustic

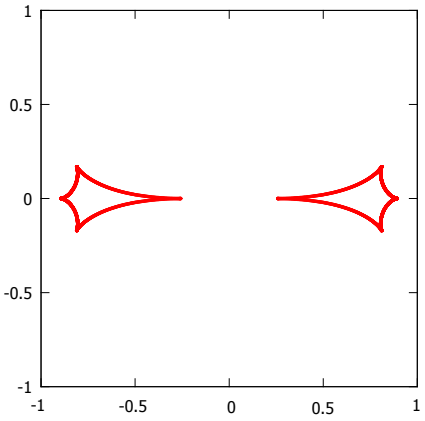

(c) Wide topology caustic

Figure 1.8: The three possible topologies of the equal-mass binary lens.

1.3.2.2 High-order effects

Several effects can affect the shape of the lightcurve. Here, the most important are briefly summarised.

- ***Limb darkening***
  When the source crosses a caustic, microlensing can also provide limb darkening measurements of distant stars. If the caustic crossing is well sampled, since different part of the star's surface are amplified at different times, changes in the amplification during the caustic crossing can be appreciated, and the surface brightness profile can be recovered.

- ***Parallax***
  When the duration of the events is longer than a month, the relative motion Earth-lens can be significant for the shape of the lightcurve since the Earth deviates from a rectilinear and uniform motion. The effect is proportional to the parallax $\pi_E = \theta_E \frac{\mathrm{AU}c^2}{4GM}$, and it is observable if π_E is not much smaller than unity.

- ***Orbital motion***
  The effect of the intrinsic Keplerian motion of the lens masses in binary or multiple systems results in changing the shape and rotating the magnification pattern (Section 1.3.4), thus perturbing the shape of the lightcurve from the static case.

- ***Binary source***
  The lightcurve deviates from the typical Paczyński curve not only when the lens consists of two masses but also when the source belongs to a binary system and the effect is observable when the source companion is significantly magnified by the lens. The two isolated Paczyński curves superpose each other in order to give the resulting lightcurve.

- ***Xallarap***
  The name arises from the fact that when the source is orbiting an unseen companion, the perturbation on the lightcurve mimics the one produced by the parallax.

1.3.3 Multiple lenses

For more than two lenses, the mathematics becomes really hard to deal with. Additionally, even finding a way to identify a topological characterisation is not a simple task, since the caustics are self-intersecting and draw really complex patterns.

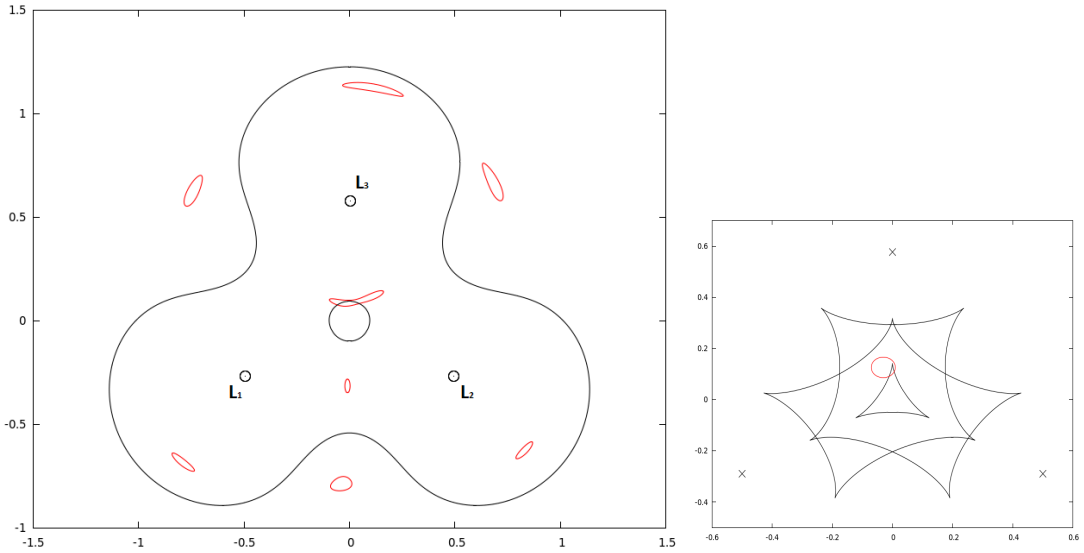

Figure 1.9: The lens plane and the source plane of an equal-mass triple lens (X and Y axes are in Einstein angle units). *The panel on the left shows the critical curves:* the lensed images are in red, while the circled dots indicate the position of the lenses. *The panel on the right shows the caustics pattern:* the crosses indicates the projected position of the lenses, while the source contour is the red circle.

Figure 1.9 shows an example of caustics and critical curves for an equal-mass triple lens and the lensed images pattern, while in Figure 1.10 we have an example of lightcurve. In this case, the complex polynomial arising from the lens equation has ten roots. This implies the possibility to have ten different images of the same source, when it is inside the innermost caustics. The triple lens is the last case in which the number of the roots can be equal to the number of the real images. For $N > 2$ the general rule is that the maximum number of images is $5(N - 1)$ (Rhie, 2002, 2003).

1.3.4 Magnification maps

In 1986, Kayser, Refsdal and Stabell indroduced the inverse ray tracing method in order to study the amplification as a function of the source position (Kayser et al., 1986). The method is used in particular for a large distribution of lenses, but it can be also used to study single and binary lenses as well. The principle of the method, also called *Inverse Ray Shooting* is to "shoot" a large amount of rays back from the observer to the lens plane and then to the source plane, in order to retrieve those source position where the rays concentrate. Such positions are

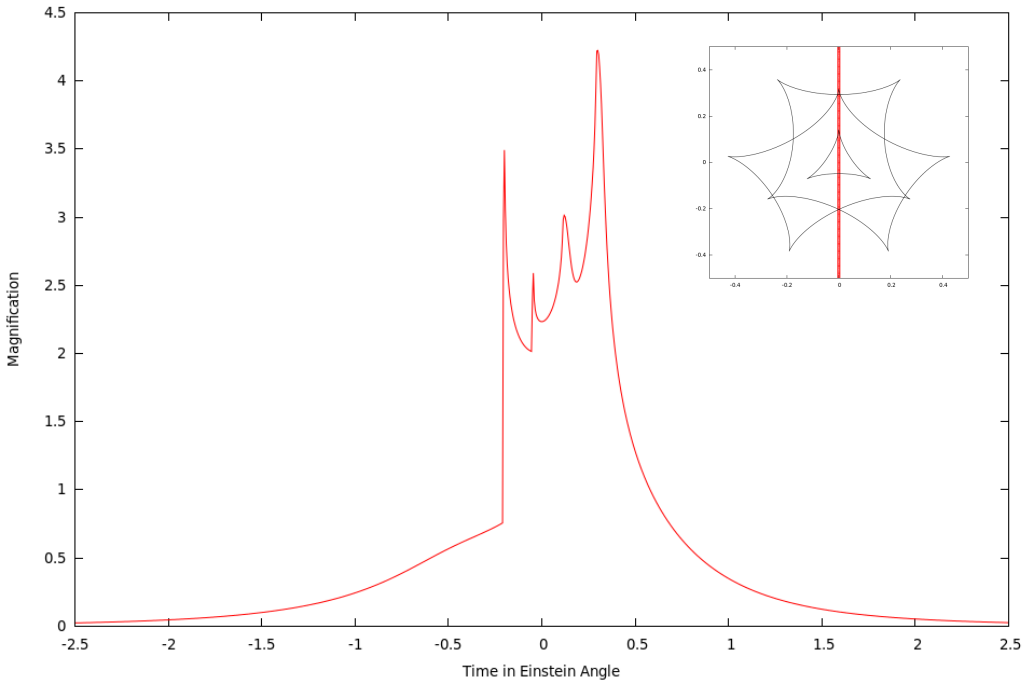

Figure 1.10: The lightcurve of an equal-mass triple lens microlensing event. The simulated lightcurve arises from the source track shown in the upper-right panel.

those corresponding to strong amplification. The result is a well-defined pattern in the source plane, resembling the caustic curves as shown in Figure 1.11 for the equal mass binary lens in intermediate topology.

Those patterns are called *magnification patterns* or *magnification maps*. They are three-dimensional maps in the source plane, with the third coordinate giving the number of the incident rays shot from the lens plane. This method requires powerful machines and long computational time depending on the number of the lenses and according to the resolution that one wants to achieve.

In this thesis, different techniques are used for simulating the lightcurves. For the classification, we used an inverse ray shooting code by Marnach (2010) in order to produce magnification maps and lightcurves; for the simulation of the examples shown so far for single, binary and triple lens, and for the following examples, a contour integration code developed by the author has been used; furthermore, for modelling OGLE-2013-BLG-1394, the contour integration code used is by Bozza (2010).

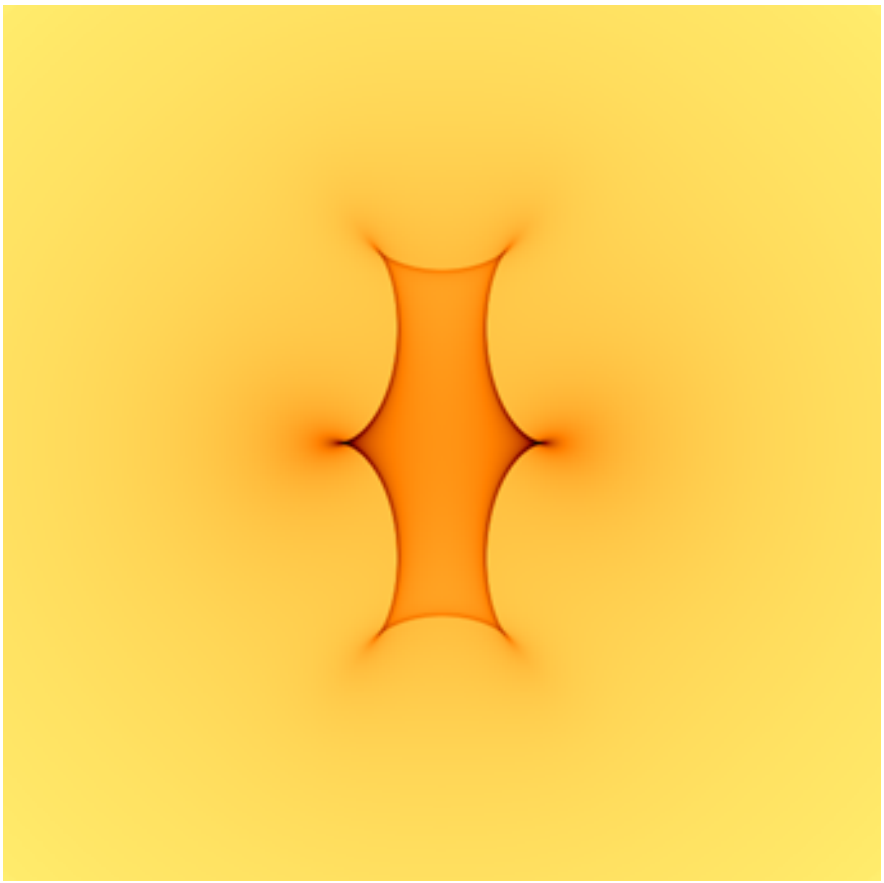

Figure 1.11: Magnification map for an equal-mass binary lens in the case of intermediate topology ($q = 1, s = 1$).

2

Lightcurve classification

"Starlight
I will be chasing a starlight
Until the end of my life"
Starlight - Muse

2.1 Motivation of the work

In order to extract the physics underlying a microlensing event, it is necessary to fit the observed lightcurve with the best model, i.e. the one which minimises the χ^2. The modelling process can be extremely hard and time-consuming as the investigation of the parameter space can require a huge effort if there is no idea of the regions of the parameter space in which the analysis has to be focused.

In the chapter dedicated to the modelling we will talk about Markov Chain Monte Carlo (MCMC), as it is the most common tool used for modelling microlensing events. Briefly, the process aims at probing the parameter space of the lens, which can be a simple 3-dimensional space, in the case of a static single lens, or even a 12-dimensional (or a more complex) space, if we consider the case of a binary lens with high order effects or more complicated systems like triple lens and beyond. The task of the modeller is to find the point in the n-dimensional space which minimises the χ^2, and this can be accomplished by following different approaches, but the most effective way is to start from a set of points in the parameter space and initialise MCMCs in order to find the best fit model. The set of initial seeds should not be randomly generated, but a first rough analysis (like a very large MCMC, or even an inspection by eye, in some cases) of the lightcurve could give clues about the nature of the lens, giving the possibility

to individuate the most promising zones in the parameter space. Anyway, a knowledge of the morphological features of the lightcurves is certainly useful for those who want to model a microlensing event.

Literature contains several examples of studies on the specific morphological traits of microlensing lightcurves (Mao &Di Stefano, 1995; Dominik &Hirshfeld, 1996; Di Stefano &Perna, 1997; Albrow et al., 1999; Dominik, 1999a; Han, 2008). One work worth to mention is by Night, Di Stefano &Schwamb (2008). They made a broad distinction between *point lens like*, *smooth*, and *caustic crossing* lightcurves, by making use of an asymmetry parameter and a multi-peak parameter to characterise the deviations from the point lens form, and by identifying the caustic-crossing lightcurves as the ones which cannot be fitted by a point lens model with a least squares metric. Additionally, they evaluated the theoretically expected relative numbers of each type of binary events, finding that there should be more smoothly perturbed events than caustic crossing events. They draw the attention on how this result is in contrast with observed events, which are dominated by the caustic crossing type, and they address the motivation to blending effects or to the difficulty in recognising binary events out from those events which may have been identified and published as point lens.

Anyway, a work aimed at developing a complete catalogue for binary microlensing lightcurves has not been developed yet. I was involved in first person in such a classification, contained in Liebig et al. (2015). The work we are going to present is the first morphological classification ever done, and represents a unique tool for modellers, since it can be directly applied to observed lightcurves of equal-mass binary microlensing, and can represent a scheme that can be applied to any mass ratio, down to planetary ones. Additionally, our database can be used to individuate the more promising zones in the parameter space where the seeds for the MCMCs could be chosen.

For our purpose, we make use of a labelling of the caustics which can help the reader in the comprehension of the work. We also define building blocks for the lightcurve features and iso-peak regions in a well defined subset (α_0 and u_0) of the lens parameter space. The following sections will reproduce the work done step by step in order to achieve the complete classification.

2.2 Cusps and folds: how the source “interacts” with the caustics

The proper motion of the source involves the interaction with the caustics produced by the lens, and the effects are recognisable in the lightcurve as specific features. These features are peaks whose nature depends on the projected motion of the source in the lens plane which are classifiable as “grazing” or “crossing” a caustic. The grazing consists in the caustic approach with no overlap of the source surface on a fold or a cusp, while the crossing occurs when the source completely enters a caustic.

We have already defined cusps and folds in Section 1.3.1. The first step of our classification is to define a labelling for cusps and folds, in order to make the connection between the source trajectory and the features of the lightcurve clearer, and to keep track of the specific elements of the caustic involved in a particular microlensing event, unambiguously.

The labelling we are going to define is not affected by the transitions among the three topologies. We will always indicate a cusp with a capital letter, from “A” to “D”, and the folds with the lowercase letters “a” and “b”. We distinguish the left side from the right side of the source plane by using respectively the numbers “1” and “2”, while the letters “b” and “t” are used in order to indicate the bottom side and the top side of the source plane, respectively. One specific fold or one specific cusp will be identified by a combination of the letters and the numbers described just above as e.g. A_1 or b_{t2}. Figures 2.1 to 2.3 show how the resulting labelling of the caustics appears in the three topologies (see Section 1.3.2.1).

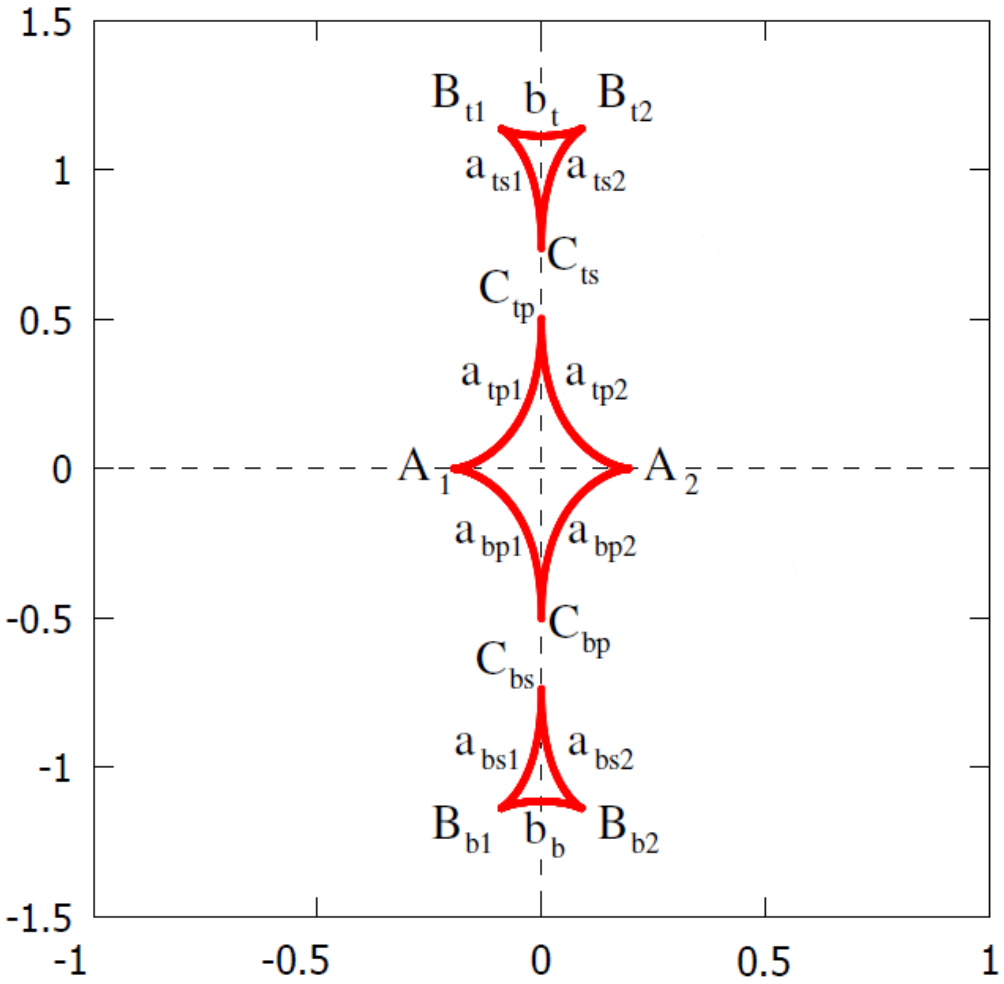

Figure 2.1: The caustic labelling for the close topology

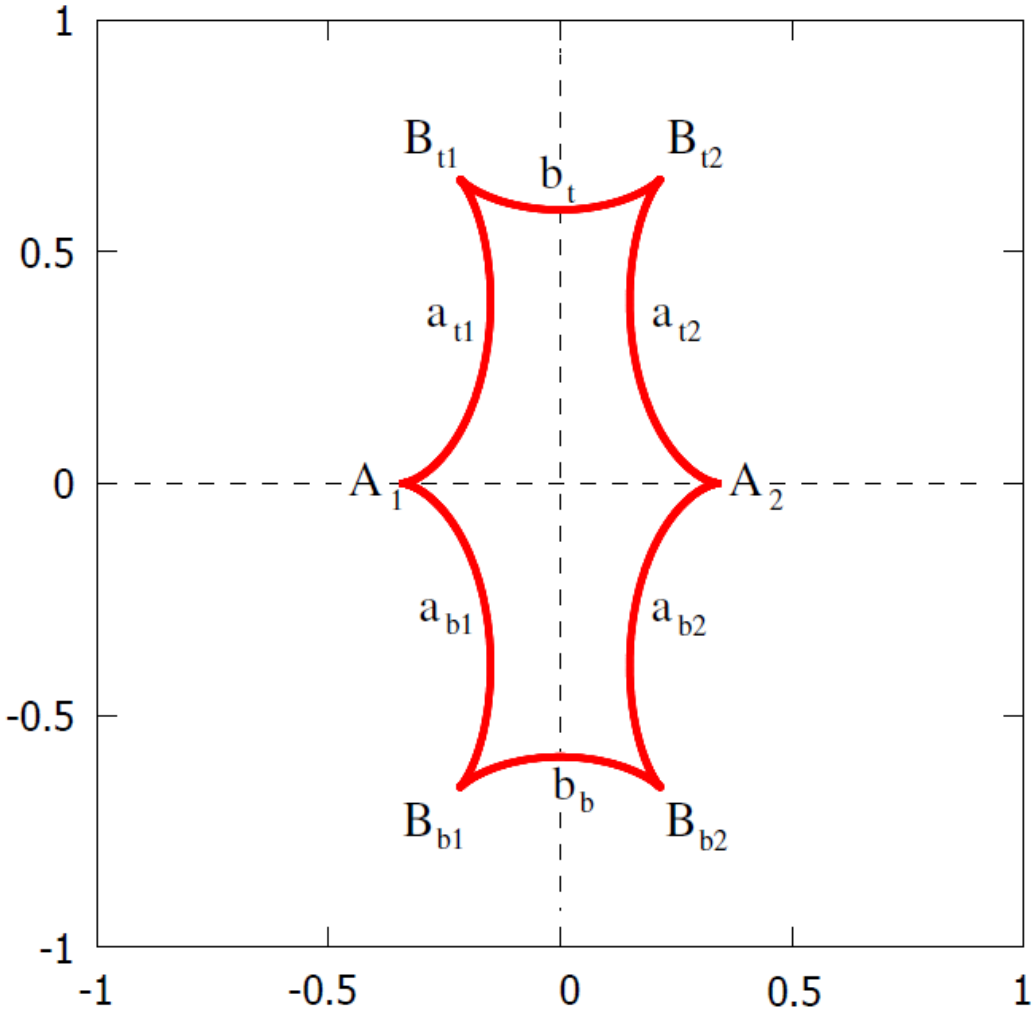

Figure 2.2: The caustic labelling for the intermediate topology

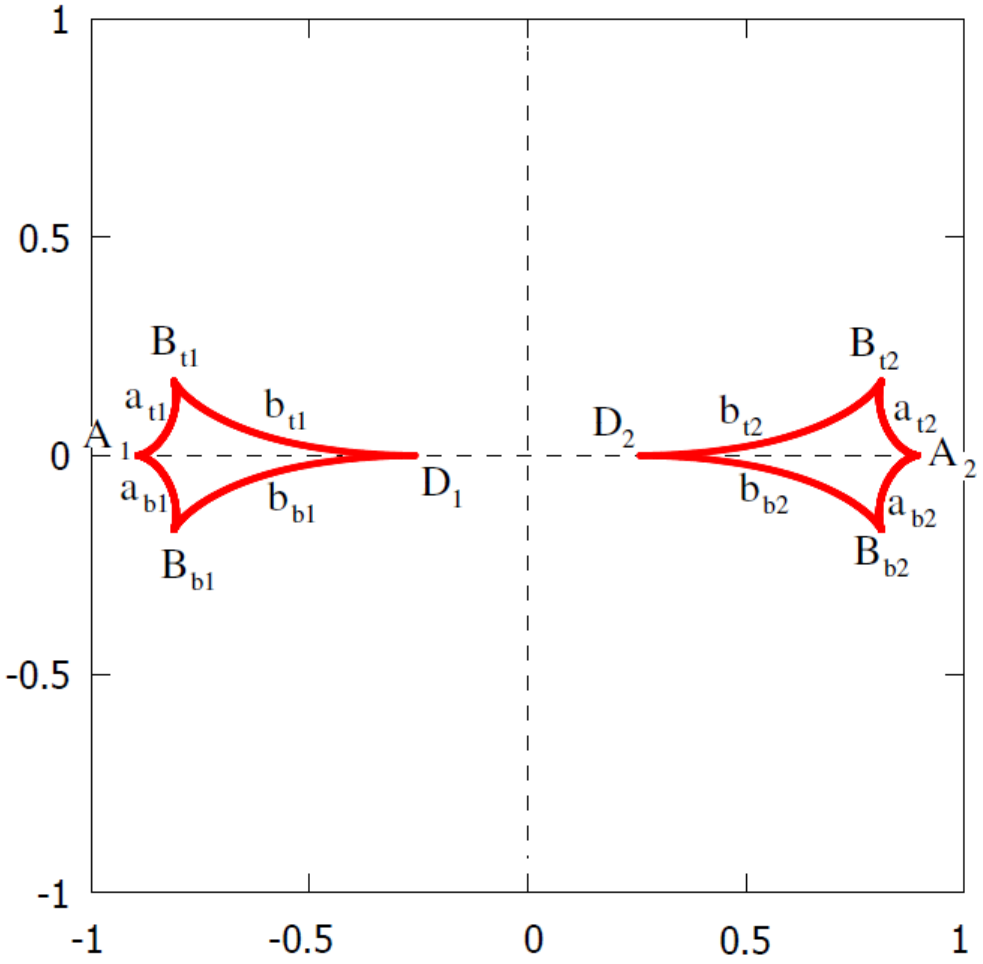

Figure 2.3: The caustic labelling for the wide topology

In order to classify the lightcurves we need to associate the source track with the features that cause that specific peak sequence. A source track is identified by the sequence of the folds and cusps the source interacts with. The entry in and the exit from a caustic are indicated by the square brackets “[” and “]” respectively, while, outside the brackets, the capital letters indicate the cusps grazing. For the mass ratio we are considering, due to the shape of the caustics, the fold grazing can only occur inside a caustic. Two examples below show the classification of source tracks resembling the caustic feature sequence of a lightcurve.

- **$A_1[a_{bp1}b_{tp2}]A_2$** This is the case of a four-peak lightcurve in the close topology. The source grazes the cusp A_1 on the lower left of the source plane and enters the caustic, crossing the fold a_{bp1}. Then, the source exits the caustic via the fold b_{tp2} and finally grazes the cusp A_2 on the upper right side of the plane (Figure 2.4);

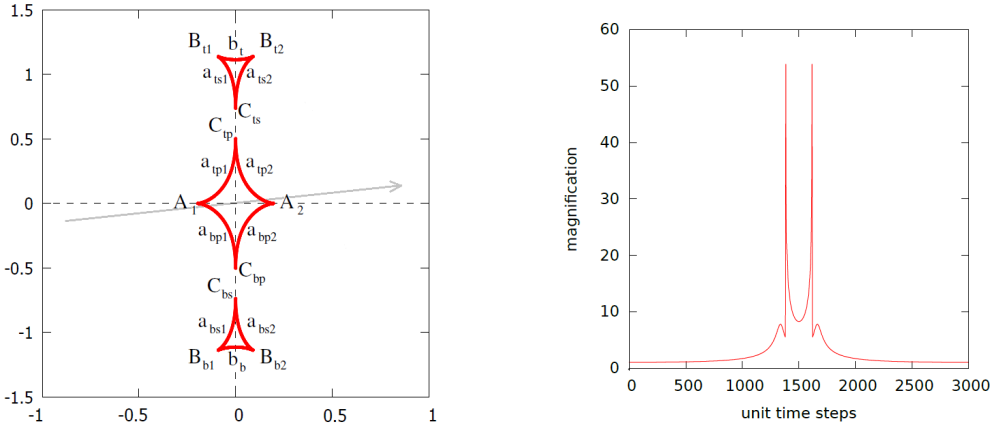

(a) Source crossing the primary caustic in the close topology: outside the caustic, before and after the fold crossings, two cusp grazings occur.

(b) The four-peak lightcurve, corresponding to the source path shown on the lefft, belongs to the morphology class $\bar{C}$ F-F $\bar{C}$, one of the classes with the highest occurence.

Figure 2.4: Source track and corresponding lightcurve for the close topology.

- **$[a_{b1}a_{t1}b_t]B_{t2}$** This is the case of a four-peak lightcurve in the intermediate topology. The source crosses the fold a_{b1} on the lower right of the plane, then we have the a_{t1} (upper left) inner grazing and the exit occurs via the fold b_t on the upper side of the plane. The last peak is due to the B_{t2} cusp grazing on the upper right of the plane (Figure 2.5).

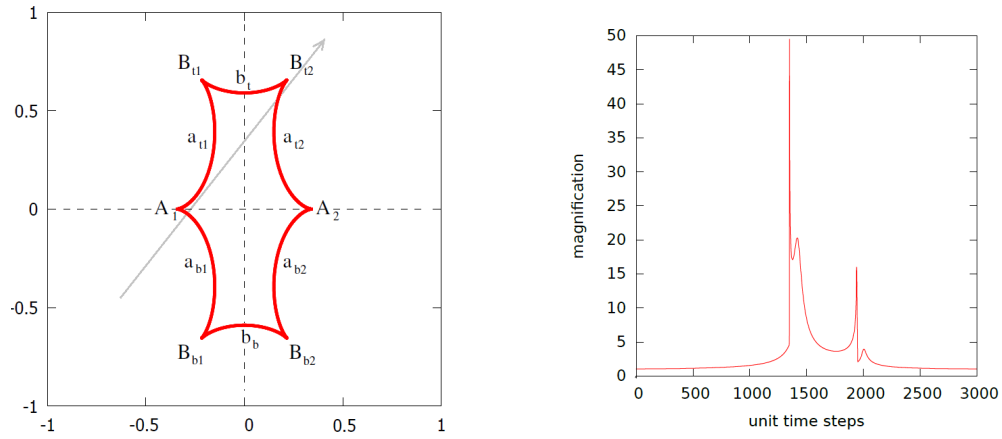

(a) Source crossing the primary caustic in the close topology: outside the caustic, before and after the fold crossings, two cusps grazing occur.

(b) The lightcurve for this specific source path (*left panel*) shows the peak due to the fold grazing, which is possible only when the source passes inside the caustic; the lightcurve shown belongs to the morphology class F-$\bar{\text{F}}$-F $\bar{\text{C}}$.

Figure 2.5: Source track and corresponding lightcurve for the intermediate topology.

2.3 The morphology classes: how to translate the caustic-source interaction into lightcurve features

After defining the syntax in use for the source tracks, we have to define *building blocks* in order to "read" the lightcurves and in order to perform a census of the morphologies. Building blocks define the four features, which can be found in the lightcurve, identifying the nature of the peaks (Figure 2.6):

- **F-** and **-F** indicate a caustic entry and a caustic exit, respectively, via a fold (*fold crossing*). In the first case, the lightcurve will show an abrupt vertical rise followed by a smoother fall, while in the case of the exit, the lightcurve shows a smooth rise followed by a vetical drop (Figure 2.6(a));
- **C-** and **-C** indicate a caustic entry and a caustic exit via a cusp (*cusp crossing*) with a steep rise followed by a symmetric descent (Figure 2.6(b));
- $\bar{\text{C}}$ indicates the *cusp grazing*. The peak is smooth and consists of a rise followed by a symmetric fall (Figure 2.6(c));

- **-$\bar{\text{F}}$-** indicates the rare case of a *fold grazing*, which can only occur when the source is inside a caustic. The peak is smooth and almost never symmetric, due to the closeness to the other cusps or folds (Figure 2.6(d)).

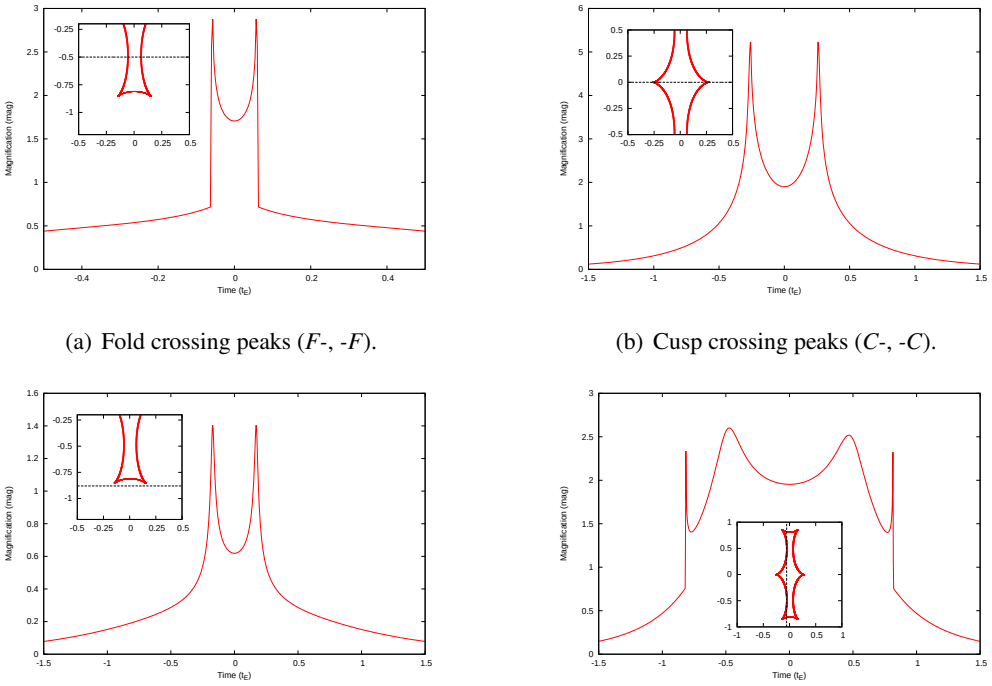

(a) Fold crossing peaks (*F*-, -*F*).

(b) Cusp crossing peaks (*C*-, -*C*).

(c) Cusp grazing peaks ($\bar{\text{C}}$).

(d) In-caustic fold grazing peaks ($\bar{\text{F}}$).

Figure 2.6: In order to show the four peak types, we chose the ($q = 0$, $s = 0.8$) intermediate topology and generate lightcurves for different source trajectories. In the four panels, lightcurves and corresponding source tracks are shown. Time in t_E is on the x-axis and magnification is on the y-axis.

By using building blocks for the lightcurves and the syntax we have defined above for the source tracks, we can unambiguously connect the lightcurves to the corresponding morphology class. The two source tracks used in the examples above (Figures 2.4 and 2.5), described by the sequences $A_1[a_{bp1}b_{tp2}]A_2$ and $[a_{b1}a_{t1}b_t]B_{t2}$, belong to the morphology classes $\bar{\text{C}}$ F-F $\bar{\text{C}}$ and F-$\bar{\text{F}}$-F $\bar{\text{C}}$, respectively.

2.4 The case of the equal-mass binary lens

We decided to simulate lightcurves for a source with an angular radius[1] $\rho_* = 0.002\,\theta_E$ undergoing microlensing by a static equal-mass binary lens. Lightcurves are then characterised only by:

1. the inclination angle α_0 between the source track and the axis connecting the two masses, considered positive anticlockwise and zero in case the source moves parallel to the axis from left to right;

2. the projected impact parameter u_0, in θ_E units, between the source track and the centre of mass of the lens, considered positive if the source and the centre of mass pass each other on the right-hand side.

We need to densely probe the parameter space defined by α_0 and u_0 by varying α_0 from 0 to 2π and by using u_0 large enough in both directions in order to be sure of probing the caustic curves of each topology. In our case, by ranging u_0 from –2 to +2 we are sure we are not missing any caustic grazing or crossing.

We produce magnification maps for each case we want to investigate by using the inverse ray shooting code called *luckylensing* (Marnach, 2010). We are going to probe the equal-mass binary lens with different separations s: 0.50, 0.65, 0.70, 0.85, 1.0, 1.5, 2.05, 2.50, with a resolution of 10^{-6}/*pixel*. Figures 2.7(a) to 2.7(h) show the magnification maps.

[1] we will treat the implications due to the source size at the end of the chapter

(a) $q = 1, s = 0.50$

(b) $q = 1, s = 0.60$

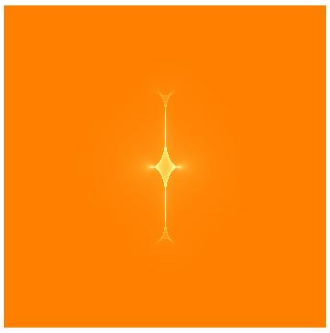

(c) $q = 1, s = 0.70$

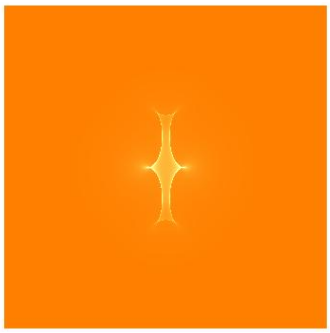

(d) $q = 1, s = 0.85$

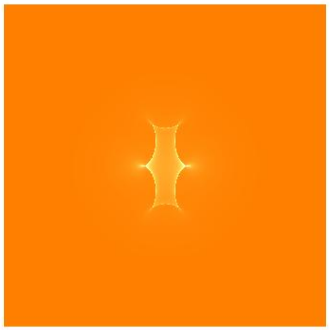

(e) $q = 1, s = 1.0$

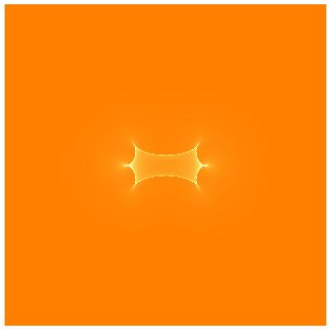

(f) $q = 1, s = 1.50$

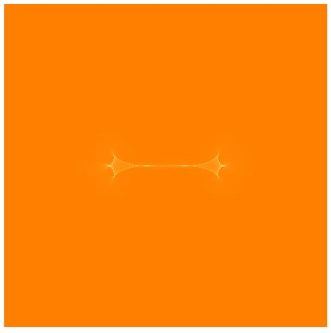

(g) $q = 1, s = 2.05$

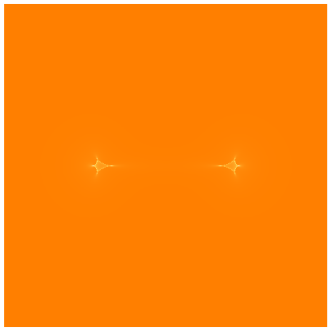

(h) $q = 1, s = 2.50$

Figure 2.7: The magnification maps produced for the classification.

Since we are just considering the static lens case and we have fixed the source size, we sample every magnification map by simulating lightcurves in order to probe the parameter space of α_0 and u_0 from 0 to $\pi/2$ and from 0 to 1, respectively, and take advantage of the symmetry of the maps. We produced one lightcurve for each point in the parameter space by sampling the two axis with 1600 steps. Using *luckylensing* routines we are able to count the peaks in the lightcurves and produce 3-dimensional datasets containing for every pair of α_0 and u_0 the relative number of peaks. By plotting these datasets for each separation, we obtain what we call *iso-peak region plots* showing, with a colour scale, the regions in the parameter space with a different number of peaks. Iso-peak region plots are then produced for each separation value (Figures 2.8(a) to 2.8(h), Liebig (2014)).

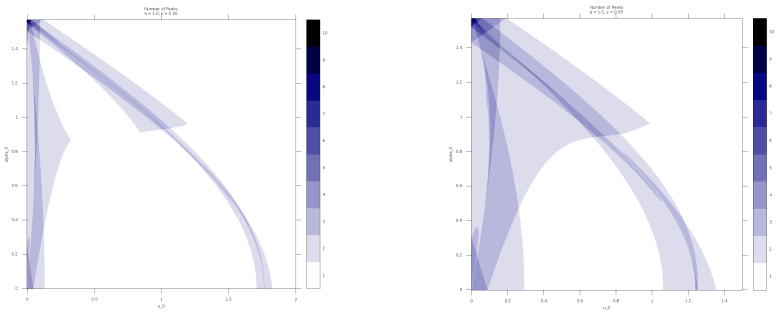

(a) $q = 1, s = 0.50$ (b) $q = 1, s = 0.60$

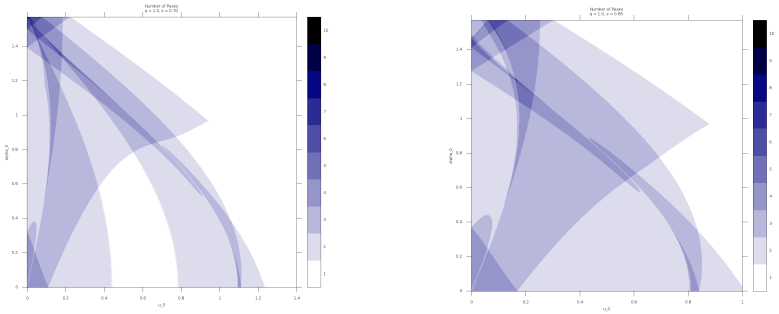

(c) $q = 1, s = 0.70$ (d) $q = 1, s = 0.85$

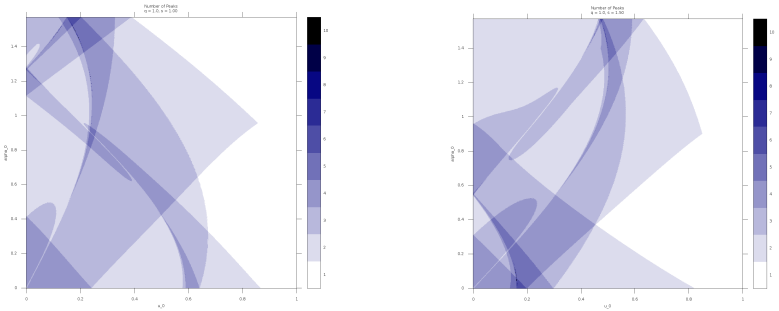

(e) $q = 1, s = 1.0$ (f) $q = 1, s = 1.50$

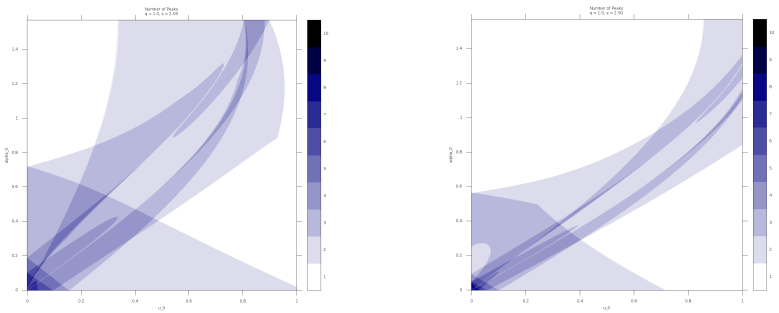

(g) $q = 1, s = 2.05$ (h) $q = 1, s = 2.50$

Figure 2.8: The iso-peak region plots inspected. Plots are in u_0 (x-axis) and α_0 (y-axis).

2.4.1 Iso-peak regions labelling

This kind of plots is the heart of the entire classification. By identifying regions in the parameter space for which we have the same number of peaks, we see how they merge, giving rise to new regions and destroying others. The behaviour of such a merging is continuous even close to the transition separation values $\sqrt{2}/2$ and 2, as one can notice by observing the plots in order of s.

Each region corresponds to a different possible lightcurve, and the geometrical extension of the region corresponds to the probability to observe that specific lightcurve. In most of the cases the regions are separated, but we can observe cases in which two of them are connected by narrow sub-regions representing values of α_0 and u_0 for which the lightcurve shows peaks due to a cusp crossing. The presence of such sub-regions occurs only if we consider a finite-size source, as we are doing. In case one tries to use a point-like source, the result is that such connecting areas between two regions disappear, shrinking to a point. We decided to use a finite source in order to simulate more realistic cases.

Regions with the same colour are those with the same number of peaks. Then, starting from the white, indicating one-peak regions, we can classify regions with the same peak number, one by one, and then move towards the darkest colour, indicating ten-peak regions. We use roman numbers, from I to X, in order to indicate the number of peaks. Lowercase letters are used to label the regions with the same peak number but with different peak sequence or nature. The labelling has been done by inspecting any single region moving away from the starting point $\alpha_0 = 0$, $u_0 = 0$.

2.4.1.1 The zero-plot: $q = 1.0, s = 1.0$

The "zero-plot" we start from is the $s = 1.0$ iso-peak region plot. Figure 2.9 shows the resulting labelled plot, while Table 2.1 shows the connection between caustic feature sequences and morphology classes. Once individuated, the iso-peak regions indicating the same peak sequences or symmetric peak sequences are classified in the same morphology class, as one can see in Table 2.2. We then repeat the process for all the separations in order to achieve the complete classification and summarise results in Section 2.5.

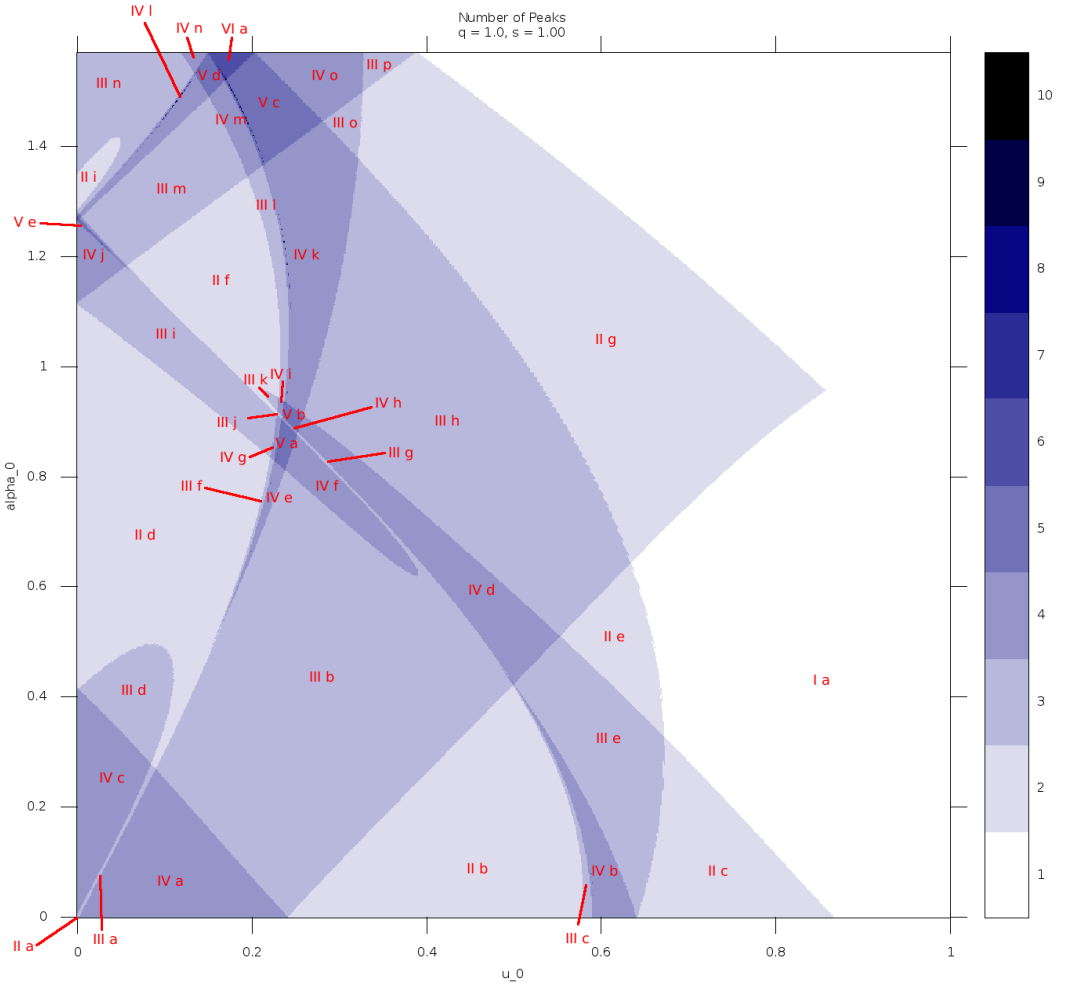

Figure 2.9: Iso-peak region plot for $s = 1.0$.

Table 2.1: Overview of the caustic feature sequences for $s = 1$.

Iso-maxima region	Caustic feature sequence	Morphology class
I a	Paczyński peak (or single cusp grazings)	$\bar{C}$
II a	$[A_1 A_2]$	C-C
II b	$[a_{t1} a_{t2}]$	F-F
II c	$B_{t1} B_{t2}$	C-C
II d	$[a_{b1} a_{t2}]$	F-F
II e	$[a_{t1} b_t]$	F-F
II f	$[a_{b1} b_t]$	F-F
II g	$A_1 B_{t1}$	C-C
II h	$[b_b b_t]$	F-F
II i	$[b_b b_t]$	F-F
III a	$[A_1 a_{t2}] A_2$	C-F $\bar{C}$
III b	$A_1 [a_{t1} a_{t2}]$	$\bar{C}$ F-F
III c	$[a_{t1} b_t a_{t2}]$	F-$\bar{F}$-F
III d	$A_1 [a_{b1} a_{t2}]$	$\bar{C}$ F-F
III e	$[a_{t1} b_t] B_{t2}$	F-F $\bar{C}$
III f	$[a_{b1} a_{t1} a_{t2}]$	F-$\bar{F}$-F
III g	$A_1 [a_{t1} B_{t2}]$	$\bar{C}$ F-C
III h	$A_1 [a_{t1} b_t]$	$\bar{C}$ F-F
III i	$[a_{b1} a_{t2}] B_{t2}$	F-F $\bar{C}$
III j	$[a_{b1} a_{t1} B_{t2}]$	F-$\bar{F}$-C
III k	$[a_{b1} b_t] B_{t2}$	F-F $\bar{C}$
III l	$[a_{b1} a_{t1} b_t]$	F-$\bar{F}$-F
III m	$B_{b1} [a_{b1} b_t]$	$\bar{C}$ F-F
III n	$[b_b a_{b1} b_t]$	F-$\bar{F}$-F
III o	$[a_{b1} a_{t1}] B_{t1}$	F-F $\bar{C}$
III p	$B_{b1} A_1 B_1$	$\bar{C}$ $\bar{C}$ $\bar{C}$
IV a	$A_1 [a_{t1} a_{t2}] A_2$	$\bar{C}$ F-F $\bar{C}$
IV b	$[a_{t1} b_t][b_t a_{t2}]$	F-F F-F
IV c	$A_1 [a_{b1} a_{t2}] A_2$	$\bar{C}$ F-F $\bar{C}$
IV d	$A_1 [a_{t1} b_t] B_{t2}$	$\bar{C}$ F-F $\bar{C}$
IV e	$[a_{b1} a_{t1}][a_{t1} a_{t2}]$	F-F F-F
IV f	$A_1 [a_{t1} a_{t2}] B_{t2}$	$\bar{C}$ F-F $\bar{C}$
IV g	$[a_{b1} a_{t1} a_{t2}] B_{t2}$	F-$\bar{F}$-F $\bar{C}$
IV h	$[a_{b1} a_{t1}][a_{t1} B_{t2}]$	F-F F-C
IV i	$[a_{b1} a_{t1} b_t] B_{t2}$	F-$\bar{F}$-F $\bar{C}$

Continued on next page.

Table 2.1: Continued.

Iso-maxima region	Caustic feature sequence	Morphology class
IV j	$B_{b1}[a_{b1}a_{t2}]B_{t2}$	$\bar{C}$ F-F $\bar{C}$
IV k	$[a_{b1}a_{t1}][a_{t1}b_t]$	F-F F-F
IV l	$[b_b a_{b1}][a_{b1}b_t]$	F-F F-F
IV m	$B_{b1}[a_{b1}a_{t1}b_t]$	$\bar{C}$ F-$\bar{F}$-F
IV n	$[b_b a_{b1}a_{t1}b_t]$	F-$\bar{F}$-$\bar{F}$-F
IV o	$B_{b1}[a_{b1}a_{t1}]B_{t1}$	$\bar{C}$ F-$\bar{F}$-F
V a	$[a_{b1}a_{t1}][a_{t1}a_{t2}]B_{t2}$	F-F F-F $\bar{C}$
V b	$[a_{b1}a_{t1}][a_{t1}b_t]B_{t2}$	F-F F-F $\bar{C}$
V c	$B_{b1}[a_{b1}a_{t1}][a_{t1}b_t]$	$\bar{C}$ F-F F-F
V d	$[b_b a_{b1}][a_{b1}a_{t1}b_t]$	F-F F-$\bar{F}$-F
V e	$B_{b1}[a_{b1}a_{t2}][a_{t2}b_t]$	$\bar{C}$ F-F F-F
VI a	$[b_b a_{b1}][a_{b1}a_{t1}][a_{t1}b_t]$	F-F F-F F-F

Table 2.2: The census of the morphology classes in the case of $s = 1$.

Morphology class	Iso-maxima regions
$\bar{C}$	I
F-F	II b, d, e, f, h, i
$\bar{C}$ $\bar{C}$	II c, g
C-C	II a
$\bar{C}$ F-F	III b, d, e, h, i, k, m, o
F-$\bar{F}$-F	III c, f, l, n
C-F $\bar{C}$	III a, g
F-$\bar{F}$-C	III j
$\bar{C}$ $\bar{C}$ $\bar{C}$	III p
$\bar{C}$ F-F $\bar{C}$	IV a, c, d, f, g, j
F-F F-F	IV b, e, k, l
F-$\bar{F}$-F $\bar{C}$	IV i, g, m, o
F-F F-C	IV h
F-$\bar{F}$-$\bar{F}$-F	IV n
F-F F-F $\bar{C}$	V a, b, c, e
F-F F-$\bar{F}$-F	V d
F-F F-F F-F	VI a

2.5 Results and lightcurve zoo

The work aims at investigating all the possible lightcurves arising from the equal-mass binary microlensing of a source with angular radius $0.002\,\theta_E$. The final goal is to achieve the complete classification of the morphologies of the lightcurves and in order to do that we have examined eight lens separations. We have also proposed a syntax and a classification scheme which can theoretically be used for, or at least extended to, any mass ratios.

We have then classified **73** different lightcurves morphologies arising in **232** independent iso-peak regions. The results are summarised in Table 2.4, where we collect all the possible lightcurve peak sequences in ten different rows corresponding to the number of the peaks, and in **73** different sub-rows corresponding to the morphology classes. The results for the three topologies are collected in three different columns.

The **73** lightcurve morphologies are shown with a sample of each kind in Figures from 2.11 to 2.18.

2.5.1 Source size implications

The choice of a finite size source is aimed at studying the most realistic lightcurves, implying also the simulation of cusp crossings. If one considered a point-like source, the only possible trajectory which could intersect the caustic via the infinitesimal cusp point would be individuated by just a point in the parameter space, then would have zero occurrence probability.
The size of the source, anyway, influences the shape of the lightcurve, modifying the peak-counting sensitivity. By using a source with radius $\rho_* = 0.002\ \theta_E$, we are indeed not sensitive to peaks arising from two subsequent caustic crossings within a distance smaller than $2 \times \rho_* = 2 \times 10^{-3}\theta_E$ (Figure 2.10). By shrinking the source size we would resize the iso-peak regions, but we would not add new information to the classification.

2.5.2 Error margin

We chose to neglect very small sub-regions in the parameter space by considering only iso-peak regions larger than 10×10 pixels. This means that, since we have sampled u_0 and α_0 axes with 1/1600, the area of a neglected region is $10^2 \times 1/1600 \times \frac{\pi}{2}/1600$, thus the probability to observe that specific lightcurve is $\lesssim 1/16000$.

2.5.3 Non-equal mass lenses

When considering $q \neq 1$, new morphology classes can occur, as this work is limited to the equal-mass static binary microlensing. Although our classification does not include non-equal

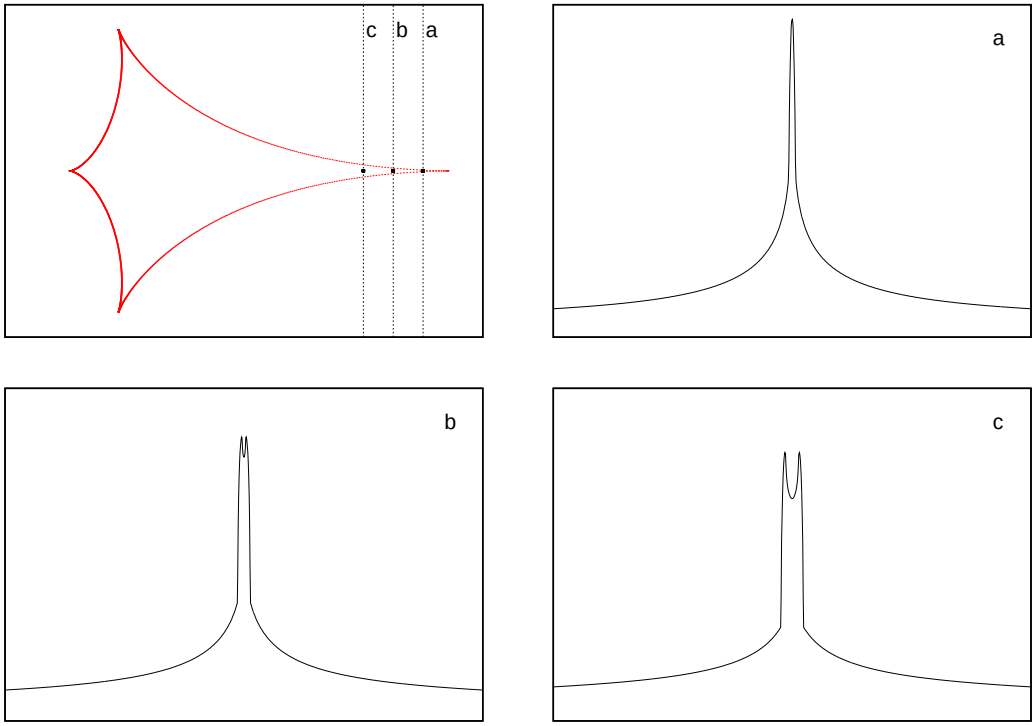

Figure 2.10: Three cases showing how the caustic crossing appears as a caustic grazing (*a*) due to the source size. When the separation between two folds becomes larger than the source diameter (*b* and *c*), the lightcurve shows the caustic crossing peaks.

mass cases, the scheme we have presented could be useful if one extended the classification, by still using the same building blocks we have just defined.

2.5.4 Occurrence rate

By looking at the extension of the iso-peak regions, we can infer the theoretical occurrence rate of the iso-peak lightcurves in the separation regimes we have studied, among the three topologies. Table 2.3 summarises the percentage of lightcurves, out of a total of 1.28×10^7 simulations for impact parameters $u_0 < 2$ (i.e. in the scenarios we have investigated), according to the number of the peaks in the 3-dimensional parameter space defined by u_0, α_0, and s that we have investigated. The table shows, among the separation values we have studied, that the probability of observing lightcurves with more than four peaks is less than 2% in each case. Lightcurves with two to four peaks are the commonest ones. The morphology classes individuated by the largest areas in the iso-peak region plots are F-F, $\bar{\text{C}}$ $\bar{\text{C}}$, $\bar{\text{C}}$ F-F, $\bar{\text{C}}$ F-F $\bar{\text{C}}$, and F-F F-F, compatibly with the lightcurves we observe in nature.

Table 2.3: Occurrence rate (%) of iso-peak lightcurves over 1.28×10^7 simulations. The occurrence rate reflects the probability to observe a specific iso-peak lightcurve in nature.

	$s = 0.5$	$s = 0.65$	$s = 0.7$	$s = 0.85$	$s = 1.0$	$s = 1.5$	$s = 2.05$	$s = 2.5$
I	78.81	60.66	48.98	25.74	31.26	30.97	61.03	33.27
II	11.12	19.18	31.19	36.79	29.39	37.26	24.05	40.87
III	4.31	7.89	14.93	28.2	28.67	18.07	11.27	17.34
IV	0.64	1.94	3.99	7.75	9.65	11.84	3.18	6.98
V	0.06	0.27	0.65	1.33	0.94	1.77	0.30	1.12
VI	0.04	0.08	0.23	0.19	0.09	0.09	0.11	0.26
VII	0.01	0.03	0.03	-	-	-	0.04	0.15
VIII	0.008	0.02	0.004	-	-	-	0.03	0.004
IX	0.005	0.005	0.001	-	-	-	-	-
X	0.003	0.0002	0.0009	-	-	-	-	-

Table 2.4: Overview of morphology classes for Close, Intermediate and Wide topologies.

	Morphology Class	Close	Intermediate	Wide
I	$\bar{C}$	outside caustics between caustics	outside caustics	outside caustics between caustics
II	F-F	$[a_{tp1}a_{tp2}]$, $[a_{ts1}a_{ts2}]$, $[a_{bp1}a_{tp2}]$, $[a_{ts1}b_t]$, $[a_{bp1}a_{tp1}]$	$[a_{t1}a_{t2}]$, $[a_{b1}a_{t2}]$, $[a_{t1}b_t]$, $[a_{b1}b_t]$, $[b_bb_t]$	$[a_{b1}b_{t1}]$, $[b_{b1}b_{t1}]$
	$\bar{C}$ $\bar{C}$	$B_{t1}B_{t2}$, A_1B_{t1}, A_1C_{tp}, A_1C_{ts}, A_1B_{t2}, $C_{ts}B_{t2}$	$B_{t1}B_{t2}$, A_1B_{t1}	$B_{t1}B_{t2}$, A_1B_{t1}, $B_{b1}D_1$, $B_{b1}B_{t2}$
	C-C	$[A_1A_2]$	$[A_1A_2]$	-
	C-F	$[a_{ts1}B_{t2}]$, $[A_1a_{tp2}]$	$[a_{t1}B_{t2}]$, $[A_1a_{t2}]$, $[B_{b1}b_t]$, $[A_1a_{t2}]$	$[B_{b1}b_{t1}]$
III	$\bar{C}$ F-F	$A_1[a_{tp1}a_{tp2}]$, $A_1[a_{bp1}a_{tp2}]$, $[a_{ts1}b_t]B_{t2}$, $A_1[a_{ts1}b_t]$, $[a_{bp1}a_{tp2}]B_{t2}$, $[a_{bp1}a_{tp1}]B_{t1}$, $[a_{ts1}a_{ts2}]B_{t2}$, $[a_{ts1}a_{tp2}]B_{t2}$, $[a_{bp1}a_{tp2}]C_{tp}$, $[a_{bp1}a_{tp1}]C_{tp}$, $[a_{bp1}a_{tp1}]B_{t2}$	$A_1[a_{t1}a_{t2}]$, $A_1[a_{b1}a_{t2}]$, $[a_{t1}b_t]B_{t2}$, $A_1[a_{t1}b_t]$, $[a_{b1}a_{t2}]B_{t2}$, $[a_{b1}b_t]B_{t2}$, $B_{b1}[a_{b1}b_t]$, $[a_{b1}a_{t1}]B_{t1}$, $[a_{t1}a_{t2}]B_{t2}$, $[a_{b1}b_t]B_{t2}$, $B_{b1}[b_bb_t]$	$[a_{t1}b_{t1}]B_{t2}$, $A_1[a_{t1}b_{t1}]$, $B_{b1}[a_{b1}b_{t1}]$, $[a_{b1}a_{t1}]B_{t1}$, $[a_{b1}b_{t1}]B_{t2}$, $B_{b1}[b_{b1}b_{t1}]$, $A_1[b_{b1}b_{t1}]$, $[a_{b1}b_{b1}]B_{t2}$
	F-$\bar{F}$-F	$[a_{ts1}b_ta_{ts2}]$, $[a_{bp1}a_{tp1}a_{tp2}]$	$[a_{t1}b_ta_{t2}]$, $[a_{b1}a_{t1}a_{t2}]$, $[a_{b1}a_{t1}b_t]$, $[b_ba_{b1}b_t]$, $[a_{b1}a_{t2}b_t]$, $[a_{b1}b_ta_{t2}]$	$[a_{b1}a_{t1}b_{t1}]$, $[a_{b1}b_{b1}b_{t1}]$
	$\bar{C}$ F-C	$[A_1a_{tp2}]A_2$, $C_{bp}[abp1C_{tp}]$	$[A_1a_{t2}]A_2$, $A_1[a_{t1}B_{t2}]$, $[A_1b_t]B_{t2}$	$[A_1b_{t1}]B_{t2}$
	$\bar{C}$ $\bar{C}$ $\bar{C}$	$B_{b1}A_1B_{t1}$, $A_1C_{ts}B_{t2}$	$B_{b1}A_1B_{t1}$	$B_{b1}A_1B_{t1}$, $B_{b1}D_1B_{t2}$, $A_1B_{t1}B_{t2}$, $B_{b1}A_1B_{t2}$
	C-$\bar{F}$-F	-	$[A_1b_ta_{t2}]$	-
	$\bar{C}$ C-F	$A_1[C_{ts}b_t]$	-	-
	$\bar{C}$ F-F $\bar{C}$	$A_1[a_{tp1}a_{tp2}]A_2$, $A_1[a_{bp1}a_{tp2}]A_2$, $A_1[a_{ts1}a_{ts2}]B_{t2}$, $B_{b1}[a_{bp1}a_{tp2}]B_{t2}$, $B_{b1}[a_{bp1}b_{tp1}]B_{t1}$, $C_{bp}[a_{bp1}a_{tp2}]C_{tp}$	$A_1[a_{t1}a_{t2}]A_2$, $A_1[a_{b1}a_{t2}]A_2$, $A_1[a_{t1}b_t]B_{t2}$, $A_1[a_{t1}a_{t2}]B_{t2}$, $B_{b1}[a_{b1}a_{t2}]B_{t2}$, $B_{b1}[a_{b1}a_{t1}]B_{t1}$, $A_1[a_{b1}b_t]B_{t2}$, $B_{b1}[a_{b1}b_t]B_{t2}$	$A_1[a_{t1}b_{t1}]B_{t2}$, $B_{b1}[b_{b1}b_{t1}]B_{t2}$, $B_{b1}[a_{b1}a_{t1}]B_{t1}$, $A_1[a_{b1}b_{t1}]B_{t2}$

Continued on next page.

Table 2.4: Morphology classes (continued).

	Morphology Class	Close	Intermediate	Wide
IV	F-F F-F	$[a_{ts1}b_t][b_t a_{ts2}]$, $[a_{bp1}a_{tp1}][a_{tp1}a_{tp2}]$, $[a_{bp1}a_{tp1}][a_{ts1}b_t]$	$[a_{t1}b_t][b_t a_{t2}]$, $[a_{b1}a_{t1}][a_{t1}a_{t2}]$, $[a_{b1}a_{t1}][a_{t1}b_t]$, $[b_b a_{b1}][a_{b1}b_t]$, $[a_{b1}a_{t2}][a_{t2}b_t]$, $[a_{b1}b_t][b_t a_{t2}]$	$[a_{t1}b_{t1}][b_{t2}a_{t2}]$, $[a_{b1}a_{t1}][a_{t1}b_{t1}]$, $[a_{b1}b_{b1}][b_{b1}b_{t1}]$, $[a_{b1}b_{b1}][b_{t2}a_{t2}]$
	$\bar{C}$ F-$\bar{F}$-F	$[a_{bp1}a_{tp1}a_{tp2}]B_{t2}$, $A_1[a_{ts1}a_{ts2}b_t]$	$[a_{b1}a_{t1}a_{t2}]B_{t2}$, $[a_{b1}a_{t1}b_t]B_{t2}$, $B_{b1}[a_{b1}a_{t1}b_t]$, $A_1[a_{t1}b_t a_{t2}]$, $A_1[a_{b1}b_t a_{t2}]$, $B_{b1}[a_{b1}a_{t2}b_t]$	$B_{b1}[a_{b1}a_{t1}b_{t1}]$, $[a_{b1}b_{b1}b_{t1}]B_{t2}$
	F-$\bar{F}$-$\bar{F}$-F	-	$[b_b a_{b1}a_{t1}b_t]$, $[a_{b1}a_{t1}a_{t2}b_t]$, $[b_b a_{b1}a_{t2}b_t]$	-
	C-F F-F	-	$[a_{b1}a_{t1}][a_{t1}B_{t2}]$, $[A_1b_t][b_t a_{t2}]$	$[A_1b_{t1}][b_{t2}a_{t2}]$
	F-F $\bar{C}$ $\bar{C}$	$[a_{bp1}a_{tp1}]C_{tp}B_{t2}$, $[a_{bp1}a_{tp1}]C_{ts}B_{t2}$, $A_1C_{ts}[a_{ts1}b_t]$, $A_1C_{ts}[a_{ts2}b_t]$, $[a_{bp1}a_{tp1}]C_{ts}B_{t1}$	-	$[a_{b1}b_{b1}]D_1B_{t2}$
	C-C C-C	-	-	$[A_1D_1][D_2A_2]$
	F-F C-F	$[a_{bp1}a_{tp1}][C_{ts}b_t]$	-	-
	C-F $\bar{C}$ $\bar{C}$	-	-	$[A_1b_{t1}]D_1B_{t2}$
	$\bar{C}$ F-C $\bar{C}$	$C_{bp}[a_{bp1}C_{tp}]B_{t2}$	-	-
V	$\bar{C}$ F-F F-F	$[a_{bp1}a_{tp1}][a_{tp1}a_{tp2}]B_{t1}$, $B_{b1}[a_{bp1}a_{tp1}][a_{ts1}b_t]$, $B_{b1}[a_{bp1}a_{tp1}][a_{ts2}b_t]$, $A_1[a_{ts1}a_{ts2}][a_{ts2}b_t]$	$[a_{b1}a_{t1}][a_{t1}a_{t2}]B_{t2}$, $B_{b1}[a_{b1}a_{t1}][a_{t1}b_t]$, $B_{b1}[a_{b1}a_{t2}][a_{t2}b_t]$, $A_1[a_{t1}b_t][b_t a_{t2}]$, $B_{b1}[a_{b1}a_{t2}][a_{t2}b_t]$, $A_1[a_{b1}b_t][b_t a_{t2}]$	$B_{b1}[a_{b1}a_{t1}][a_{t1}b_{t1}]$, $A_1[a_{t1}b_{t1}][b_{t2}a_{t2}]$, $A_1[a_{b1}b_{t1}][b_{t2}a_{t2}]$, $[a_{b1}b_{b1}][b_{b1}b_{t1}]B_{t2}$, $[a_{b1}b_{b1}][b_{b1}b_{t1}]D_1$, $A_1[a_{b1}b_{b1}][b_{t1}a_{t2}]$
	F-F F-$\bar{F}$-F	$[a_{bp1}a_{tp1}][a_{ts1}a_{ts2}b_t]$	$[b_b a_{b1}][a_{b1}a_{t1}b_t]$, $[a_{b1}a_{t1}][a_{t1}a_{t2}b_t]$, $[a_{b1}a_{t1}a_{t2}][a_{t2}b_t]$, $[b_b a_{b1}][a_{b1}a_{t2}b_t]$, $[a_{b1}b_b b_t][b_t a_{t2}]$	-
	$\bar{C}$ F-$\bar{F}$-F $\bar{C}$	$B_{b1}[a_{bp1}a_{tp1}a_{tp2}]B_{t2}$	$A_1[a_{t1}b_t a_{t2}]A_2$	$A_1[a_{b1}b_{b1}b_{t1}]B_{t2}$
	$\bar{C}$ F-F $\bar{C}$ $\bar{C}$	$B_{b1}[a_{bp1}a_{tp1}]C_{tp}B_{t2}$, $C_{bp}[a_{bp1}a_{tp2}]C_{tp}B_{t2}$, $C_{bp}[a_{bp1}a_{tp1}]C_{tp}B_{t2}$, $B_{b1}[a_{bp1}a_{tp1}]C_{ts}B_{t1}$	-	$A_1[a_{b1}b_{b1}]D_1B_{t2}$, $A_1[a_{t1}b_{t1}]D_1B_{t2}$, $A_1[a_{b1}b_{t1}]D_1B_{t2}$
	F-F $\bar{C}$ F-F	$[a_{bp1}a_{tp1}]C_{ts}[a_{ts2}b_t]$, $[a_{bp1}a_{tp1}]C_{ts}[a_{ts1}b_t]$	-	$[a_{b1}b_{b1}]D_2[b_{t2}a_{t2}]$

Continued on next page.

Table 2.4: Morphology classes (continued).

	Morphology Class	Close	Intermediate	Wide
	$\bar{C}$ F-F C-F	$B_{b1}[a_{bp1}a_{tp1}][C_{ts}b_t]$	-	-
	C-C C-F $\bar{C}$	-	-	$[A_1D_1][D_2a_{t2}]A_2$
	C-F F-F $\bar{C}$	-	-	$[A_1b_{t1}][b_{t2}a_{t2}]A_2$
	$\bar{C}$ F-C F-F	-	-	$A_1[a_{b1}D_1][b_{t2}a_{t2}]$
	C-F $\bar{C}$ F-F	-	-	$[A_1b_{t1}]D_1[b_{t2}a_{t2}]$
	F-F $\bar{C}$ $\bar{C}$ $\bar{C}$	$[a_{bp1}a_{tp1}]C_{tp}C_{ts}B_{t2}$	-	-
	$\bar{C}$ $\bar{C}$ F-C $\bar{C}$	$B_{b1}Cbp[a_{bp1}C_{tp}]B_{t2}$	-	-
	F-F F-F F-F	$[b_ba_{bs1}][a_{bp1}a_{tp1}][a_{ts1}b_t]$, $[a_{bp1}a_{tp1}][a_{ts1}a_{ts2}][a_{ts2}b_t]$, $[b_ba_{bs1}][a_{bp1}a_{tp1}][a_{ts2}b_t]$	$[b_ba_{b1}][a_{b1}a_{t1}][a_{t1}b_t]$, $[a_{b1}a_{t1}][a_{t1}a_{t2}][a_{t2}b_t]$, $[b_ba_{b1}][a_{b1}a_{t2}][a_{t2}b_t]$	-
	$\bar{C}$ F-F F-F $\bar{C}$	$B_{b1}[a_{bp1}a_{tp1}][a_{tp1}a_{tp2}]B_{t2}$	$A_1[a_{t1}b_t][b_ta_{t2}]A_2$	$A_1[a_{t1}b_{t1}][b_{t2}a_{t2}]A_2$, $A_1[a_{b1}b_{t1}][b_{t2}a_{t2}]A_2$, $A_1[a_{b1}b_{b1}][b_{b1}b_{t1}]B_{t2}$, $A_1[a_{b1}b_{b1}][b_{t2}a_{t2}]A_2$
	$\bar{C}$ F-F $\bar{C}$ F-F	$B_{b1}[a_{bp1}a_{tp1}]C_{tp}[a_{ts2}b_t]$, $B_{b1}[a_{bp1}a_{tp1}]C_{ts}[a_{ts2}b_t]$, $B_{b1}[a_{bp1}a_{tp2}]C_{tp}[a_{ts2}b_t]$	-	$A_1[a_{b1}b_{b1}]D_1[b_{t2}a_{t2}]$, $A_1[a_{b1}b_{t1}]D_1[b_{t2}a_{t2}]$, $A_1[a_{t1}b_{t1}]D_1[b_{t2}a_{t2}]$
	$\bar{C}$ F-$\bar{F}$-F F-F	$B_{b1}[a_{bp1}a_{tp1}a_{tp2}][a_{ts2}b_t]$	-	$A_1[a_{b1}b_{b1}b_{t1}][b_{t2}a_{t2}]$
VI	C-F $\bar{C}$ F-F $\bar{C}$	-	-	$[A_1b_{t1}]D_1[b_{t2}a_{t2}]A_2$
	F-C C-C C-F	$[b_bC_{bs}][C_{bp}C_{tp}][C_{ts}b_t]$	-	-
	$\bar{C}$ F-F $\bar{C}$ C-F	$B_{b1}[a_{bp1}a_{tp1}]C_{tp}[C_{ts}b_t]$	-	-
	F-F F-F C-F	$[b_ba_{bs1}][a_{bp1}a_{tp1}][C_{ts}b_t]$	-	-
	C-C $\bar{C}$ F-F $\bar{C}$	-	-	$[A_1D_1]D_2[b_{t2}a_{t2}]A_2$
	$\bar{C}$ F-C F-F $\bar{C}$	-	-	$A_1[a_{b1}D_1][b_{t2}a_{t2}]A_2$

Continued on next page.

Table 2.4: Morphology classes (continued).

	Morphology Class	Close	Intermediate	Wide
	$\bar{C}\ \bar{C}$ F-F $\bar{C}\ \bar{C}$	$B_{b1}C_{bp}[a_{bp1}a_{tp2}]C_{tp}B_{t2}$, $B_{b1}C_{bp}[a_{bp1}a_{tp1}]C_{tp}B_{t2}$, $B_{b1}C_{bp}[a_{bp1}a_{tp1}]C_{tp}B_{t1}$	-	-
	$\bar{C}\ \bar{C}$ F-C $\bar{C}\ \bar{C}$	$B_{b1}C_{bp}[a_{bp1}C_{tp}]C_{ts}B_{t2}$	-	-
	$\bar{C}$ F-F $\bar{C}\ \bar{C}\ \bar{C}$	$B_{b1}[a_{bp1}a_{tp1}]C_{tp}C_{ts}B_{t2}$	-	-
	F-F F-C F-F	$[b_b a_{bs1}][a_{bp1}C_{tp}][a_{ts}b_t]$	-	-
	F-F F-F $\bar{C}$ F-F	$[b_b a_{bs1}][a_{bp1}a_{tp1}]C_{tp}[a_{ts2}b_t]$, $[b_b a_{bs1}][a_{bp1}a_{tp1}]C_{tp}[a_{ts1}b_t]$, $[b_b a_{bs1}][a_{bp1}a_{tp2}]C_{tp}[a_{ts2}b_t]$	-	-
	$\bar{C}$ F-F $\bar{C}\ \bar{C}$ F-F	$B_{b1}[a_{bp1}a_{tp1}]C_{tp}C_{ts}[a_{ts2}b_t]$, $B_{b1}[a_{bp1}a_{tp1}]C_{tp}C_{ts}[a_{ts1}b_t]$	-	-
	F-F F-F $\bar{C}$ C-F	$[b_b a_{bs1}][a_{bp1}a_{tp1}]C_{tp}[C_{ts}b_t]$	-	-
VII	$\bar{C}\ \bar{C}\ \bar{C}$ F-C $\bar{C}\ \bar{C}$	$B_{b1}C_{bs}C_{bp}[a_{bp1}C_{tp}]C_{ts}B_{t2}$	-	-
	$\bar{C}\ \bar{C}$ F-F $\bar{C}\ \bar{C}\ \bar{C}$	$B_{b1}C_{bp}[a_{bp1}a_{tp1}]C_{tp}C_{ts}B_{t2}$	-	-
	F-F $\bar{C}$ C-C C-F	$[b_b a_{bs1}]C_{bs}[C_{bp}Ctp][C_{ts}b_t]$	-	-
	$\bar{C}\ \bar{C}$ F-F $\bar{C}$ C-F	$B_{b1}C_{bp}[a_{bp1}a_{tp1}]C_{tp}[C_{ts}b_t]$	-	-
	$\bar{C}$ F-C $\bar{C}$ F-F $\bar{C}$	-	-	$A_1[a_{b1}D_1]D_2[b_{t2}a_{t2}]A_2$
	C-F $\bar{C}\ \bar{C}$ F-F $\bar{C}$	-	-	$[A_1 b_{t1}]D_1 D_2[b_{t2}a_{t2}]A_2$
	$\bar{C}$ F-F $\bar{C}$ F-F $\bar{C}$	-	-	$A_1[a_{b1}b_{b1}]D_1[b_{t2}a_{t2}]A_2$, $A_1[a_{b1}b_{t1}]D_1[b_{t2}a_{t2}]A_2$, $A_1[a_{t1}b_{t1}]D_1[b_{t2}a_{t2}]A_2$
	$\bar{C}$ F-F F-F F-F	$B_{b1}[a_{bp1}a_{tp1}][a_{tp1}a_{tp2}][a_{ts2}b_t]$	-	$A_1[a_{b1}b_{b1}][b_{b1}b_{t1}][b_{t2}a_{t2}]$

Continued on next page.

Table 2.4: Morphology classes (continued).

	Morphology Class	Close	Intermediate	Wide
VIII	F-F $\bar{C}$ F-F $\bar{C}$ F-F	$[b_b a_{bs1}]C_{bp}[a_{bp1}a_{tp1}]C_{tp}[a_{ts1}b_t]$, $[b_b a_{bs1}]C_{bp}[a_{bp1}a_{tp2}]C_{tp}[a_{ts2}b_t]$, $[b_b a_{bs1}]C_{bp}[a_{bp1}a_{tp1}]C_{tp}[a_{ts2}b_t]$	-	-
	F-F $\bar{C}$ C-C $\bar{C}$ F-F	$[b_b a_{bs1}]C_{bs}[C_{bs}C_{tp}]C_{ts}[a_{ts2}b_t]$	-	-
	F-F $\bar{C}$ F-C $\bar{C}$ F-F	$[b_b a_{bs1}]C_{bp}[a_{bp1}C_{tp}]C_{ts}[a_{ts2}b_t]$, $[b_b a_{bs1}]C_{bp}[a_{bp1}C_{tp}]C_{ts}[a_{ts1}b_t]$	-	-
	F-F $\bar{C}$ $\bar{C}$ F-C C-F	$[b_b a_{bs1}]C_{bs}C_{bp}[a_{bp1}C_{tp}][C_{ts}b_t]$	-	-
	F-F $\bar{C}$ F-F $\bar{C}$ C-F	$[b_b a_{bs1}]C_{bp}[a_{bp1}a_{tp1}]C_{tp}[C_{ts}b_t]$	-	-
	F-F F-F $\bar{C}$ $\bar{C}$ F-F	$[b_b a_{bs1}][a_{bp1}a_{tp1}]C_{tp}C_{ts}[a_{ts2}b_t]$, $[b_b a_{bs1}][a_{bp1}a_{tp1}]C_{tp}C_{ts}[a_{ts1}b_t]$	-	-
	$\bar{C}$ $\bar{C}$ $\bar{C}$ F-F $\bar{C}$ $\bar{C}$ $\bar{C}$	$B_{b1}C_{bs}C_{bp}[a_{bp1}a_{tp2}]C_{tp}C_{ts}B_{t2}$, $B_{b1}C_{bs}C_{bp}[a_{bp1}a_{tp1}]C_{tp}C_{ts}B_{t1}$	-	-
	$\bar{C}$ $\bar{C}$ F-F $\bar{C}$ $\bar{C}$ F-F	$B_{b1}C_{bp}[a_{bp1}a_{tp1}]C_{tp}C_{ts}[a_{ts2}b_t]$, $B_{b1}C_{bp}[a_{bp1}a_{tp1}]C_{tp}C_{ts}[a_{ts1}b_t]$	-	-
	$\bar{C}$ $\bar{C}$ $\bar{C}$ F-F $\bar{C}$ C-F	$B_{b1}C_{bs}C_{bp}[a_{bp1}a_{tp1}]C_{tp}[C_{ts}b_t]$	-	-
	$\bar{C}$ F-F $\bar{C}$ $\bar{C}$ F-F $\bar{C}$			$A_1[a_{b1}b_{b1}]D_1D_2[b_{t2}a_{t2}]A_2$
IX	F-F $\bar{C}$ $\bar{C}$ F-C $\bar{C}$ F-F	$[b_b a_{bs1}]C_{bs}C_{bp}[a_{bp1}C_{tp}]C_{ts}[a_{ts2}b_t]$	-	-
	F-F $\bar{C}$ $\bar{C}$ F-F $\bar{C}$ C-F	$[b_b a_{bs1}]C_{bs}C_{bp}[a_{bp1}a_{tp1}]C_{tp}[C_{ts}b_t]$	-	-
	$\bar{C}$ $\bar{C}$ $\bar{C}$ F-F $\bar{C}$ $\bar{C}$ F-F	$B_{b1}C_{bs}C_{bp}[a_{bp1}a_{tp1}]C_{tp}C_{ts}[a_{ts2}b_t]$, $B_{b1}C_{bs}C_{bp}[a_{bp1}a_{tp1}]C_{tp}C_{ts}[a_{ts1}b_t]$	-	-
	F-F $\bar{C}$ F-F $\bar{C}$ $\bar{C}$ F-F	$[b_b a_{bs1}]C_{bp}[a_{bp1}a_{tp1}]C_{tp}C_{ts}[a_{ts2}b_t]$, $[b_b a_{bs1}]C_{bp}[a_{bp1}a_{tp1}]C_{tp}C_{ts}[a_{ts1}b_t]$	-	-

Continued on next page.

Table 2.4: Morphology classes (continued).

	Morphology Class	Close	Intermediate	Wide
X	F-F $\tilde{C}$ $\tilde{C}$ F-F $\tilde{C}$ $\tilde{C}$ F-F	$[b_b a_{bs1}]C_{bs}C_{bp}[a_{bp1}a_{tp1}]C_{tp}C_{ts}[a_{ts2}b_t]$, $[b_b a_{bs1}]C_{bs}C_{bp}[a_{bp1}a_{tp1}]C_{tp}C_{ts}[a_{ts1}b_t]$	-	-

Figure 2.11: The lightcurve zoo. (Liebig et al., 2015)

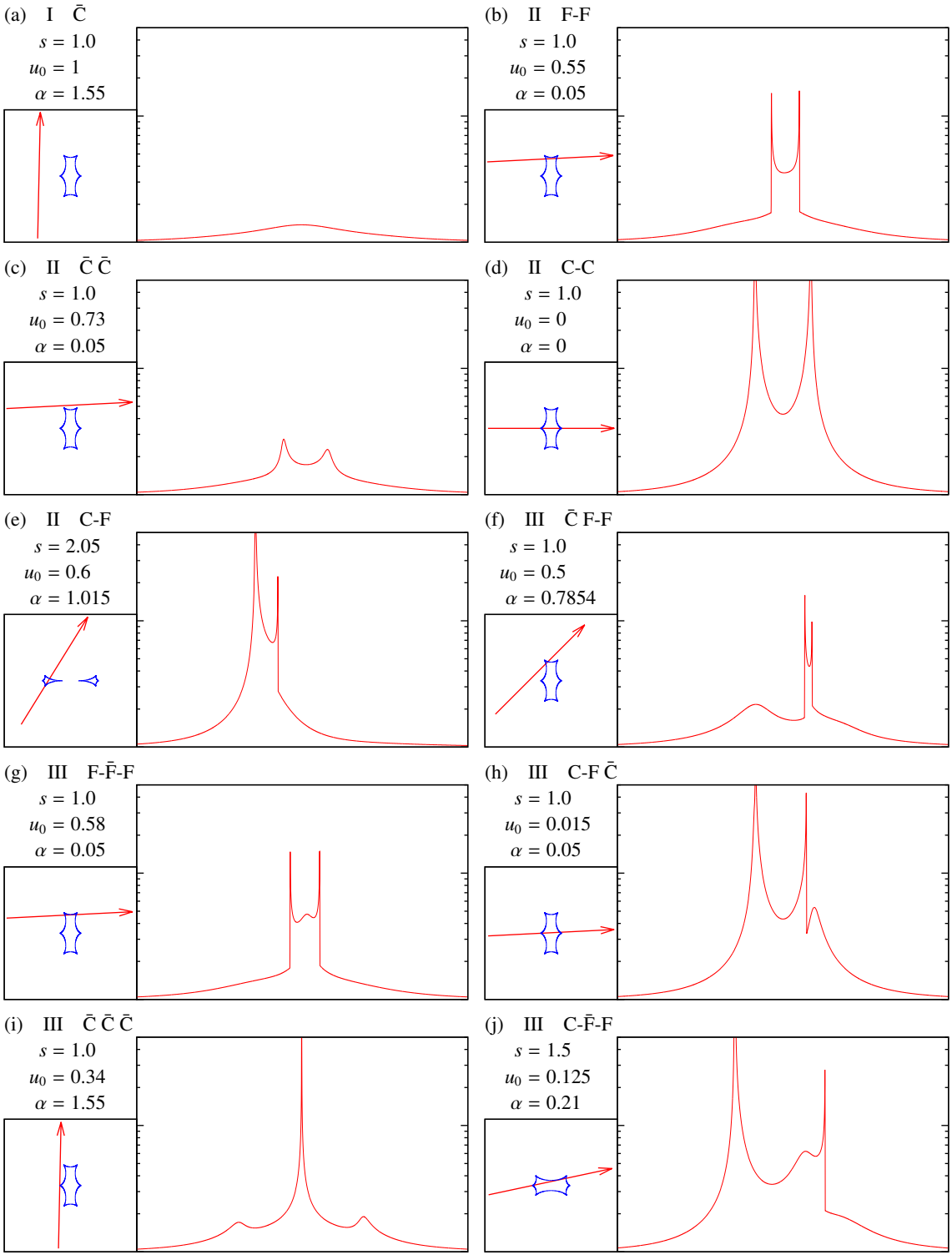

Figure 2.12: The lightcurve zoo. (Continued.)

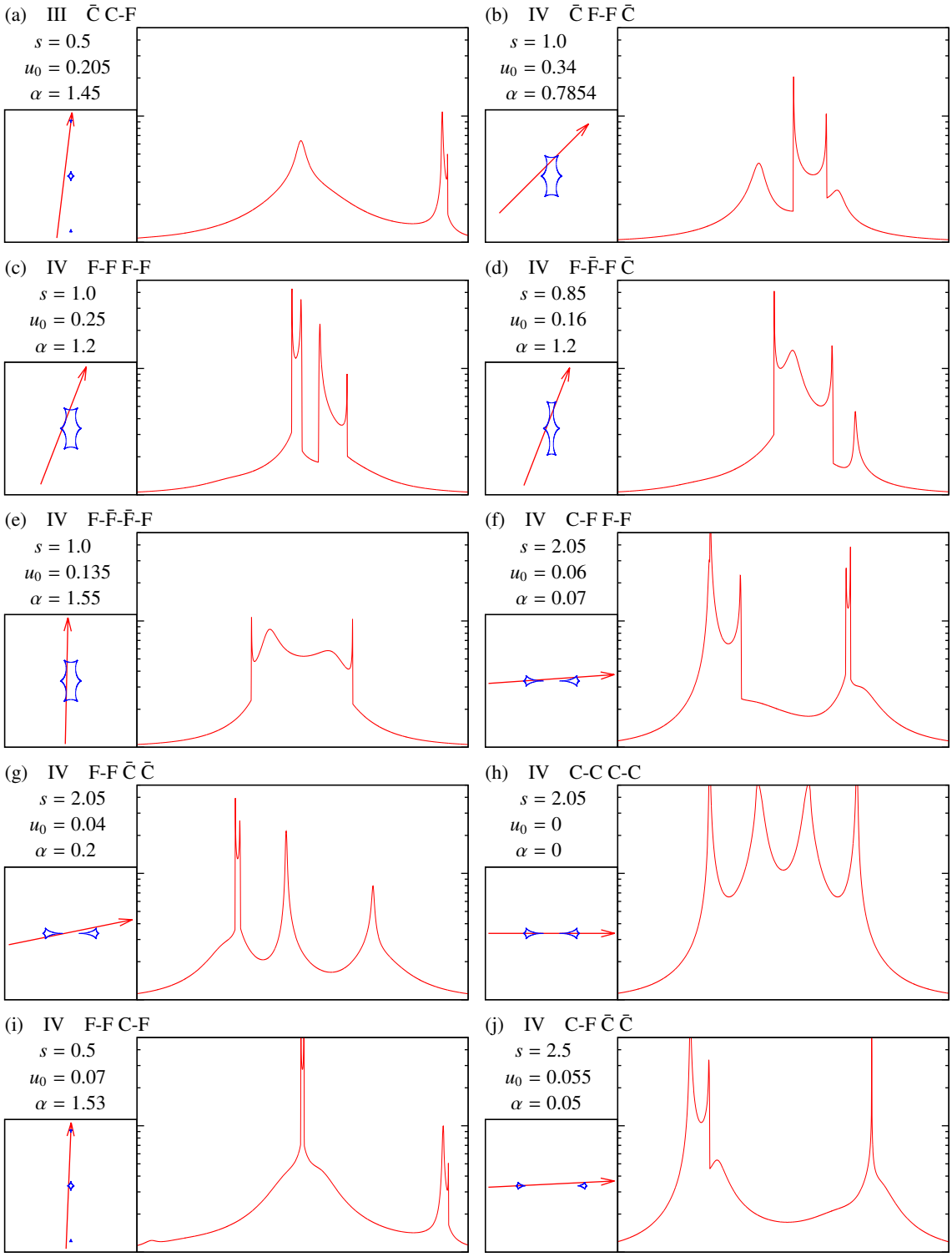

Figure 2.13: The lightcurve zoo. (Continued.)

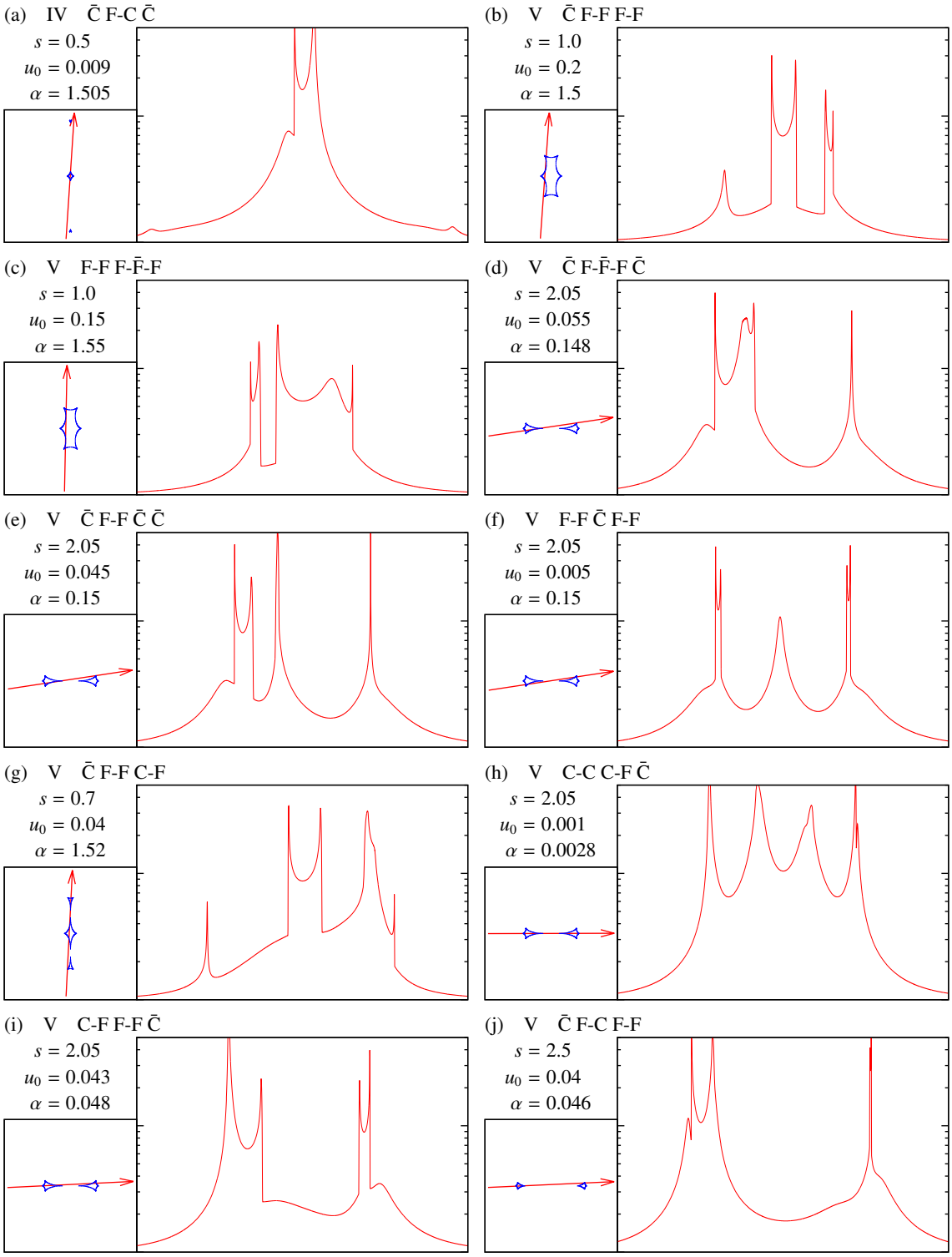

Figure 2.14: The lightcurve zoo. (Continued.)

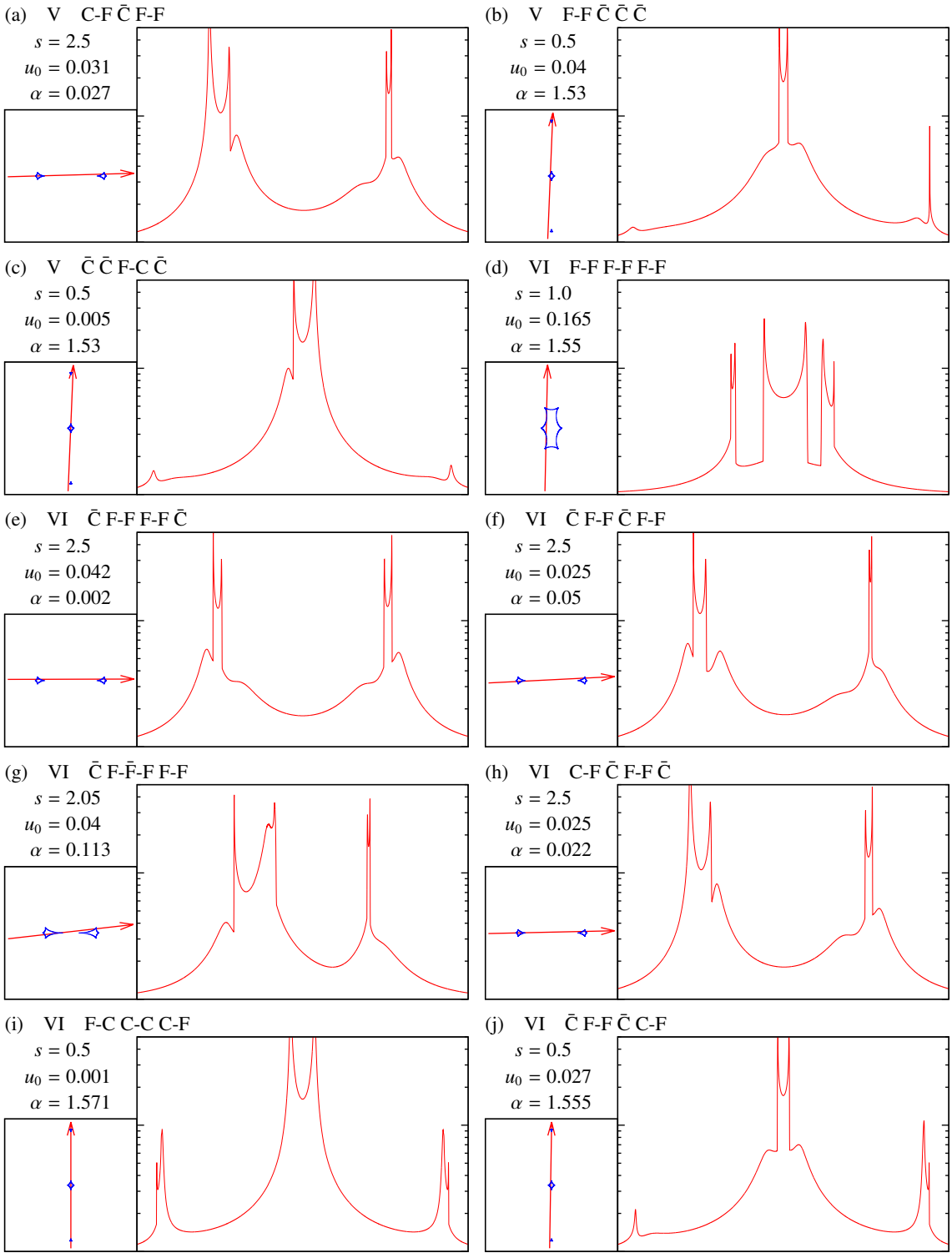

Figure 2.15: The lightcurve zoo. (Continued.)

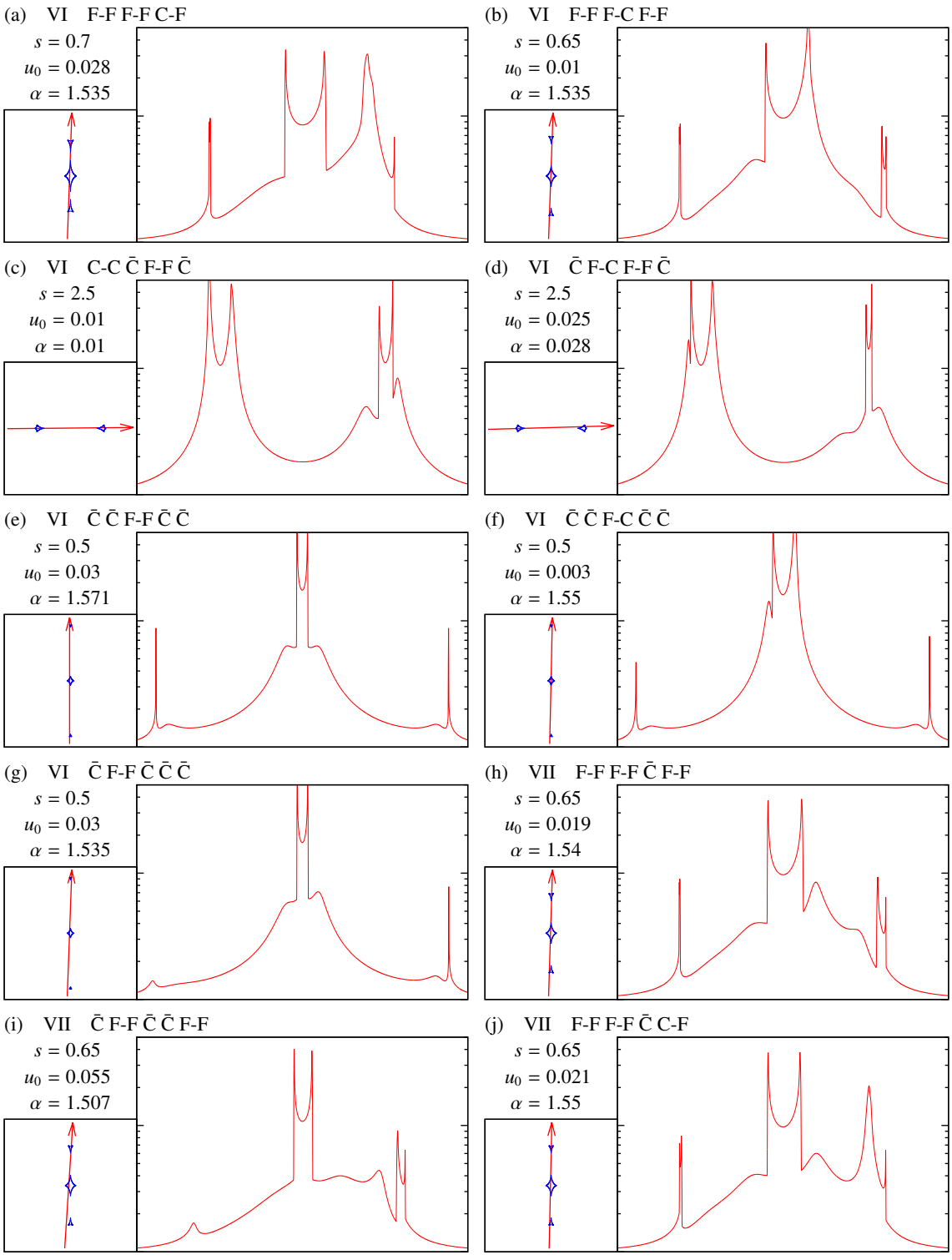

Figure 2.16: The lightcurve zoo. (Continued.)

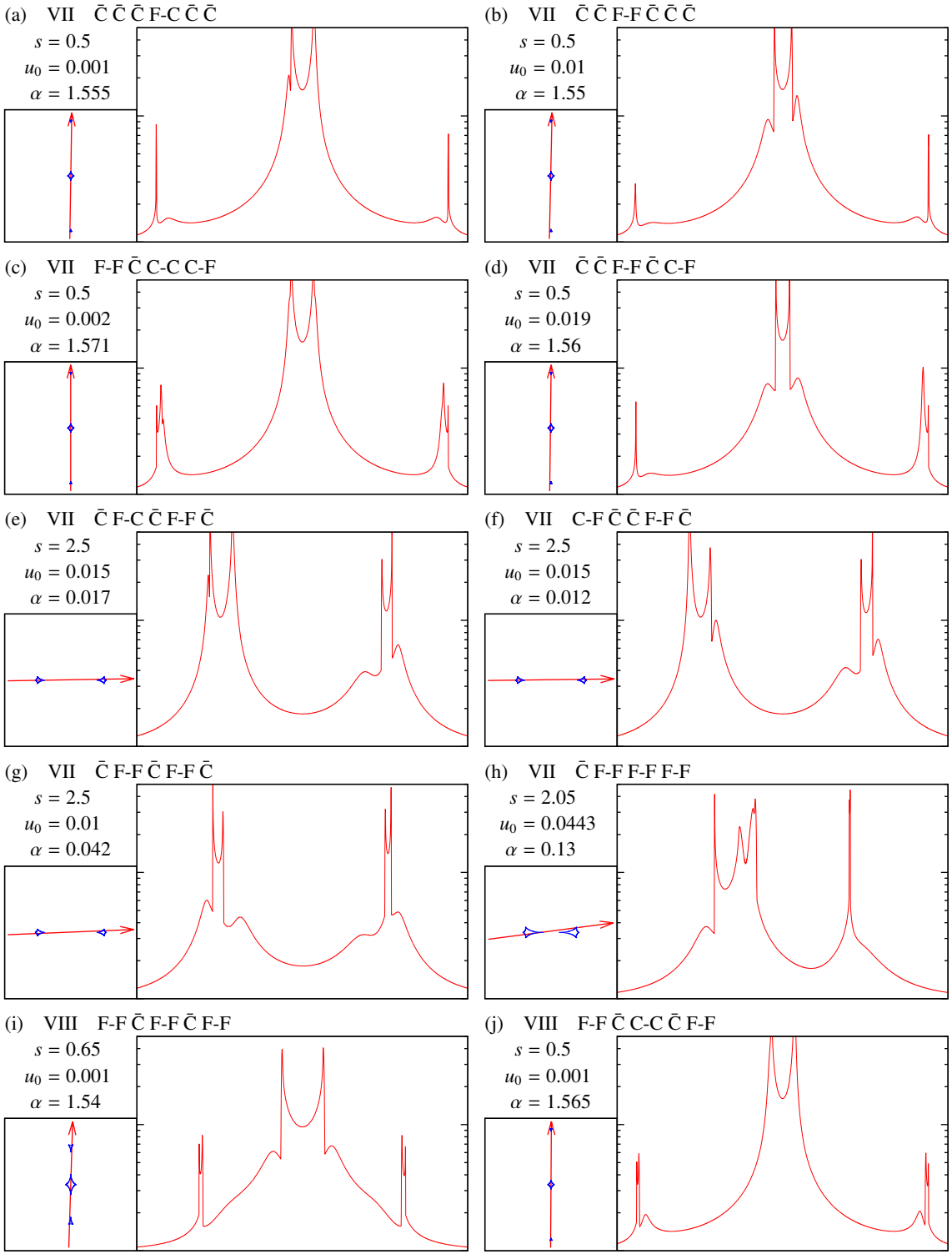

Figure 2.17: The lightcurve zoo. (Continued.)

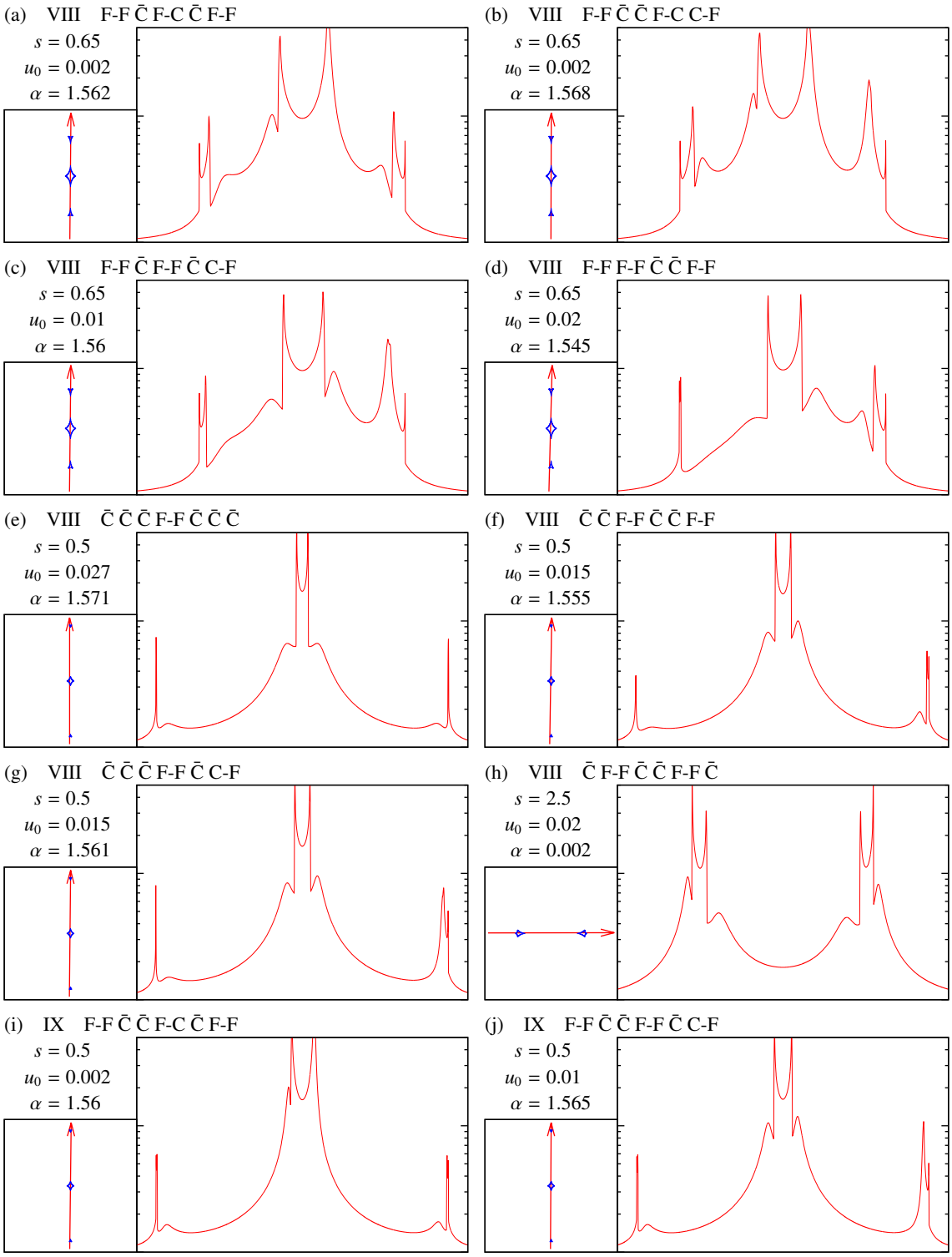

Figure 2.18: The lightcurve zoo. (Continued.)

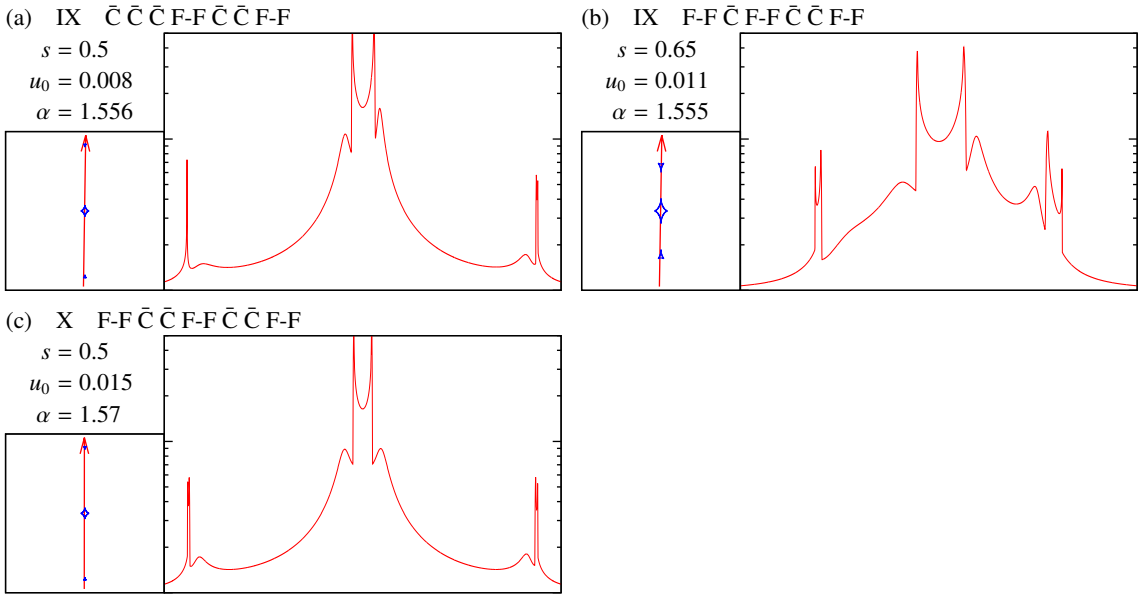

3

Exoplanetary microlensing

"Starfleet to scoutship, please give your position, Over.
I'm in orbit around the third planet from the star called the Sun, Over.
You mean it's the Earth? Over.
Positive. It is known to have some form of intelligent species. Over.
I think we should take a look."

Third Stone From The Sun - Jimi Hendrix

Although Einstein himself did not believe in the possibility of observing a microlensing event, in 1986 Paczyński found out that, if the dark halo of the Galaxy is made of massive compact (halo) objects (MACHOs), the probability that a distant source undergoes microlensing is about 10^{-6}, considering as best targets the stars in LMC (Paczyński, 1986). Subsequently, Paczyński (1991) found that the optical depth, i.e. the probability for a background source to undergo microlensing by at least 0.3 mag, toward the Galactic bulge stars visible in the *Baade's window*[1], on ordinary disc stars, is $\tau \sim 4 \times 10^{-7}$. Anyway, he concluded that the duration of the events, the optical depth, and then the number of events detected per year, would have changed according to the nature of the stars populating the disc. A time scale of 17 days is expected considering lenses with mass of 0.1 – 1.0 $M_{\odot}$, with a predicted average number of detected events of $\sim$ 4 per year per 10^6 bulge stars. For lenses of 0.001 – 0.01 $M_{\odot}$ the time scale is 7 days, with a rate of 17 events per year per 10^6 bulge stars. By considering less massive lenses, the duration of the events becomes shorter while the event rate increases until the limit case of 1.5 hr time scale with a rate of $\sim 2 \times 10^3$ events per year per 10^6 bulge stars, for a hypothetical large population of Mercurys in the Galactic disc, i.e. the smallest mass able to produce

[1] A region of the Galactic bulge ($l = 1°.02$, $b = 3°.92$ in Galactic coordinates) toward the Sagittarius constellation, with relatively low amount of interstellar dust, thus characterised by low extinction.

a detectable microlensing effect (see also Dominik, 2010, for considerations on the planetary detection efficiency).

Mao &Paczyński (1991) extended the discussion by proposing to look for microlensing of Galactic bulge stars produced by binary lenses in the Galactic disc, since it is well established that the majority of the stars in the Galactic disc are in binary systems (Abt, 1983). They found that about 10% of all microlensing events observed towards the Galactic bulge would have strongly shown the binary nature of the lens, and that the presence of a planet as a less massive companion orbiting the primary lens would have been detectable in up to 5% or 10% of all microlensing events. They predicted about two planet discoveries per year.

3.1 Finding planets with microlensing

A planetary companion perturbs the lightcurve of the single lens microlensing. The caustic shape changes according to s and q. For instance, we are considering the three topologies for the case of a planetary system with mass ratio $q = 0.001$, simulating the $M_J/M_\odot$ ratio. The radius of the considered source is $\rho_* = 0.002$ as in the case of the binary lightcurve classification, which should resemble a main sequence/subgiant star in the bulge. By using Equations (1.23) and (1.24) we find that the transition between the close and the intermediate topology occurs at $s = \sqrt{\frac{91^{1/2}}{11}} \sim 0.93$, while the transition to the wide topology occurs at $s = \frac{11}{91^{1/2}} \sim 1.15$. As we can see in Figure 3.1, the three topologies appear definitely different from the ones shown in the case of the equal mass ratio, although the caustics are still not self-intersecting.

There are mainly two channels which can lead to the discovery of a planetary anomaly in the lightcurve: high-magnification, and planetary caustic perturbations.

1. *High-magnification events*
   When the impact parameter is small ($u_0 \ll 1$), the flux of the source undergoes very high amplification, since the amplification goes approximately as $A(t) \sim u_t^{-1}$, showing anomalies at the peak if there are any planetary companions to the main lens. Following this kind of events is convenient since they can be monitored on the peak also with middle/small class (> 0.30 m) telescopes, and the behaviour of the lightcurve can be predicted in advance, then the peak perturbation, caused by the interaction between the source and the central caustic, occurs in a well-defined time window. Although such events are rare and the perturbations are relatively small (additionally, binary sources can easily contaminate the lightcurve), the method is highly sensitive to the presence of giant planets and to Earth-size planets, when they lie at the distance of $\sim r_E$ (which corresponds to a few AU, when considering the lens geometry and mass ratios we used so

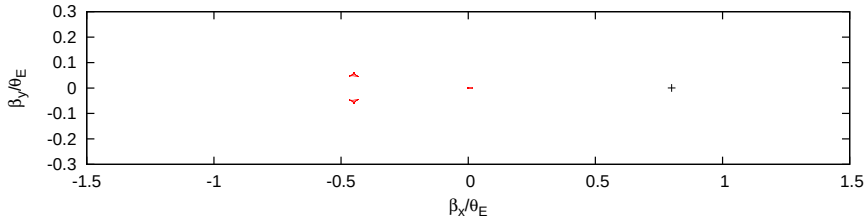

(a) Close topology caustics for $s = 0.8$ and 0.001. There is one central 3-cusp caustic and two 3-peak planetary caustics on the opposite side with respect to the planet.

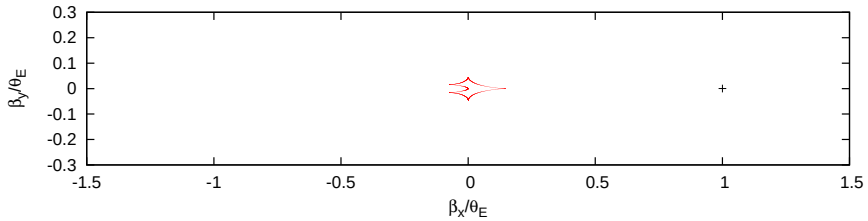

(b) Intermediate topology caustic for $s = 1.0$ and $q = 0.001$. There is only one 6-cusp caustic close to the position of the host star.

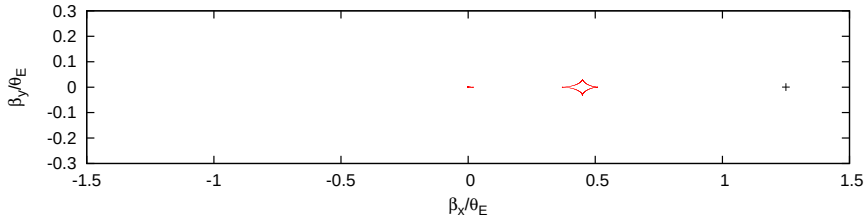

(c) Wide topology caustics for $s = 1.25$ and $q = 0.001$. The biggest part of the preceeding caustic separates towards the planet and, on the right part of the panel, the planetary caustic arises.

Figure 3.1: Topology transitions in the planetary case: the primary lens is placed at the center of each frame, at the position (0,0), while the position of the planet is indicated by the cross.

far), and this method is largely adopted since the community can rely on a large number of middle/small class telescopes for the follow-up and the anomaly monitoring.

2. *Planetary caustic perturbations*
   Looking at Figure 3.1, it is clear that planetary caustics span larger areas, in the magnification pattern, than the one occupied by the central caustic, and the planetary caustic crossing causes large perturbations in the lightcurve. It is impossible to know well in advance when a source will enter a caustic, then, in order to catch the planetary caustic lightcurve feature, we need to densely sample the whole lightcurve. This kind of events usually undergo low amplification and, even if they are more common, the possibility to observe the rare phenomenon of a planetary caustic crossing is diminished by the fact that it is more difficult to observe low-magnification events with small telescopes.

3.1.1 Exoplanetary lightcurve morphologies and the wide/close degeneracy

By comparing the lightcurve arising from a planetary event with the simple extended source and point lens (ESPL) model, we can have an idea of the anomalies which characterise this specific microlensing case. The variety of lightcurve morphologies is enriched with more complex scenarios with respect to the equal-mass binary microlensing, since the magnification pattern shows more and non-symmetric features, and it is worth a look at some examples among the three planetary topologies. In Figure 3.2 we have six different source trajectories in the close topology caustic ($s = 0.8$). The six tracks are defined by $\alpha_0 = \pi/4$ and $u_0 = 0.0$, –0.1, –0.2, –0.3, –0.4, –0.5. Figures from 3.3(a) to 3.3(f) show how the lightcurves, corresponding to the source tracks in Figure 3.2, change.

By moving from $u_0 = 0.0$ to $u_0 = -0.5$ we notice how the perturbation becomes clearer and the magnification tends to decrease. As we said before, the evolution of a low-magnification event, with a planetary caustic perturbation, is slower than the evolution of a high-magnification event with a central caustic perturbation. The mosaic in Figure 3.3 depicts the transition between this two kinds of typical planetary microlensing lightcurves.

The central caustic perturbation characterises the high-magnification lightcurve $u_0 = 0.0$ in Figure 3.4. As one can see, the perturbation is small, but the lightcurve clearly deviates from the point lens lightcurve.

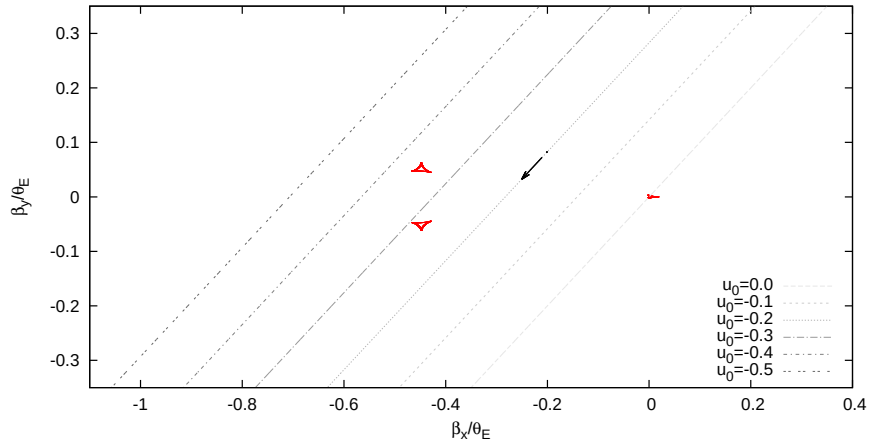

Figure 3.2: Six source tracks moving from the top right to the bottom left of the panel, with a source radius $\rho = 0.002$. The tracks include the central caustic interaction ($u_0 = 0.0$) and the planetary caustic interaction ($u_0 = -0.2, -0.3, -0.4$).

The intermediate topology occurs for $\sqrt{\frac{91^{1/2}}{11}} < s < \frac{11}{91^{1/2}}$ ($\sim 0.93 < s < 1.15$). The morphology variety is large, but we choose $s = 1.0$ and see what happens for three u_0 values, when the source interacts with the resonant caustic (the one arising from the merging of the central caustic with the planetary caustics) at impact parameters $u_0 = -0.1$, $u_0 = -0.1$, and $u_0 = 0.1$ (Figure 3.5(a)), and see how the magnification changes in these three cases. In Figure 3.5 we have all the three trajectories and the corresponding lightcurves.

We can see how for $u_0 = -0.1$ (Figure 3.5(b)), the lightcurve shows similar features to the planetary caustic perturbation of the close topology (Figure 3.5(c)) due to the source crossing a region of negative magnification. The scenario changes at $u_0 = -0.01$: the small impact parameter causes high magnification peaks, and the double caustic entry/exit causes the "devil's horns" shape. Finally, at $u_0 = 0.1$, there is a very high magnification peak due to the cusp perturbation (Figure 3.5(d)).

By moving to the wide topology we choose $s = 1.25$. This specific value is chosen in order to show the so called close/wide degeneracy, which we will describe later. We are showing just two examples of lightcurves corresponding to the source tracks in Figure 3.6 with $u_0 = 0.0$ and $u_0 = 0.3$. The two examples, summarised in Figure 3.7, show once again the difference between the central caustic (Figure 3.7(a)) and the planetary caustic (Figure 3.7(b)) perturbations. The latter exhibits a double-peaked anomaly due to the planetary caustic crossing. On the other hand, the trajectory intersecting the central caustic gives rise to a lightcurve very similar to the one in Figure 3.4. The degeneracy arising between lightcurves for $s_{close} = 1/s_{wide}$, where s_{close} and s_{wide} are two separation values for the close and the wide regime, is called close/wide

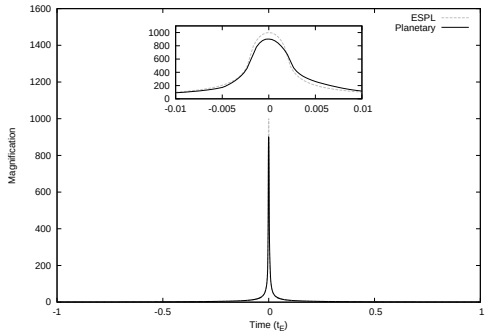

(a) $u_0 = 0.0$, $\alpha_0 = \pi/4$: the central caustic perturbed lightcurve.

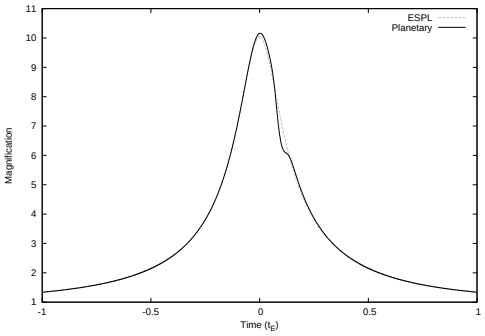

(b) $u_0 = –0.1$, $\alpha_0 = \pi/4$

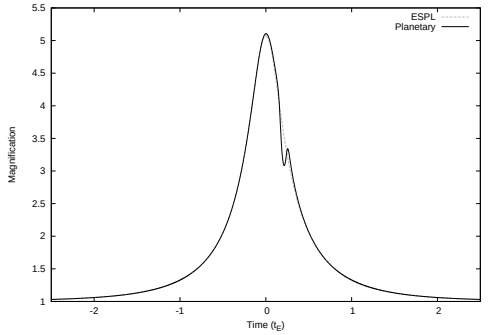

(c) $u_0 = –0.2$, $\alpha_0 = \pi/4$

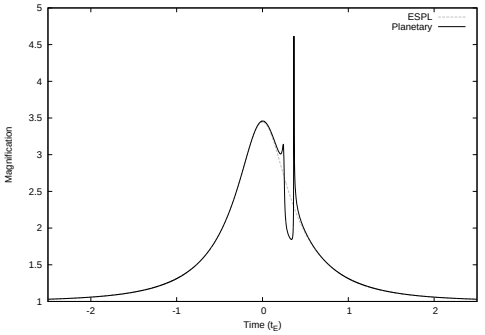

(d) $u_0 = –0.3$, $\alpha_0 = \pi/4$: a clear example of planetary caustic perturbation.

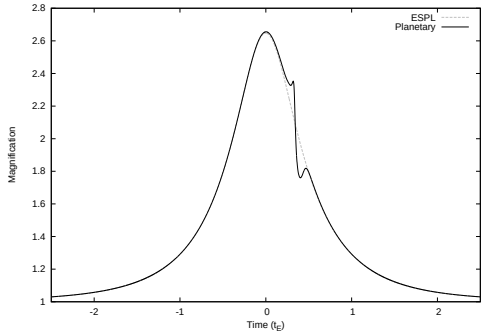

(e) $u_0 = –0.4$, $\alpha_0 = \pi/4$

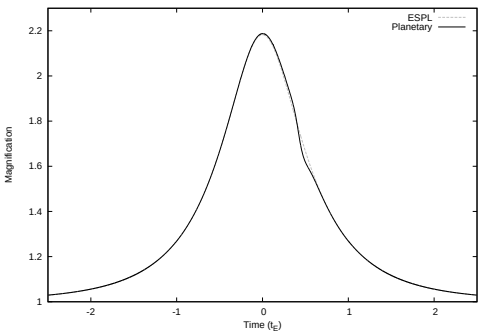

(f) $u_0 = –0.5$, $\alpha_0 = \pi/4$

Figure 3.3: Lightcurves arising from the source tracks in figure 3.2. Time in t_E on x-axis and magnification on y-axis.

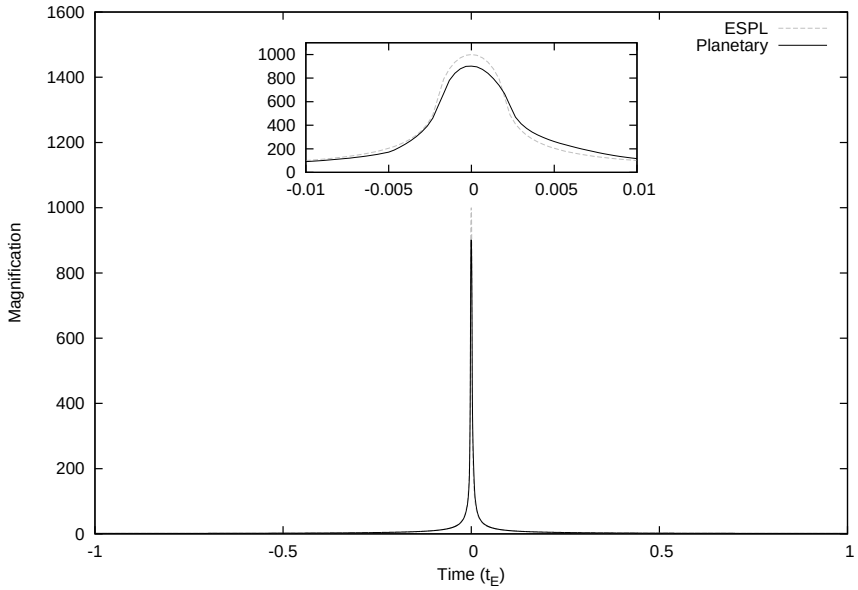

Figure 3.4: Central caustic perturbation ($u_0 = 0.0$, $\alpha_0 = \pi/4$). The example shows a high-magnification event lightcurve with a perturbation affecting the peak. Time in t_E on x-axis and magnification on y-axis.

degeneracy, as it is practically impossible to distinguish a close topology lightcurve from a wide one when $q \ll 1$ and s is far from 1. The two cases shown in Figures 3.4 and 3.7(a) are a clear example of the degeneracy described.

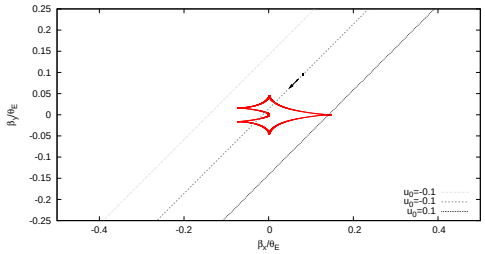

(a) Three cases in which the source interacts with the resonant caustic.

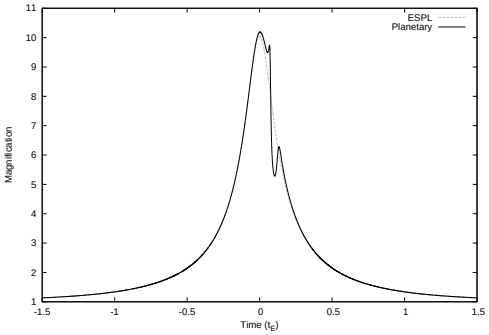

(b) $u_0 = –0.1$, $\alpha_0 = \pi/4$.

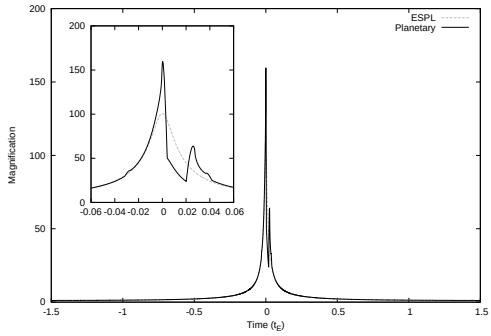

(c) $u_0 = –0.01$, $\alpha_0 = \pi/4$.

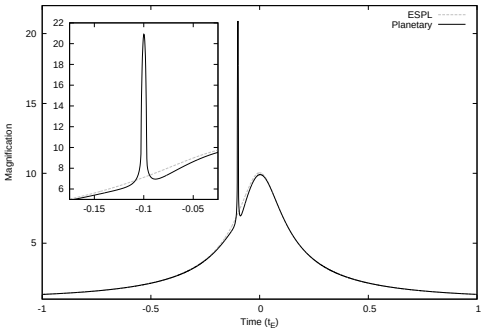

(d) $u_0 = 1$, $\alpha_0 = \pi/4$.

Figure 3.5: The intermediate topology at $s = 1.0$. In the panels (b), (c), and (d), time in t_E on x-axis and magnification on y-axis.

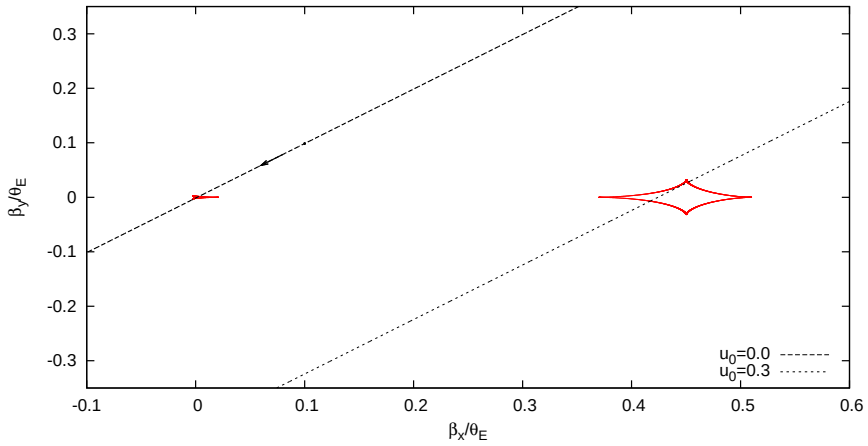

Figure 3.6: Two examples of trajectories in the wide topology ($s = 1.25$) showing the the central caustic perturbation (degenerate with the close topology case) at $u_0 = 0.0$, and the planetary caustic perturbation at $u_0 = 0.3$.

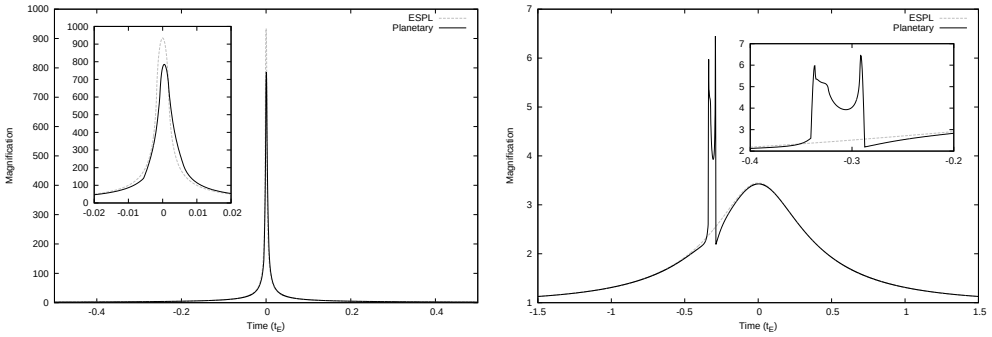

(a) $u_0 = 0.0$, $\alpha_0 = \pi/4$.

(b) $u_0 = 0.3$, $\alpha_0 = \pi/4$.

Figure 3.7: Lightcurves arising from the planetary wide topology ($s = 1.25$). Time in t_E on x-axis and magnification on y-axis.

Finally, it is interesting to see what happens when the planet is smaller. When passing from a planetary mass ratio of 0.001 (i.e. $M_J/M_\odot$) to a mass ratio of 3×10^{-6} (similar to the Earth-Sun mass ratio), we can appreciate how the duration of the anomaly due to the presence of an Earth-mass planet orbiting the primary lens is clearly shorter (tipically 0.5 hr) than the anomaly due to a Jupiter-mass planet. Figure 3.8 shows the comparison between the two lightcurves in the close topology.

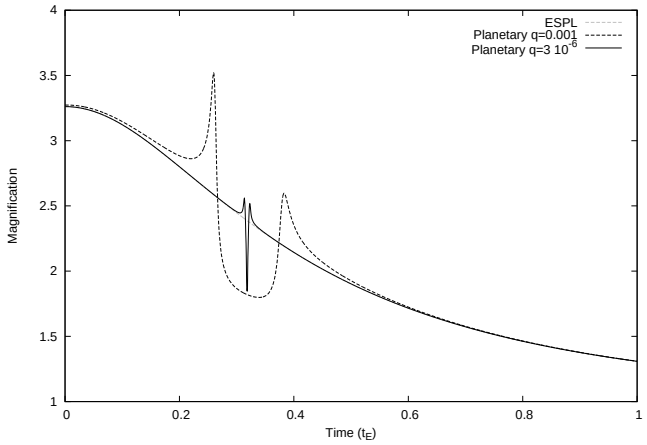

Figure 3.8: Comparison between two anomalies due to the presence of a Jupiter-mass planet and an Earth-mass planet. Time in t_E on x-axis and magnification on y-axis.

3.2 Microlensing observations towards the Galactic Bulge

3.2.1 Microlensing survey experiments

The Optical gravitational Lensing Experiment (OGLE) is one of the two principal microlensing surveys started in 1992 (Wyrzykowski et al., 2014). The 1.3 m Warsaw Telescope is placed at the Las Campanas Observatory, in Chile. In the newest phase of the survey (OGLE-IV), the telescope is equipped with a 32 detector CCD mosaic covering a field of view of 1.4 $\deg^2$. For the microlensing, frames are taken in Johnson-Cousin *I* band filter. The OGLE Early Warning System (EWS) is designed for detecting ongoing microlensing events. From the very first stage of the experiment, EWS was able to detect an increasing number of events, and in the last observing season (2014) the number of events detected by OGLE has been of 2049.

MOA (Microlensing Observations in Astrophysics) collaboration is a joint collaboration between Japan and New Zealand, started in the 1995 (Sako et al., 2008). In the newest upgrade, the experiment makes use of a 1.8 m telescope installed at Mt John University Observatory, in New Zealand. The telescope is equipped with a ten CCD detector mosaic covering a field of view of 2.2 $\deg^2$ with a single exposure in wide-band red filter. In the 2014 observing season, MOA alerted 621 events.

These two collaborations continuously monitor the Galactic bulge every year during its annual observability window from March to November, alerting more than 2000 events per year in total, well beyond the most optimistic predictions by Paczyński.

Starting from 2015, another survey experiment will be monitoring the sky. The KMTNet (Korea Micro-lensing Telescope Network) consists of a net of three 1.6m telescopes with a field of view of 4 $\deg^2$ each, and installed at Cerro Tololo Inter-American Observatory (CTIO), South Africa Astronomical Observatory (SAAO), and Siding Spring Observatory (SSO) in Australia (Moon et al., 2011). This ambitious and promising experiment is designed in order to observe the Galactic bulge round-the-clock and is going to give a prominent contribution in the years to come.

3.2.2 Follow-up observations

The short duration of a planetary anomaly makes the detection not a simple task to accomplish. For example, the presence of a Jovian size planet orbiting a Sun-like star causes a perturbation of about one day, while we talk of less than 1 hr for an Earth-like planet. This means that in order not to miss any important features in the lightcurve, we need to ensure the maximum coverage of (at least) the most promising events. And, so far, the microlensing community had played in cooperation in order to maximise the number of planet discoveries.

For the purpose, two aspects are crucial:

- *Round-the-clock follow-up observations;*
- *Real-time modelling.*

There are several different follow-up collaborations which cooperate in order to follow the events alerted by OGLE and MOA. I was involved in the MiNDSTEp (Microlensing Network for the Detection of Small Terrestrial Exoplanets) consortium for the years 2012, 2013, and 2014. Observations were conducted at the 1.54m Danish telescope installed at La Silla (Chile, ESO Observatory), but also at the Salerno University Observatory (SUO) 0.35m telescope. The follow-up campaigns usually start in March/April and end in October.
The second follow-up collaboration in which I was involved is the RoboNet project, a network of currently six observatories including three 2m telescopes sited in Hawaii, eastern Australia, and Canary Islands, and nine 1m telescopes sited in Chile, South Africa, eastern Australia, and Texas. The telescopes are fully robotic and the network allows to densely monitor the Galactic bulge for an effective observing time of more than 24 hr per day, due to the superposition of the observing time windows of each site.
MiNDSTEp and RoboNet strategies are strictly dependent on ARTEMiS (Automated Robotic Terrestrial Exoplanet Microlensing Search, Dominik et al. (2010)), a web platform that collects all the data from surveys and follow-up collaborations and which is able to manage the priority of the most promising events to be followed relying on the SIGNALMEN immediate anomaly detector (Dominik et al., 2007). I will now concentrate on the Salerno University Observatory campaigns.

3.2.3 Salerno Observatory ML campaigns 2012-2014

Salerno University Observatory is located in the university campus of Fisciano (Salerno, Italy) at coordinates: Latitude 40°46'30" N, Longitude 14°47'20" E, 300 m asl. The observatory is fully operational since March 2011 and it is equipped with a 0.35m Celestron C-14 telescope on a GM-4000 HPS mount with a 15" pointing accuracy. The CCD camera is a SBIG ST-2000XM with a resolution of 1600×1200 pixels, and the field of view is 14'×11'. The telescope is used principally for observations of microlensing events within the MiNDSTEp consortium and transiting exoplanets within the KELT (Kilodegree Extremely Little Telescope) collaboration.

The telescope is located at a latitude that still allows a visibility window of the Galactic bulge from February to November (usually, the campaign starts on April 1st and closes on October 31st, but few extra observing nights outisde this time interval are not excluded). The duration of the daily visibility window goes from a minumum of 1 hr at the beginning/end of the season and reaches the duration of almost 7 hr around middle June. The Northern latitude

at which our telescope is located could permit possible measurements of terrestrial parallax by comparing our lightcurves with the ones observed from the southern emisphere.

Our observing strategy is based on the ARTEMiS scheduler. From the ARTEMiS priority list, we select the most promising events and perform the follow-up of targets with magnitude lower than 15.5 at declination -20°, 15 at declination -25°, 14.5 at -30°and so on.

Dedicated software controls the dome and the telescope motion, the CCD camera, the focuser and the pointing. In addition, a pipeline reduces the data in real-time.

Data coming from the telescope are then immediately reduced and analysed with a PSF-fitting method, and the photometry is sent directly to ARTEMiS in order to be plotted together with the data coming from other telescopes and to be compared with the lightcurve theoretical model, in order to search or confirm an anomalous signature.

Each spool consists of a stack of 10 scientific frames with exposure time of 2 minutes each, taken in Bessel-*I* filter, for an effective exposure time of 20 minutes. The stacking allows to reduce the S/N ratio, improving the photometry even for low declination targets.

While in 2012 and 2013 we used to follow one event per night, since 2014 the observations are managed with SUObot, a software developed by Valerio Bozza, which allows us to manage the follow-up of more events in the same night. The use of SUObot makes the observatory almost fully robotic. Each night, the software checks the ARTEMiS priority list and selects three events according to our observing criteria and constraints. Then, with just an initial human interaction in order to select the best focus, SUObot manages the pointing and the cadence of observations for the three selected events. The implementation of SUObot has dramatically increased the number of events we can follow during the year.

3.2.3.1 2012 observing campaign

The 2012 observing season started on June 1st and ended on September 30th. In total, 13 events were followed, with in particular one event followed for 31 nights:

- OGLE-2012-BLG-0176 is a long PSPL event characterised by parallax effect;
- OGLE-2012-BLG-0798 is a moderate amplification event due to a single lens, which we observed during the descent and for which the finite source effect is clear and also polarimetry measurements, carried out at the Liverpool telescope, are available; this could give the opportunity of studying the source atmosphere (see Ingrosso et al., 2012);
- OGLE-2012-BLG-1523 is an interesting binary event.

3.2.3.2 2013 observing campaign

The 2013 observing season was longer than the previous one, since it started on May 17th and ended on October 31st, with 90 good nights out of 168. 13 events were followed, and in particular:

- OGLE-2013-BLG-1394 has been followed for 53 nights (883 frames) and, modelled by this author, it showed binary source signature with xallarap (see the following chapter);
- OGLE-2013-BLG-0911 was a high-magnification event with probable planetary signature;
- OGLE-2013-BLG 0446 was a high-magnification event with parallax and a debated possible planetary signature:
- OGLE-2013-BLG-0798 was a binary lens event.

3.2.3.3 2014 observing campaign

The longest and most productive observing season to date was the 2014 one, when we observed since March 12th until November 3rd for a total of 105 good nights out of 214. With the introduction of SUObot, the number of events followed increased up to 49, with 29 good-sampled events. In particular:

- OGLE-2014-BLG-0494/0589/0879/0944 are ordinary events, included in a study by Calchi Novati et al. (2014) on parallax measurements via terrestrial and Spitzer observations;
- OGLE-2014-BLG-1112 is a slow evolution binary event and it will be followed during the 2015 observing season in order to confirm planetary signature;
- five more binary and four high-magnification events could be of interest for publication.

3.3 Analysing ML events

The flux measured during the observations is a combination of two components: the actual flux F_s by the source and the blending flux F_b. The latter quantity includes the flux produced by every other unresolved object but the source, like a source companion, background stars, or the lens itself. Due to the crowded field we usually are pointing at, blending is almost always present in our measurements. Since the source is magnified by a time-dependent amount $A(t)$

related to the relative motion between source and lens, the observed flux is the time-dependent quantity (Dominik, 2010)

$$F(t) = F_s A(t) + F_b \, . \tag{3.1}$$

It is important to have measurements of the same field from more than one site and in different filters, because the fraction of blended light changes according to the bandpass. Besides, the different instrumental resolution of the observatories could also affect the blending and help in isolating the actual amplified flux of the source. The total number of degrees of freedom is then $N_{nl} + 2 \times N_O$ (Gaudi, 2011), where N_{nl} is the number of non-linear parameters included in Equation (3.1) (such as s, q, t_0, t_E, u_0, α_0, and ρ_*, in the "simple" case of the static binary lens), and $2 \times N_O$ is the number of total independent datasets for F_s and F_b. All these parameters are normally degenerate (Dominik, 2009), and Woźniak &Paczyński (1997) have already shown for the static single lens how u_0, t_0 and F_s, tend to draw highly correlated patterns in the χ^2 diagrams.

3.3.1 Lightcurve fitting

While estimates of the source flux F_s and the blended flux F_b can be found by using a least-squares fit, the non-linear parameters require more sophisticated techniques.

The most efficient way to reduce the degeneracies is to perform a thorough and well-structured analysis of the parameter space. Especially in the case of the binary lens, which includes the planetary solution, many different sets of parameters can lead to the same lightcurve. A good sampling can help in catching even minimal features and in discarding some of the degenerate solutions.

In the off-line analysis, a brute-force approach is often time-consuming and needs powerful computing facilities. One good approach could be to first scan the parameter space with a routine which minimises the χ^2, like a downhill fitting. The choice of well-distributed initial seeds can come from a lightcurve library like the one we have presented in Chapter 2. Then, once we have obtained a first set of solutions, we can densely probe the surrounding regions in the parameter space by initialising Markov Chains and including also non-static parameters whenever the residuals show that the models found do not fit the observed data properly. Introducing more parameters in the modelling of an event usually further minimises the χ^2. In the next chapter, we will treat the practical case of the modelling of OGLE-2013-BLG-1394.

4

OGLE-2013-BLG-1394

"They got music in their Solar System
They've rocked around the Milky Way
They dance around the Borealice
They're space truckin' everyday"
Space Truckin' - Deep Purple

In 2013, the OGLE collaboration detected 1987 microlensing events. On July 26th, the OGLE EWS alerted the event no. 1394 in the OGLE-IV BLG639.05 field at the coordinates (J2000) RA 17:50:25.86, DEC -24:34:57.3 (see Figures 4.1 and 4.2 for OGLE-IV field mosaic and OGLE-2013-BLG-1394 finding chart).

4.1 Data

While the baseline and the alert of the microlensing event come from OGLE, the follow-up observations started on Aug 7th (HJD 2456511.75) with the MiNDSTEp Danish 1.54m telescope and were performed from many different sites (Table 4.1).

The timeline of the most important steps of the observations is summarised in Table 4.2. The anomaly was alerted on September 15th 2013 at 00:33 UT by ARTEMiS, when the event was undergoing a Δmag $\sim$ 2 mag amplification and it was deviating from the PSPL model. A first bump was registered at 6554 (HJD-2450000) and the event evolved towards a second bump at $\sim$ 12.9 mag at 6566.5 (HJD-2450000). We followed the event from the Salerno Unversity Observatory from 6515.5 (HJD-2450000) to 6596.5 (HJD-2450000) for a total of 53 nights with 883 frames. Overall, considering the data coming from OGLE, MiNDSTEp, RoboNet and μFUN, we have baseline data points since 2010 and a good sampling of the event for the 2013 season with a very good coverage of the magnification peak, and finally we also have

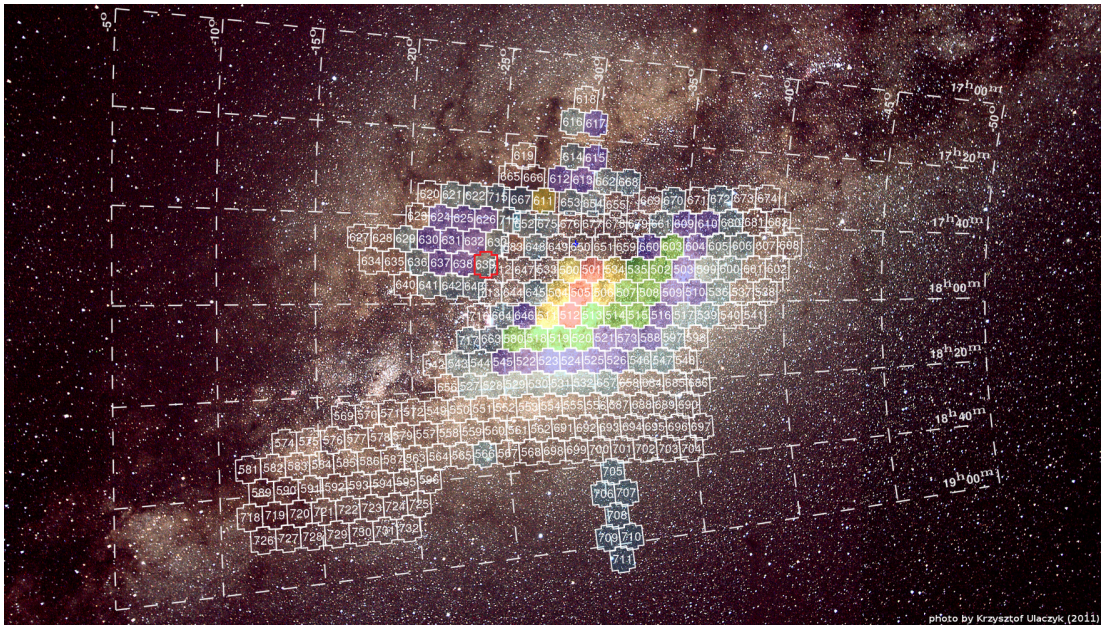

Figure 4.1: OGLE-IV survey fields. Red fields are those with high-cadence. Field BLG639 (highlighted in red) is a low cadence field, with 1 observation every 2 nights. *From OGLE webpage: photo by Krzysztof Ulaczyk and plot by Jan Skowron.*

HJD-2450000	Observatory (filter)	Site	Team
5267.68-6791.81*	Warsaw 1.3m (*I*)	Cerro Tololo (Chile)	OGLE
6511.75	Danish 1.54m (*I*)	La Silla (Chile)	MiNDSTEp
6512.92	LCOGT SAAO 1m A (*I*)	Sutherland (South Africa)	RoboNet
6512.92	LCOGT SSO 1m B (*I*)	Siding Spring (Australia)	RoboNet
6513.57	LCOGT CTIO 1m A (*I*)	Cerro Tololo (Chile)	RoboNet
6513.95	LCOGT SSO 1m A (*I*)	Siding Spring (Australia)	RoboNet
6514.50	LCOGT CTIO 1m A (*I*)	Cerro Tololo (Chile)	RoboNet
6516.33	SUO 0.35m (*I*)	Salerno University (Italy)	MiNDSTEp
6517.90	Faulkes South 2.0m (*I*)	Siding Spring (Australia)	RoboNet
6568.58	CTIO 1.3m (*I*)	Cerro Tololo (Chile)	μFUN
6568.58	CTIO 1.3m (*V*)	Cerro Tololo (Chile)	μFUN

Table 4.1: List of the collaborations which carried out the observations of OB1394. The first column indicates when observatories started taking data, except for the first line which indicates the time range of the dataset by OGLE.
*Baseline taken since 2010, and 2014 data included

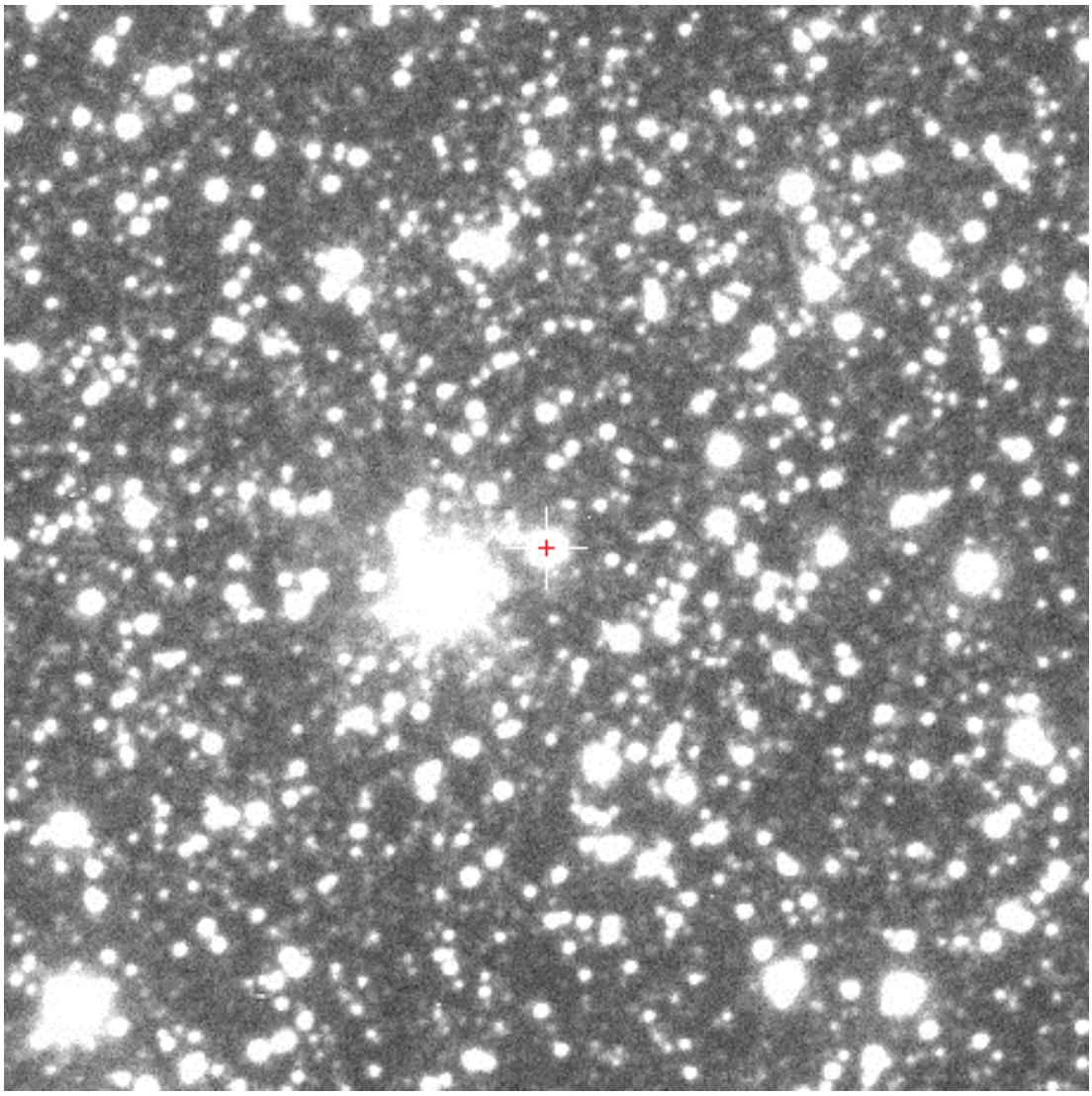

Figure 4.2: OGLE-2013-BLG-1394 finding chart. The red cross indicates the star undergoing microlensing. By looking at the crowded field, it is clear that the blending always affects our measurements and how important it is to achieve a very good optical resolution.

Date (HJD-2450000)	Description
6500.21	OGLE EWS announces the ongoing microlensing event on OGLE-2013-BLG-1394
6550.52	Anomaly detected by ARTEMiS (SIGNALMEN)
6550.57	First real-time model circulated by RTModel (Valerio Bozza)
6579.49	First spectrum taken with Clay 6.5m Magellan Telescope at Las Campanas
6931.49	Second spectrum taken with Clay 6.5m Magellan Telescope

Table 4.2: OB1394 timeline.

2014 data from OGLE covering the descent. All the groups carrying out the follow-up have real-time pipelines for the reduction of the data, allowing to figure out the behaviour of the event in real-time. Once the observing season ended, all the collaborations have made their re-reduced datasets available.

The first model circulated to the community, just one hour after the anomaly alert, was from RTModel by Valerio Bozza. This model predicted, among the possible solutions, a binary lens with a mass ratio ~ 0.02, but real-time modelling changes every time we add a new data point, and with such a slow event the final model remained uncertain, awaiting a deeper offline investigation.

In October 2013 and September 2014, spectral measurements were carried out at the Clay 6.5m Magellan Telescope, at Las Campanas (Chile), in order to shed light on the nature of the source. As we will see later (Section 4.2.3), spectral measurements are crucial for those events which manifest ambiguous anomaly and, in this case, the two measurements revealed the binary nature of the source.

Figure 4.3 shows the data taken during the 2013 observing season. The plot is produced with the ARTEMiS plotter and shows the data points collected by the follow-up collaboration, the anomaly monitoring follow-up telescopes, and the additional data taken in V-bandpass by μFUN.

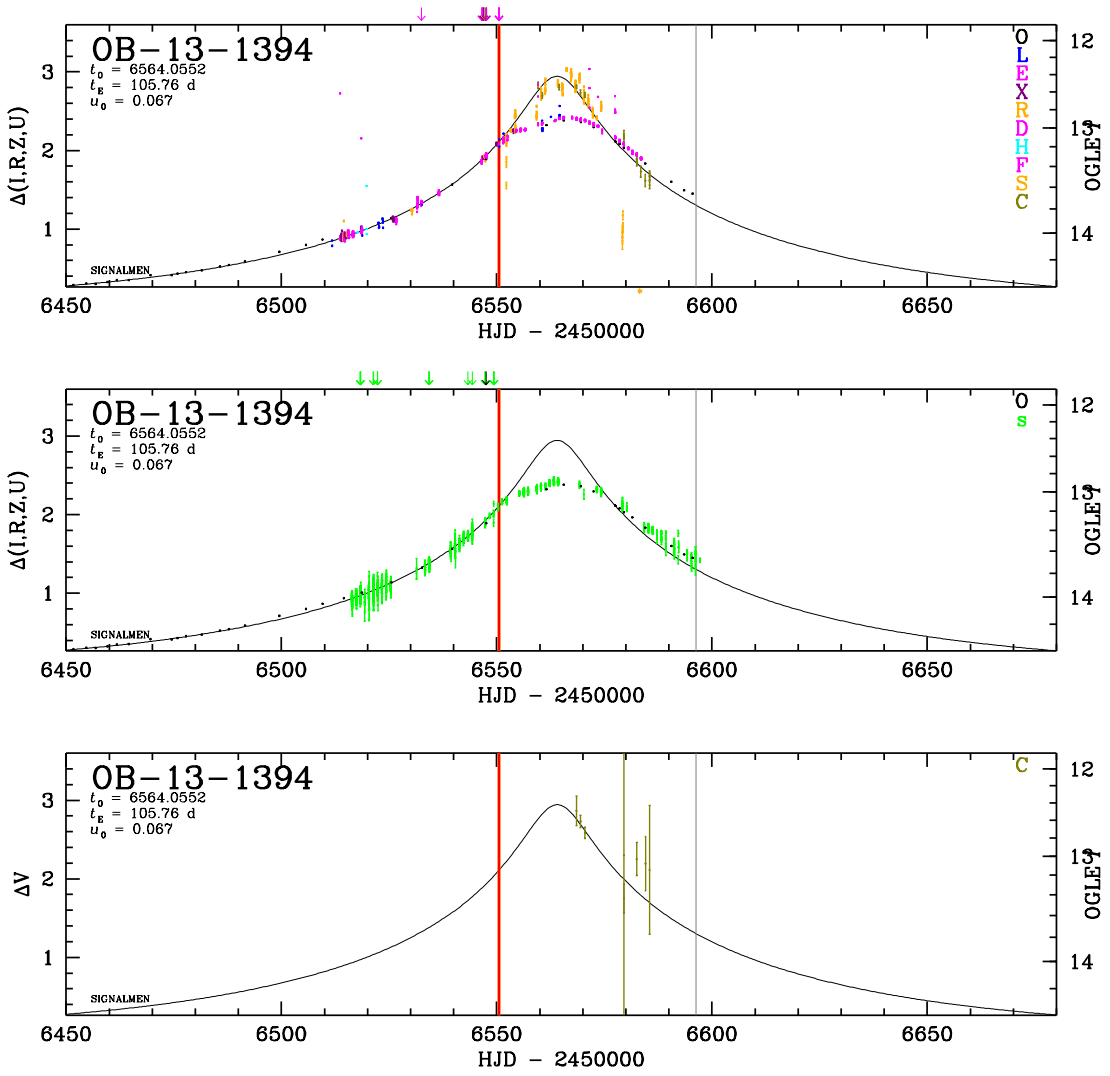

Figure 4.3: OB131394 lightcurve observed in 2013. The solid black line in the background represents the PSPL theoretical fit (the parameters are on the upper left), the red line indicates the SIGNALMEN anomaly trigger (alerting when the observed lightcurve deviates from the PSPL model), while the grey line indicates the last data point on the lightcurve. *Top panel*: lightcurve observed by the follow-up collaborations. *Mid panel*: Salerno data showed as anomaly monitoring data. *Bottom panel*: Additional CTIO μFUN data, taken in V-bandpass.

4.2 Modelling

Starting from the last results coming from the real-time modelling, we can undertake a denser investigation by using Markov Chain Monte Carlo method. The routine we used in order to model the event exploits a contour integration code (by Valerio Bozza) in order to simulate lightcurves.
For a given set of parameters (lens static/non-static parameters and source size/track information), the contour integration code is a routine in C++ that solves the fifth-order polynomial associated to the lens equation (Section 1.3.2) with numerical methods (e.g., Laguerre's method) for each position of the source along its track. By sampling the boundary of a finite source, we can then retrieve the position and the contour of real images, by selecting those which satisfy the lens equation. The code makes use of the Green's theorem for evaluating the area S_i of each image so that the quantity $\Sigma_i S_i/S_*$ (where $S_* = \pi\rho_*^2$) evaluates the amplification at a specific source position. By iterating for each point of the source track we can simulate the lightcurve. The limb darkening effect can be simulated by representing the source with concentric circles in order to mimic the source brightness profile.
We first searched for binary lens and binary source static solutions, by exploring the parameter space with chains at high temperature with 1.6×10^5 steps, than we explored the local minima, if any, with colder MCMCs, in order to search for the solutions minimising the χ^2.
Due to the long duration of the event, we needed to introduce non-static effects taking into account the orbital motion of the lens/source systems and annual parallax. In order to model the features in the lightcurve attributable to such effects, we started from the best static solutions and used a grid in order to initialise additional MCMCs for a dense exploration of subregions in the parameter space. We first introduced the two parallax parameters and then the three orbital motion parameters.
Since the lightcurve showed no clear evidence of a caustic crossing, we decided not to include a limb darkening model at the early stages of the modelling. We subsequently did not include limb darkening, because the supervening spectral measurements made further investigation of planetary models useless.

It is worth looking at how parallax and orbital motion affect the source trajectory and the topology of the lens:

- *Parallax*
  The effect due to the Earth motion around the Sun is proportional to the parallax $\pi_E \equiv 1\mathrm{AU}\frac{D_S - D_L}{D_S D_L}\theta_E$ and it is observable whenever the duration of the event makes the trajectory of the source, with respect to the lens, deviate from a straight line; the curvature of the trajectory is expressed by a vector of magnitude π_E, and the parameters we introduce

when modelling the parallax effect are the two components $\pi_{E\parallel}$ and $\pi_{E\perp}$, parallel and perpendicular to the source trajectory respectively, of π_E;

- *Orbital motion and xallarap*
  The parameters we introduce are $\frac{d\alpha_0}{dt}$ and $\frac{ds}{dt}$, which express how the trajectory inclination and the lens separation change with time, as an effect of the Newtonian motion of the binary lens (orbital motion) or the binary source (xallarap), and ω_3, which is the longitudinal component of the velocity normalised to the magnitude of the angular velocity.

4.2.1 Binary lens models

In Table 4.3 we summarise the best binary lens solutions, while in Figure 4.4 we have the three corresponding source tracks and caustics. It is apparent, by looking at the χ^2, that by adding the high-order effects we obtain a better fit, and we will show later (Section 4.3) the comparison between the residuals of all the solutions. The best model, with parallax and orbital motion, proposes an intermediate topology system with planetary mass ratio. The two bumps in the lightcurve (see Figure 4.5(b)) would be then justified by the two cusp grazings (Figure 4.4(c))

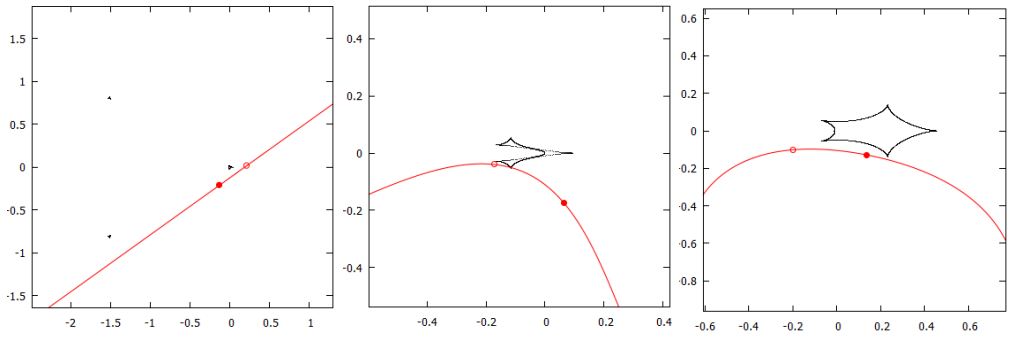

(a) Binary lens. (b) Binary lens + parallax. (c) Binary lens + parallax and orbital motion.

Figure 4.4: Sourcetracks for the three binary lens models found. The source, represented by the circle, moves from the empty circle to the filled one.

We show the best fit model, including parallax and orbital motion, with residuals in Figure 4.5, and the correlation plots for the parameters in Figure 4.6.

	Binary Lens	Parallax	Parallax+Orbital Motion
s	0.468056 ± 0.008593	0.943417 ± 0.002118	1.121460 ± 0.014828
q	0.049808 ± 0.003341	0.001241 ± 0.000095	0.014157 ± 0.001763
u_0	0.105349 ± 0.001915	–0.091602 ± 0.003110	–0.104099 ± 0.004272
θ (rad)	0.586225 ± 0.005269	2.62835 ± 0.01965	3.034440 ± 0.035729
ρ_*	0.000190 ± 0.002706	0.029510 ± 0.001893	0.023996 ± 0.002069
t_E (days)	109.096 ± 1.517	166.142 ± 5.380	124.149 ± 3.313
t_0 (HJD†)	6565.24 ± 0.05	6567.00 ± 0.06	6570.10 ± 0.44
$\pi_\perp$	–	0.384678 ± 0.010245	–0.144687 ± 0.009152
$\pi_\parallel$	–	–0.039048 ± 0.005366	0.036266 ± 0.009152
ds/dt	–	–	0.002940 ± 0.000689
$d\alpha_0/dt$	–	–	0.005805 ± 0.001382
ω_3	–	–	0.005705 ± 0.001632
f_b/f_s	2.02 ± 0.07	2.87 ± 0.13	2.50 ± 0.14
χ^2	1118.79 ± 3.18	1066.11 ± 3.84	1000.51 ± 4.48

Table 4.3: Comparison between the binary lens solutions, with the corresponding χ^2 and OGLE blending f_b/f_s.
†HJD-2450000

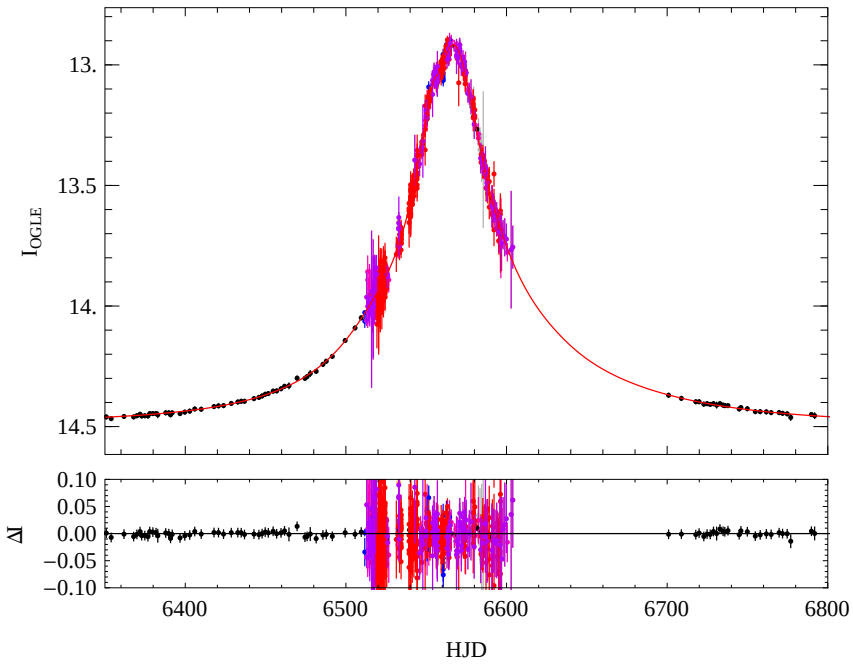

(a) Best fit including OGLE 2014 data (black dots on the right).

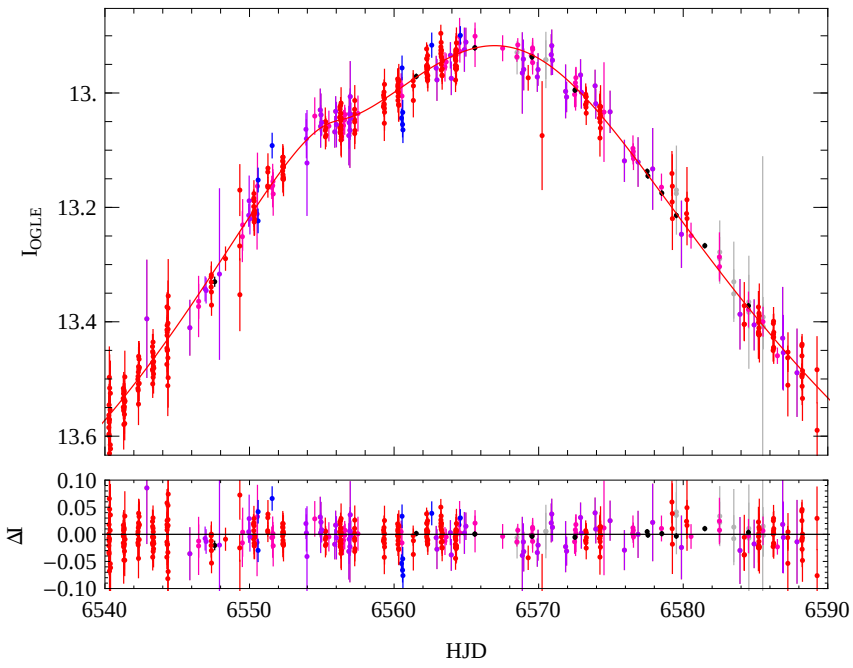

(b) Zoom of the peak showing the two bumps due to the cusp grazings.

Figure 4.5: Binary lens model, with parallax and orbital motion, best fit. At the bottom of each panel we show the residuals.

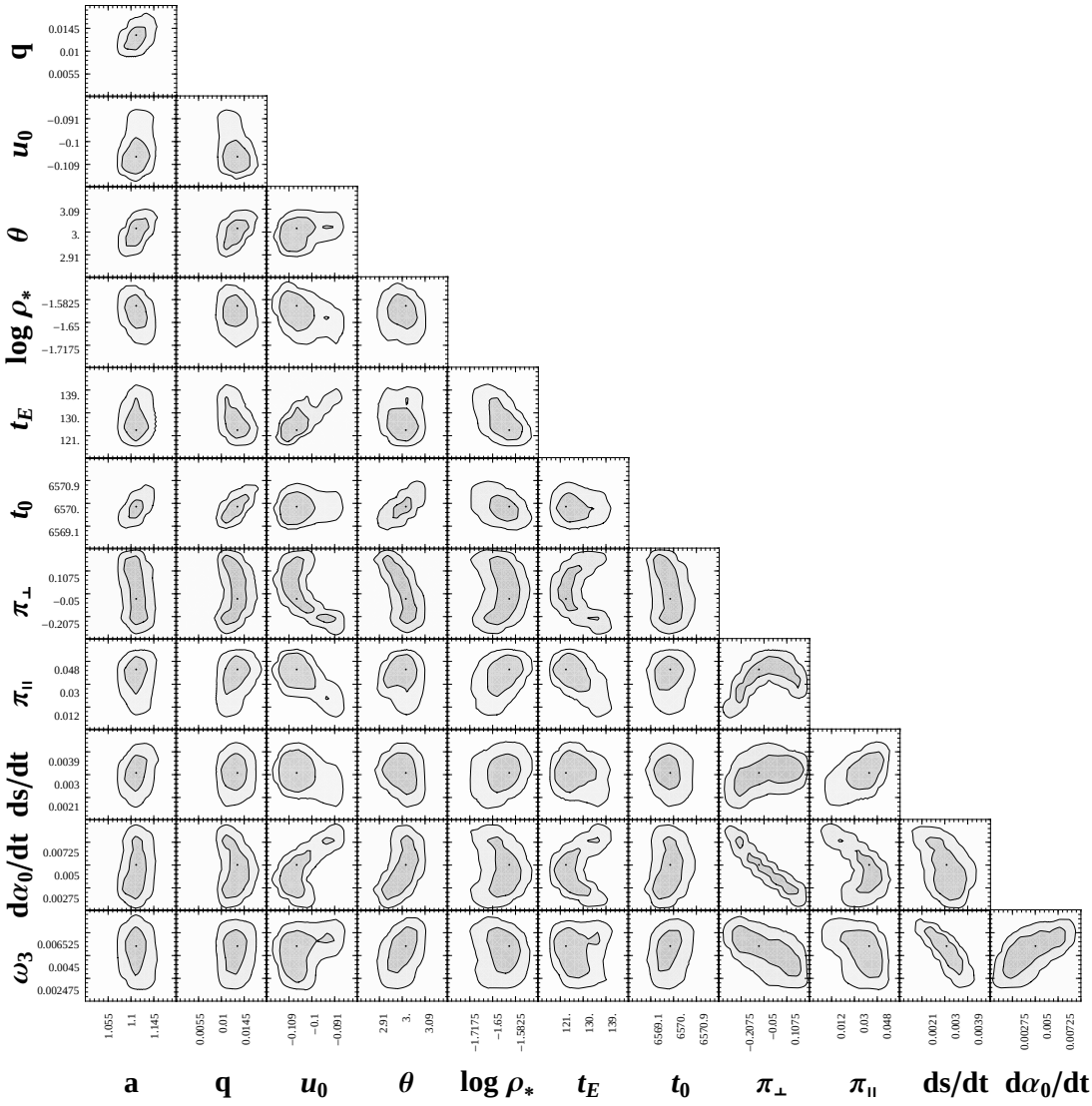

Figure 4.6: Correlation plots show how the model parameters are cross-correlated. The lighter regions indicate the 68% confidence interval, while the darker regions indicate the 95% confidence interval

.

4.2.2 Binary source models

As we said in Section 1.3.2.2 the lightcurve of a binary source microlensing is the superposition of the two lightcurves arising from the microlensing of each single component of the system. Like the case of the PSPL, t_E represents the Einstein time; FR indicates the source flux ratio F_2/F_1, while u_{01}, u_{02}, t_{01}, and t_{02}, represent the impact parameters and the time of maximum approach between the two sources and the lens; parallax parameters are the components of the annual parallax vector as in the cases shown above, while the orbital motion parameters are referred to the xallarap, since this time they describe the effect of the orbital motion of the source system.

The amplification, in the case of a binary source, is given by

$$A(t) = \frac{1}{1+FR}A_1(t) + \frac{FR}{1+FR}A_2(t) = \frac{1}{1+FR}\frac{u_1^2+2}{u_1\sqrt{u_1^2+4}} + \frac{FR}{1+FR}\frac{u_2^2+2}{u_2\sqrt{u_2^2+4}}\,, \tag{4.1}$$

where u_1 and u_2 are functions of time and depend on the same t_E:

$$u_i(t) = \sqrt{u_{0i}^2 + \frac{(t-t_{0i})^2}{t_E^2}} \quad (i = 1, 2)\,. \tag{4.2}$$

As we said for the case of the binary lens, parallax and orbital motion affect the source trajectory by making t_{0i} and u_{0i} change as a function of time, and then causing the asymmetric shape of the lightcurve.

We show below the binary source solutions (Table 4.4) with the best fit model, including parallax and xallarap effects, and corresponding residuals, in Figure 4.7. Figure 4.8 shows the correlation plots for the parameters of the best fit model.

	Binary Source	Parallax	Parallax+Xallarap
t_E (days)	107.42 ± 1.50	168.70 ± 7.96	156.35 ± 10.95
FR	0.081197 ± 0.008873	0.100580 ± 0.011250	0.040583 ± 0.007214
u_{01}	0.120497 ± 0.002588	0.066675 ± 0.003850	0.133596 ± 0.010580
u_{02}	0.046823 ± 0.002786	–0.019599 ± 0.003206	0.064698 ± 0.004085
t_{01} (HJD†)	6567.60 ± 0.11	6567.65 ± 0.10	6564.36 ± 0.29
t_{02} (HJD†)	6553.15 ± 0.12	6552.12 ± 0.11	6561.65 ± 1.06
$\pi_\perp$	–	0.324195 ± 0.012366	0.349086 ± 0.018719
$\pi_\parallel$	–	–0.007330 ± 0.005988	0.009685 ± 0.018281
ds/dt	–	–	–0.140080 ± 0.016256
$d\alpha_0/dt$	–	–	–0.130280 ± 0.018551
ω_3	–	–	0.003041 ± 0.000937
f_b/f_s	1.80 ± 0.07	4.23 ± 0.31	1.69 ± 0.27
χ^2	1181.30 ± 2.98	1046.32 ± 3.55	1001.90 ± 4.26

Table 4.4: Comparison between the binary source solutions, with the corresponding χ^2 and OGLE blending f_b/f_s.
†HJD-2450000

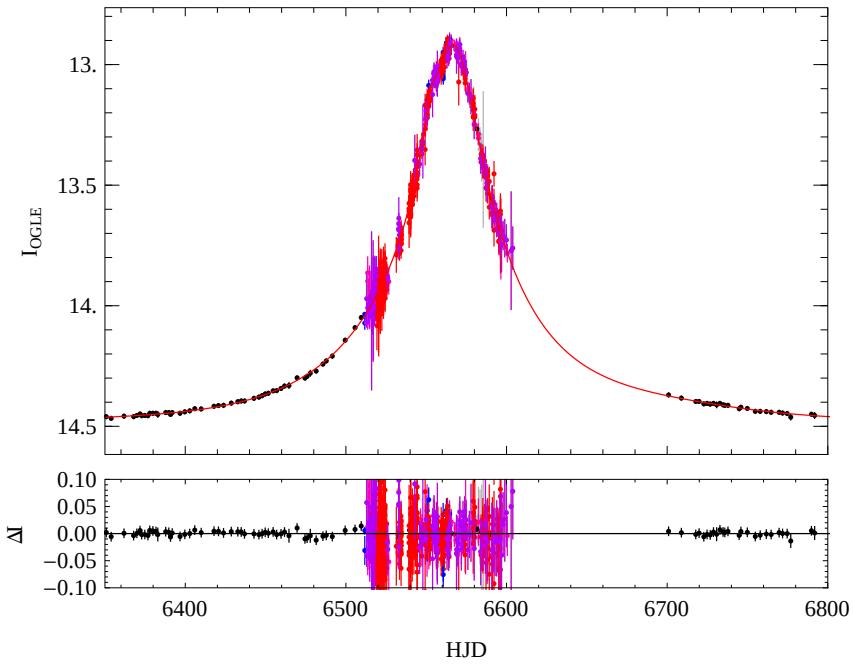

(a) Best fit including OGLE 2014 data (black dots on the right).

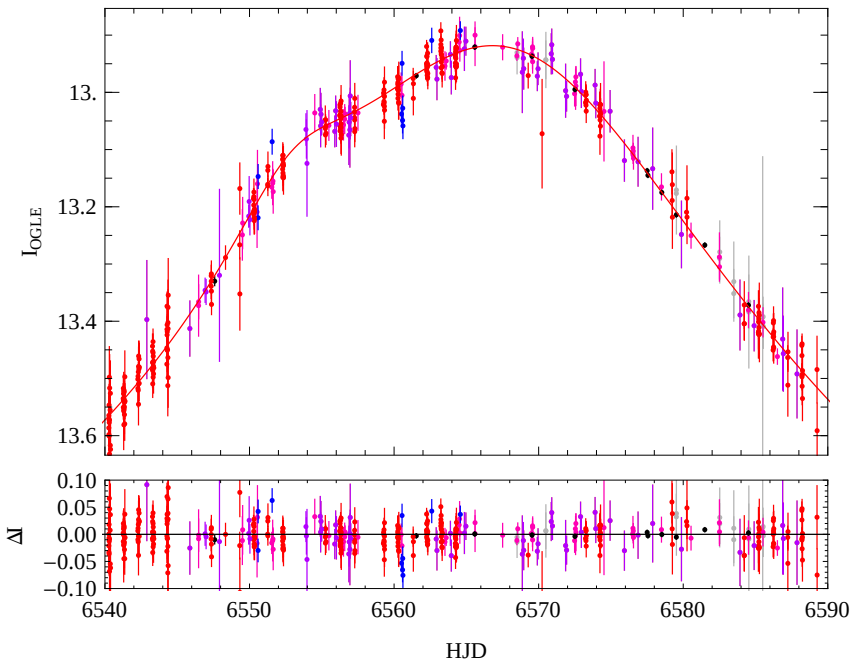

(b) Zoom of the peak showing the two bumps due to the cusp grazings.

Figure 4.7: Binary source model with parallax and xallarap best fit. At the bottom of each panel we show the residuals.

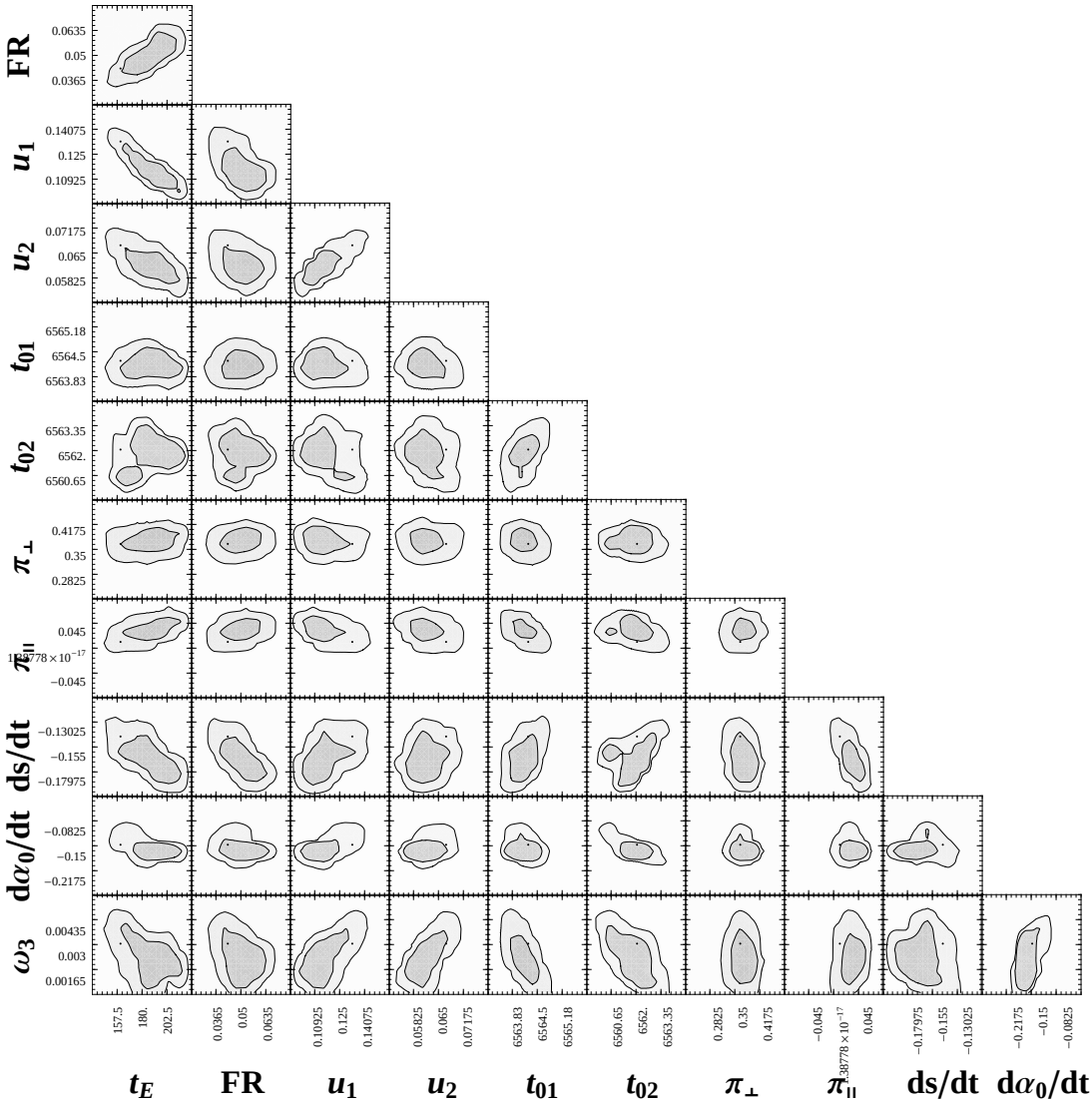

Figure 4.8: Correlation plots show how the model parameters are cross-correlated. The lighter regions indicate the 68% confidence interval, while the darker regions indicate the 95% confidence interval

.

While the binary lens solution with orbital motion and the binary source solution with xallarap show the same χ^2 (within the errors) and almost the same best-fit curve, by looking at the residuals, it seems that the former better fit the data. While I complete this PhD thesis, the exploration of the parameter space is still ongoing. So I do not exclude that a better fit for the binary source model is possible.

4.2.3 Spectral measurements

Table 4.5 shows the results of the spectroscopic measurements carried out in October 2013 and September 2014 by Ian Thompson at the Clay 6.5m Magellan Telescope.

HJD-2450000	v_1 (km/s)	v_2 (km/s)
6579.4925	4.56 ± 0.34	–25.87 ± 0.84
6931.4994	–24.51 ± 0.37	–11.0 ± 1.25

Table 4.5: The two peaks in the radial velocity measurement of the source revealed two components. The spectra have been observed, within one year of each other, on Oct 13th, 2013, and on Sep 30th, 2014.

These spectra showed two different velocity components in the two measurements, revealing that the source is definitely constituted by a binary system and that the two bumps in the lightcurve are due to the superposition of the two magnification peaks (Figure 4.9).

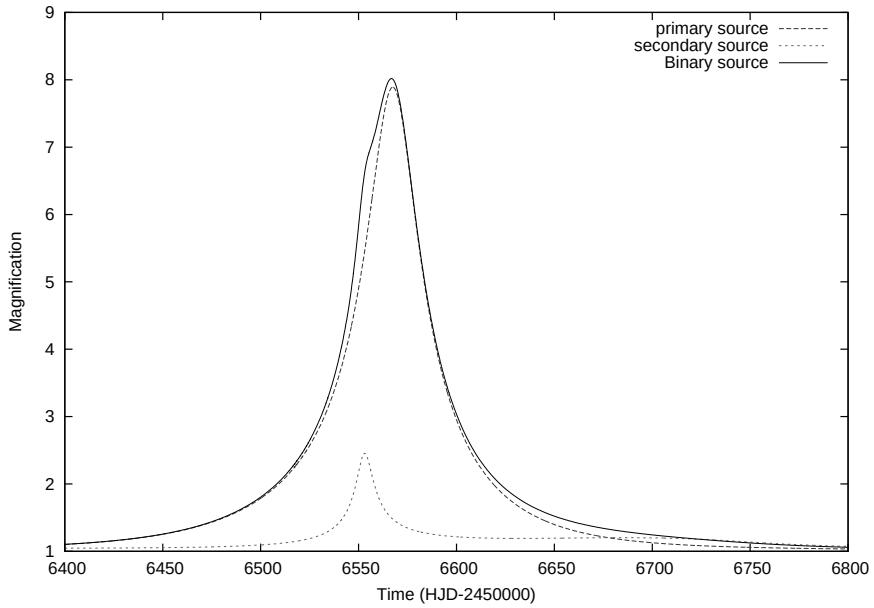

Figure 4.9: The superposition of the microlensing magnification on the two components gives the total magnification for the binary source.

4.3 Conclusions

OGLE-2013-BLG-1394 has been a puzzling event due to its weak anomaly. The MCMC modelling has shown that the models with smaller χ^2 were the ones which took into account high-order effects. We finally found two models with the same χ^2, one binary lens model with parallax and orbital motion, and one binary source model with parallax and xallarap. Figures 4.10 and 4.11 show the residuals comparison.

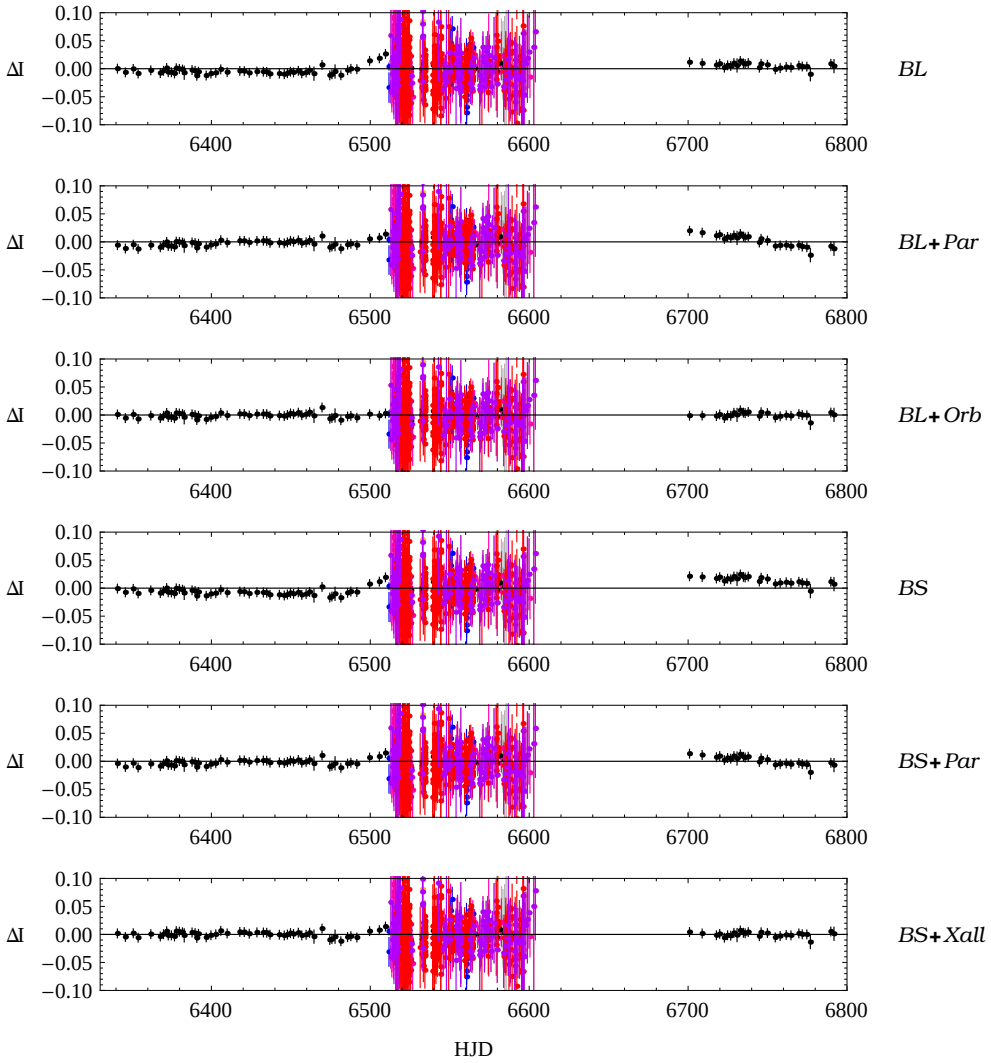

Figure 4.10: Residuals with also OGLE 2014 data (black dots on the right).

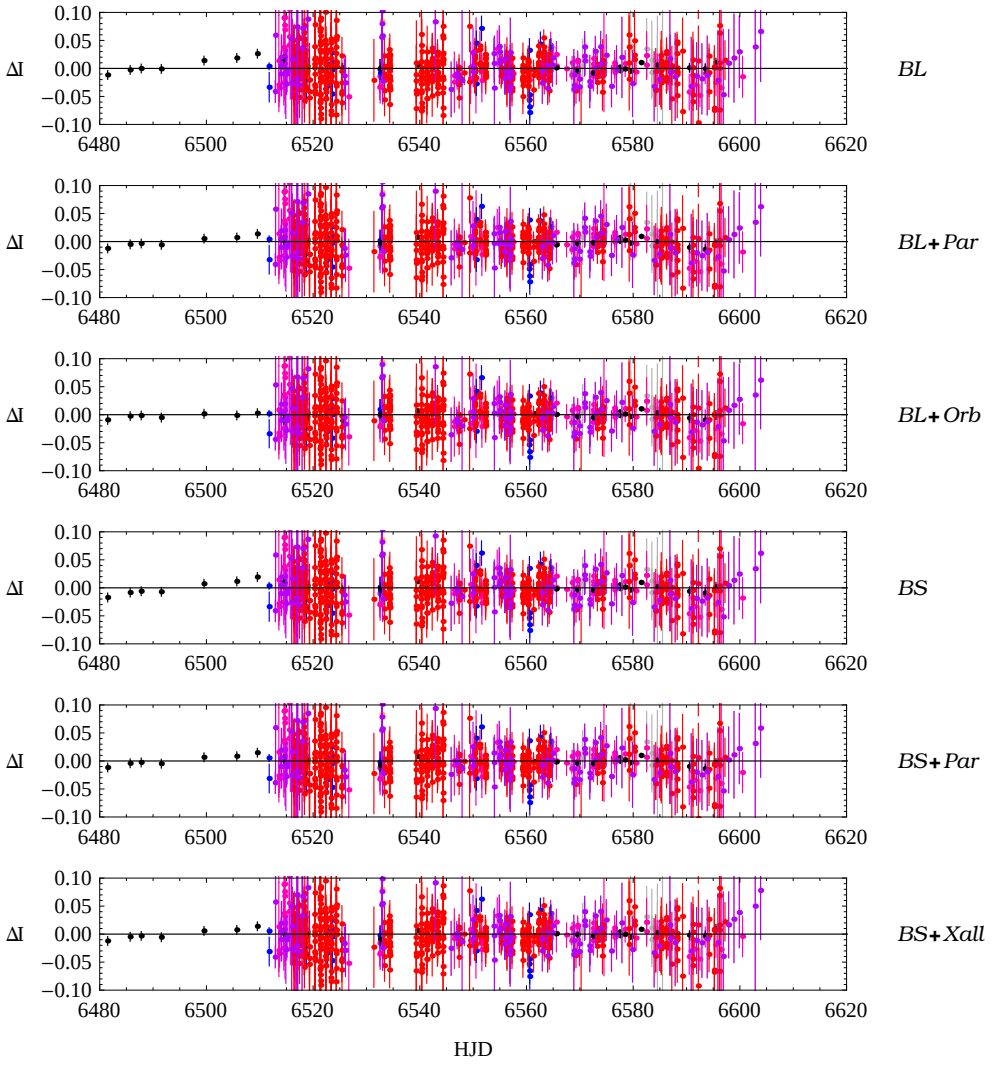

Figure 4.11: Highlight around the magnification peak. The binary lens with orbital motion model clearly fit OGLE data (black dots) between 6500 and 6510 (HJD-2450000).

Thanks to the spectral analysis we have been able to break the degeneracy between the two best solutions, revealing the binary nature of the source. The anomaly can be finally justified by considering the source as a binary system which undergoes a single lens microlensing. Currently, we are carrying out additional analysis in order to develop a complete physical interpretation of the microlensing event.

Nevertheless, we can state that the analysis conducted on this event draws our attention on the binary source/planetary lens degeneracy, and it could be worth stressing few points:

- it may be useful to carry out deeper analysis on events discarded due to weak anomalies, since binary sources contaminate events with no evident caustic signature;
- in some cases spectroscopic or multi-band measurements are crucial in order to reveal planetary lensing hidden behind ambiguous anomaly;
- a statistical study on past and ongoing microlensing events could be useful in order to better evaluate the binary source contamination rate, a very important factor to consider if we want to find the real planetary sensitivity for space missions like EUCLID and WFIRST.

5

Other methods for detecting exoplanets

"Oh! But it don't make no difference, babe, hey
And I know that I could always try
There's a fire inside everyone of us
You'd better need it now
I got to hold it, yeah
I better use it till the day I die"

Kozmic Blues - Janis Joplin

By studying microlensing events, we are able to detect planets in a specific region of the parameter space defined by mass and orbital radius, i.e. the region of planets beyond the snow line. For a complete investigation of such parameter space and a better knowledge of the statistical distrubution of the exoplanets, we have to use other methods which are sensitive to other regions of the parameter space.

We can summarise the most important as:

- *Transiting exoplanets (TEP)*
  Discovered by studing the eclipse due to the planet transit on the stellar disk;

- *Radial Velocities (RV)*
  This method exploits the doppler effect on the stellar spectra, in order to search for a planetary companion causing a periodic shift;

- *Direct imaging*

Planets distant from the host stars, could be directly detected with coronographic techniques;

- *Transit Timing Variation (TTV)*
  By measuring the changes in the timing of a transit, we are able to reveal the additional components of a multi-planetary system;

- *Pulsar Timing*
  The first planetary system discovered was by Wolszczan &Frail (1992) and it was discovered by measuring the variation in the timing of the pulsar PSR1257+12;

- *Astrometry*
  Even if we cannot see the planet, we observe stars wobbling around a point which can reveal the position of the centre of mass of a planetary system of which we cannot resolve the less massive and luminous components.

In the following sections, I will give a brief report of some transiting exoplanets which I have observed during the past years using the 1.54m Danish telescope in La Silla (Chile) and the 1.52 Cassini telescope in Loiano (Italy). Such observations were conducted in collaboration with John Southworth, Luigi Mancini and Simona Ciceri, in order to better characterise the physical parameters of known planets and to probe their atmosphere with spectrophotometric techniques.

Figure 5.1 shows the distribution of the known exoplanets in the parameter space defined by planetary mass and orbital radius. The plot clearly shows how some regions of the parameter space are dominated by a specific method of detection.
For instance, we can highlight:

- microlensing planets dominate the region from 1 to 10 AU, since it is the typical physical extension of the Einstein angle for lenses in the Galactic disk, corresponding to the maximum sensitivity to a planetary companion orbiting the primary lens;

- transiting exoplanets dominate around 1 M_J and between 0.01-0.1 AU, as this region is the one where hot-Jupiters, the planetary population tipically discovered with this method, are distrubuted;

- RV are almost uniformly distributed from 0.01 to 10 AU, but as the orbital radius rises, the mass detectivity threshold becomes higher, since the doppler effect due to the planetary companion is inversely proportional to the distance from the host star;

- the upper right of the plot is dominated by directly imaged explanets, which need to be distant from the host star in order to be detected.

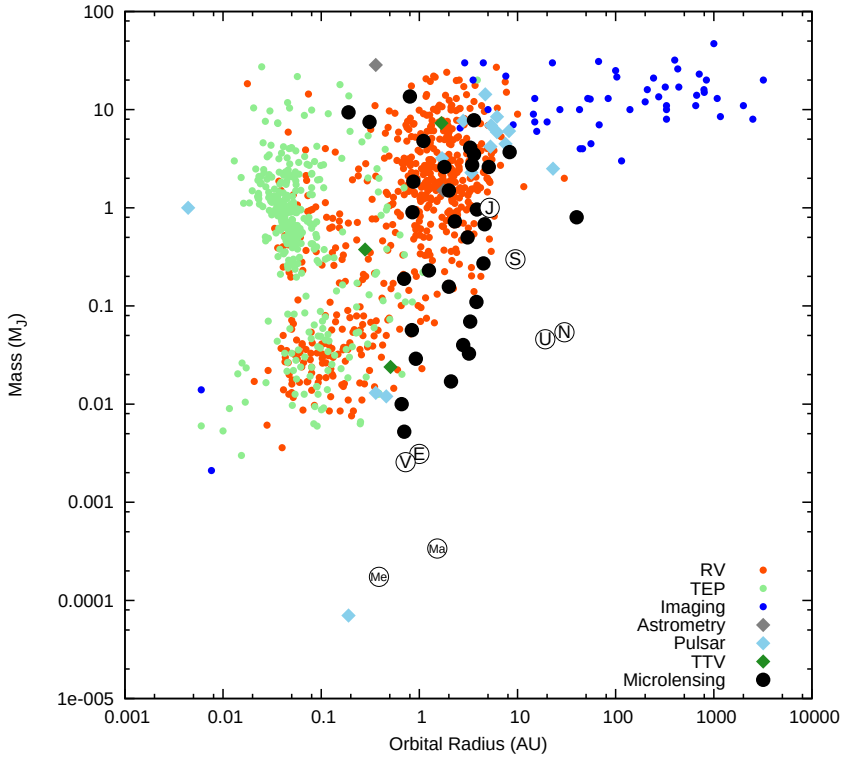

Figure 5.1: Demography of all the exoplanets discovered so far with different techniques and for which we have been able to characterise mass and orbital radius (Solar system planets are indicated with circled letters). The plot shows how exoplanets are distributed in a plane defined by planetary mass and the orbital radius (units are in Jupiter mass M_J and AU). It is clear how each technique is sensitive to a specific region of this parameter space. *From exoplanet.eu*

5.1 Transiting exoplanets

This method is based on the study of the lightcurve of a star hosting a planet. When the orbit of the planet intersects the stellar disk, the measured light undergoes a dimming with intensity and duration proportional to the duration of the transit and the projected size of the planet on the stellar surface (Figure 5.2).

Four kinds of "contacts" (Figure 5.3) are defined at different times: t_I is the time of "first contact", at which the planet projected surface touches the stellar disk; at t_{II}, the planet projected surface is completely "inside" the stellar disk; t_{III} is the time at which the planet begins the exit from the stellar disk; finally, at t_{IV} the transit is completed. Between t_I and t_{II} we can observe the so called *ingress*, while the egress goes from t_{III} to t_{IV}. The intensity of the flux drop is usually measured in mmag and indicated by the quantity δ which is called *transit depth*, while the duration of the transit is indicated by T and measures the duration between the middle

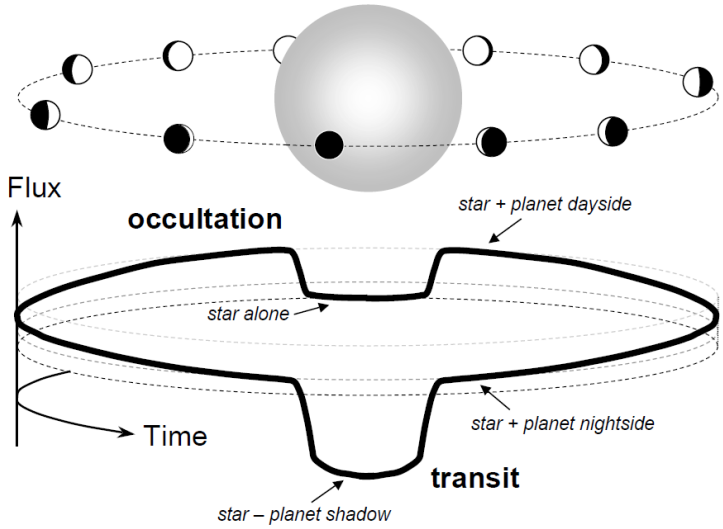

Figure 5.2: A transit occurs when the planet passes in the foreground, while occultation occurs when it passes in the background. The sketch shows the variation of the flux corresponding to both the phenomena. *From Winn (2011).*

point of the ingress and the middle point of the egress.

From the measurement of the time between two subsequent transits, one can have a direct measurement of the orbital period P of the planet around the host star. The study of the lightcurve gives the ratio k, between the radius R_p of the planet and the radius R_* of the star, which is proportional to the square root $\sqrt{\delta}$ of the transit depth. The lightcurve represents the combined flux of star and planet as a function of time, and can be written as

$$F(t) = F_*(t) + F_p(t) - k^2 \alpha_{tra}(t) F_*(t) \,, \tag{5.1}$$

with F_* and F_p the fluxes of star and planet, and α_{tra} a dimensionless function depending on the overlap between the stellar and planetary disks. The stellar flux F_* could be also affected by flares or star spots.

In the simplest case for which we can consider F_* to be a constant, if we define I_* and I_p as the stellar and planetary disk-averaged intensities, during the transit, the ratio $f(t) = F_p/F_* = k^2 I_p/I_*$ can be written, from Equation (5.1) as

$$f(t) = 1 + k^2 \left[\frac{I_p(t)}{I_*} - \alpha_{tra}(t) \right] \,, \tag{5.2}$$

where the time variation in I_p can be due to the fact that the fraction of stellar light reflected by the planet can change with its "phase", and also to intrinsic changes of the planetary atmo-

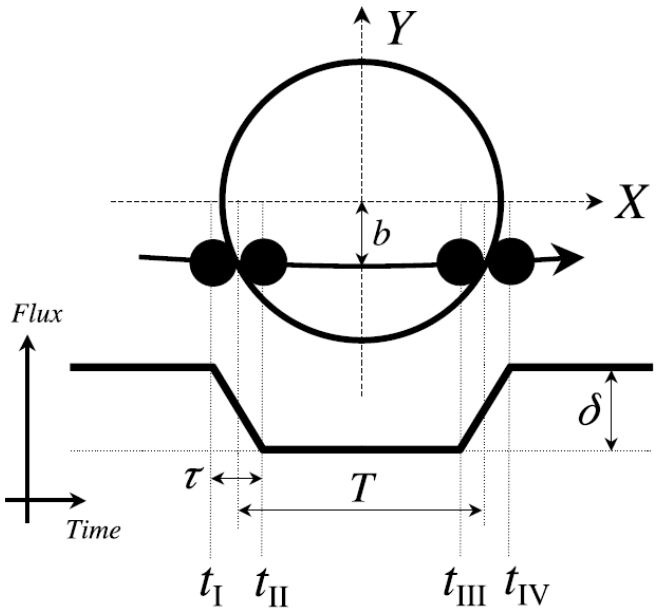

Figure 5.3: Observables of a transiting exoplanet. *From Winn (2011).*

sphere. In a good approximation, the maximum loss of light during a transit is

$$\delta_{tra} \approx k^2 \left[1 - \frac{I_p(t_{tra})}{I_*} \right] , \tag{5.3}$$

where the flux variation during the ingress and egress is considered linear in time. For a more rigorous derivation, we invite the reader to see Winn (2011) and Murray &Correia (2011).

5.1.1 Measuring physical parameters of transiting exoplanets

Except for direct measurement of P, from the lightcurve analysis one can infer constraints on mass and radius of the planet, or orbital radius and inclination. The relation between the planetary and the stellar radii comes from the depth of the transit, as we have seen in the last section: $k = R_p/R_* \approx \sqrt{\delta}$, so one needs more information on the host star, in order to find the radius R_p of the planet. In many cases the transit method works in close collaboration with radial velocity measurements. Particularly, with Doppler techniques we can measure K, the semi-amplitude of radial velocity, given by

$$K = \left(\frac{2\pi G}{P} \right)^{1/3} \frac{M_p \sin i}{(M_* + M_p)^{2/3}} \frac{1}{\sqrt{1-e^2}} , \tag{5.4}$$

where i is the inclination angle of the orbit, with respect to a normal plane to the line of sight, and e is the orbit eccentricity (another one of the RV method observables). Since a transit

Physical parameter	Symbol
Stellar mass	M_* $(M_\odot)$
Stellar radius	R_* $(R_\odot)$
Stellar surface gravity	$\log g_*$ (cgs)
Stellar density	ρ_* $(\rho_\odot)$
Planetary mass	M_p (M_J)
Planetary radius	R_p (R_J)
Planetary surface gravity	g_* (ms^{-2})
Planetary density	ρ_p (ρ_J)
Planetary equilibrium temperature	T_{eq} (K)
Orbital semimajor axis	a (au)

Table 5.1: Physical parameters and corresponding symbols.

is observable only when $\sin i \approx 1$, one can break the $M_p \sin i$ degeneracy in Equation (5.4) whenever is possible to perform transit observations in addition to RV measurements, gaining the relation existing between the mass of the planet and the mass of the hosting star:

$$\frac{M_p}{(M_* + M_p)^{2/3}} \approx \left(\frac{P}{2\pi G}\right)^{1/3} K \sqrt{1 - e^2}\,. \tag{5.5}$$

In order to determine the absolute dimensions of the planet, one still needs additional information about the host star such as luminosity or spectral type, which can be used to infer the mass M_*.

In the following section I will summarise the properties of some transiting exoplanets which I observed with the 1.54m Danish telescope located in La Silla (Chile) and the 1.52m Cassini telescope located in Loiano (Italy). The two telescopes mount a Faint Object Spectrograph and Camera (FOSC), respectively DFOSC and BFOSC. They were used both in photometry and spectrophotometry mode, in order to infer physical parameters and information on planetary atmospheres. Table 5.1 provides a guide to read the physical parameters tables which will follow.

5.1.2 HAT-P-16b

This is a Jovian planet discovered by Buchhave et al. (2010) and our observations led to improve the measurement of its physical parameters as summarised in Table 5.2.

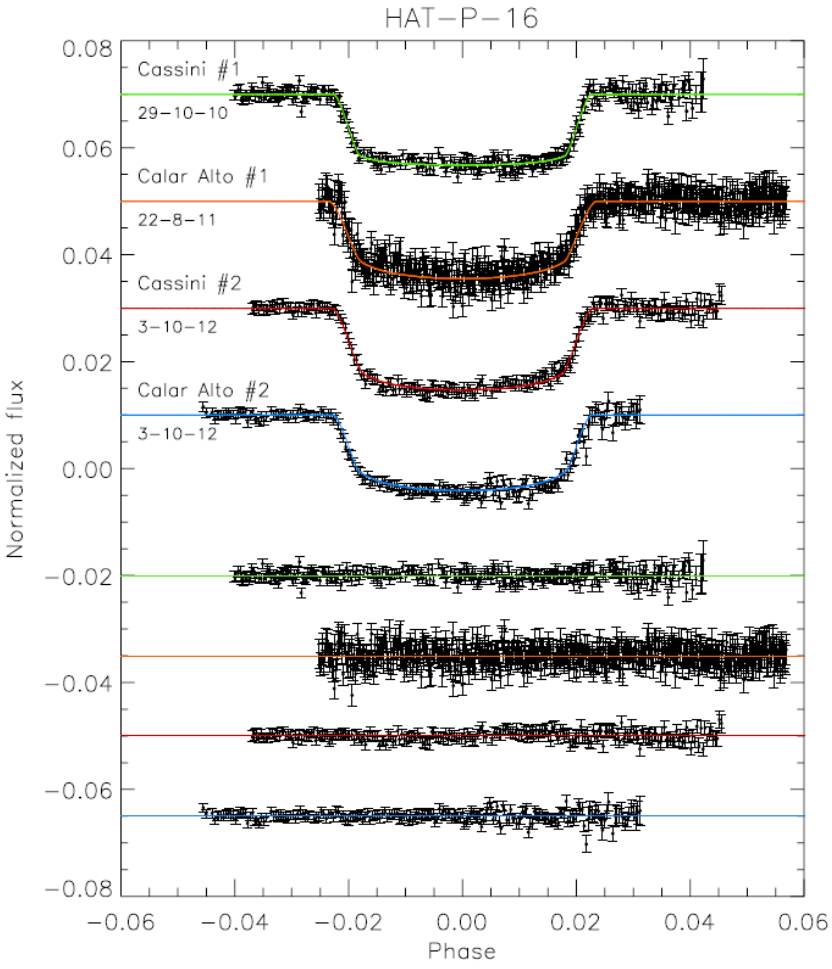

Figure 5.4: Lightcurves of HAT-P-16 fitted by the theoretical model obtained with JKTEBOP code. Four lightcuves observed at the Cassini telescope and Calar Alto telescope are shown. *From Ciceri et al. (2013).*

	Ciceri et al. (2013)	Buchhave et al. (2010)
M_* $(M_\odot)$	$1.216 \pm 0.042 \pm 0.036$	1.218 ± 0.039
R_* $(R_\odot)$	$1.158 \pm 0.023 \pm 0.011$	1.237 ± 0.054
$\log g_*$ (cgs)	$4.396 \pm 0.016 \pm 0.004$	4.34 ± 0.03
ρ_* $(\rho_\odot)$	0.784 ± 0.040	–
M_p (M_J)	$4.193 \pm 0.098 \pm 0.083$	4.193 ± 0.094
R_p (R_J)	$1.190 \pm 0.035 \pm 0.012$	1.289 ± 0.066
g_p (ms^{-2})	73.4 ± 4.1	63.1 ± 5.8
ρ_p (ρ_J)	$2.33 \pm 0.20 \pm 0.02$	1.95 ± 0.28
T_{eq} (K)	1567 ± 22	1626 ± 40
a (AU)	$0.04130 \pm 0.00047 \pm 0.00041$	0.0413 ± 0.0004
Age (Gyr)	$0.5^{+0.4+0.5}_{-0.5-0.5}$	2.0 ± 0.8

Table 5.2: HAT-P-16b: Comparison between the physical parameters measured by Ciceri et al. (2013) and the discovery paper by Buchhave et al. (2010).

5.1.3 WASP-21b

The radius of this planet is larger than the one measured in the discovery paper (Bouchy et al., 2010). Two possible explanations could be that the lower metallicity of the host star implies that the planet is composed by light elements, or that this was a more massive planet which lost mass and became a Neptune-like planet with a radius larger than 1 R_J.

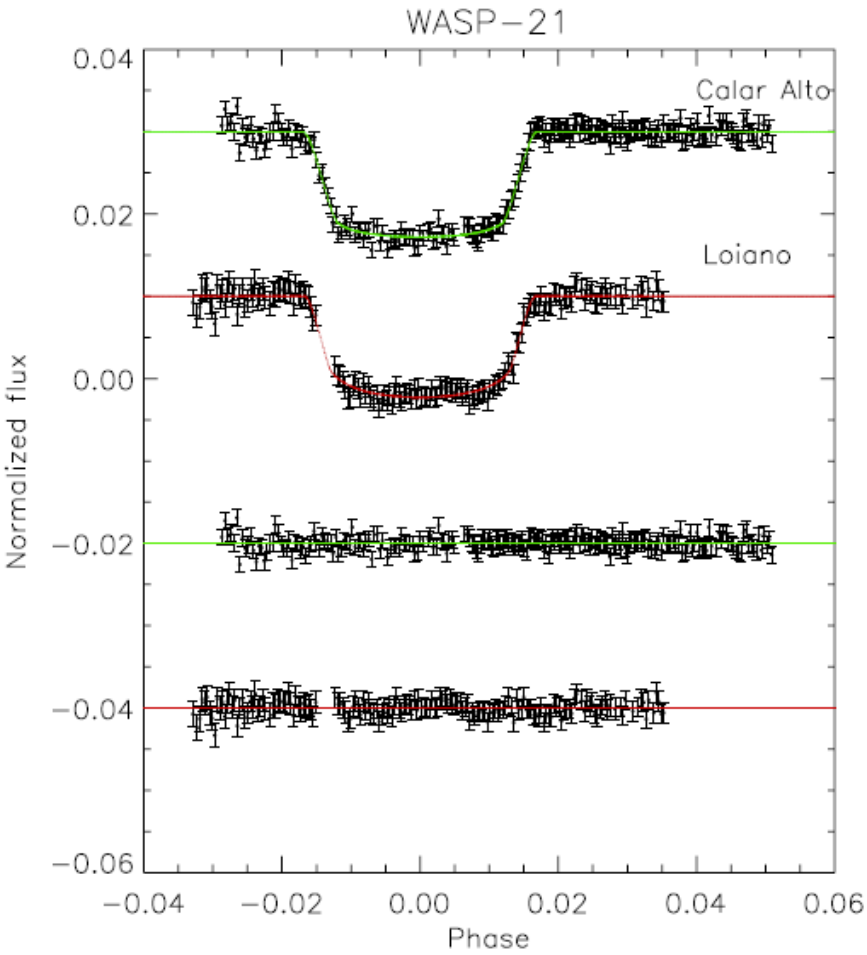

Figure 5.5: Lightcurves of WASP-21 fitted by the theoretical model attained with JKTEBOP code. Two lightcuves observed at the Cassini telescope and Calar Alto telescope are shown. *From Ciceri et al. (2013).*

	Ciceri et al. (2013)	Bouchy et al. (2010)
M_* ($M_\odot$)	$0.890 \pm 0.071 \pm 0.035$	1.01 ± 0.03
R_* ($R_\odot$)	$1.136 \pm 0.049 \pm 0.015$	1.06 ± 0.04
$\log g_*$ (cgs)	$4.277 \pm 0.025 \pm 0.006$	4.39 ± 0.03
ρ_* ($\rho_\odot$)	0.607 ± 0.048	0.84 ± 0.09
M_p (M_J)	$0.276 \pm 0.018 \pm 0.007$	0.300 ± 0.011
R_p (R_J)	$1.162 \pm 0.052 \pm 0.015$	1.07 ± 0.06
g_p (ms^{-2})	5.07 ± 0.35	–
ρ_p (ρ_J)	$0.165 \pm 0.018 \pm 0.002$	0.24 ± 0.05
T_{eq} (K)	1333 ± 28	–
a (AU)	$0.0499 \pm 0.0013 \pm 0.0007$	$0.052^{+0.00041}_{-0.00044}$
Age (Gyr)	–	12 ± 5

Table 5.3: WASP-21b: Comparison between the physical parameters measured by Ciceri et al. (2013) and the discovery paper by Bouchy et al. (2010).

5.1.4 WASP-80b

The transit of this planet was observed with 1.52m Danish telescope and ESO 2.2m telescope, both located at La Silla. The Gamma Ray burst Optical and Near-infrared Detector (GROND) mounted on ESO 2.2m telescope allowed to take measurements in four optical filters (*g'*, *r'*, *i'*, *z'*) simultaneously, and three NIR filters (J, H, K). The results are presented in the work by Mancini et al. (2014). Additional spectroscopic analysis had revealed that the star, WASP-80A, is at the border of the M class. The planet, WASP-80b, is a hot Jupiter. Interestingly, the spectroscopic analysis revealed that WASP-80A is one of the most active planet hosts known, with strong magnetic activity and the presence of starspots, although they are not affecting the lightcurve.

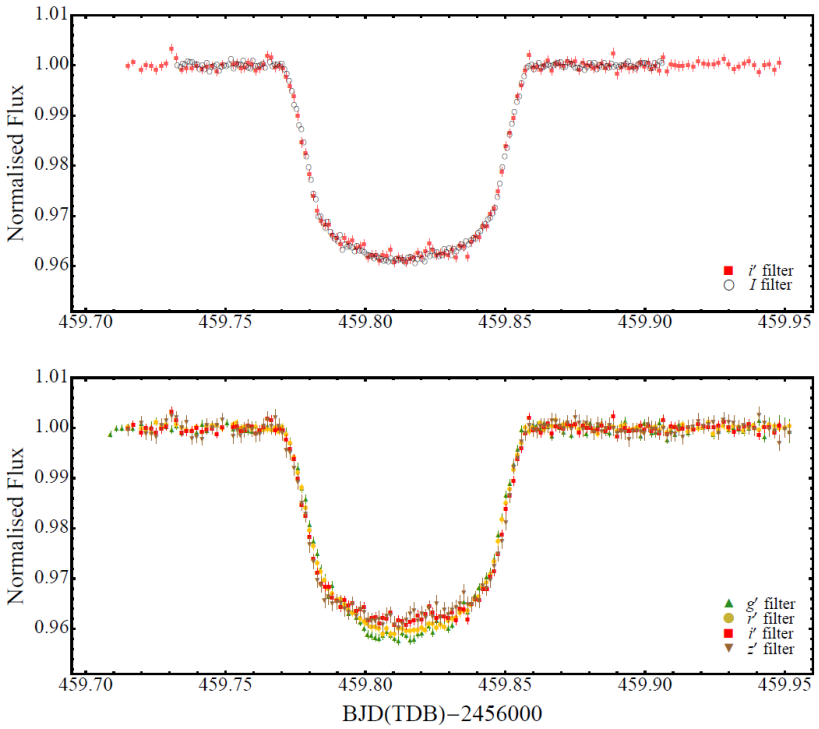

Figure 5.6: Lightcurves of WASP-80. The *top panel* shows the lightcurve taken at the 1.54m Danish telescope, while the *bottom panel* shows the lightcurves taken simultaneously in four pass-bands with GROND at the ESO 2.2m telescope. *From Mancini et al. (2014).*

	Mancini et al. (2014)	Triaud et al. (2013)
M_* $(M_\odot)$	$0.596 \pm 0.032 \pm 0.014$	$0.57^{+0.05}_{-0.05}$
R_* $(R_\odot)$	$0.593 \pm 0.011 \pm 0.005$	$0.571^{+0.016}_{-0.016}$
$\log g_*$ (cgs)	$4.6678 \pm 0.0077 \pm 0.0034$	$4.689^{+0.012}_{-0.013}$
ρ_* $(\rho_\odot)$	2.862 ± 0.050	$3.117^{+0.021}_{-0.020}$
M_p (M_J)	$0.562 \pm 0.025 \pm 0.009$	$0.554^{+0.030}_{-0.039}$
R_p (R_J)	$0.986 \pm 0.020 \pm 0.008$	$0.952^{+0.026}_{-0.027}$
g_* (ms^{-2})	14.34 ± 0.46	$15.07^{+0.45}_{-0.42}$
ρ_p (ρ_J)	$0.549 \pm 0.023 \pm 0.004$	$0.554^{+0.030}_{-0.039}$
T_{eq} (K)	825 ± 20	~ 800
a (au)	$0.03479 \pm 0.00062 \pm 0.00027$	$0.0346^{+0.008}_{-0.011}$

Table 5.4: WASP-80b: Comparison between the physical parameters measured by Mancini et al. (2014) and the discovery paper by Triaud et al. (2013).

5.1.5 WASP-67b

This system was observed with the 1.52m Danish telescope and the ESO 2.2m telescope. Multi-band observations were made using Sloan *g'*, *r'*, *i'*, *z'* filters on GROND, and Bessel R filter was used on DFOSC. The planet was discovered by Hellier et al. (2012). The results of our observations are presented in Mancini et al. (2014b), improving measurements of the radius and then inferring a higher density than the one measured in the discovery paper, and positioning this hot Jupiter planet in a different region of the mass-radius parameter space.

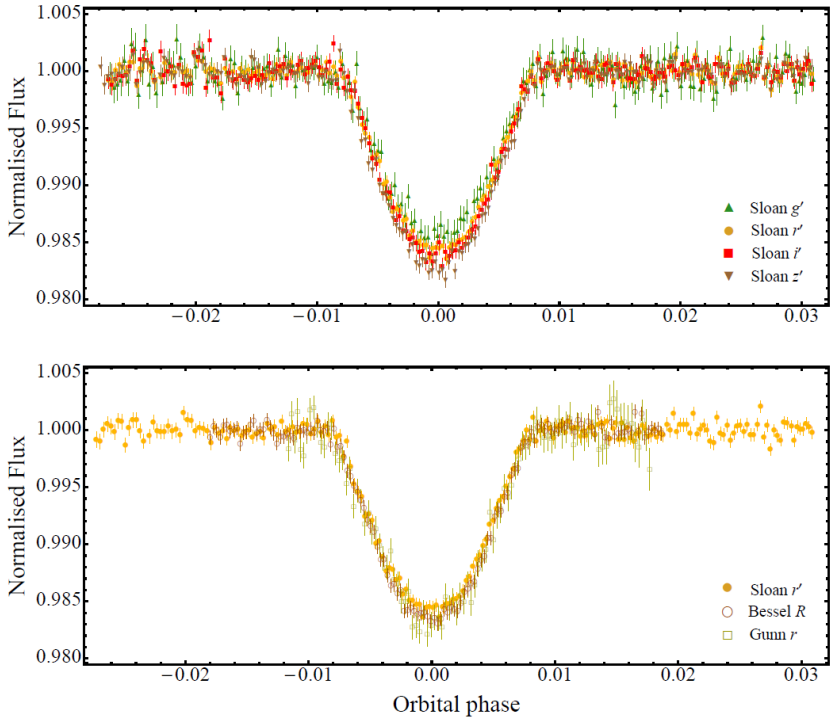

Figure 5.7: Lightcurves of WASP-67. The *top panel* shows the lightcurves simultaneously taken with GROND, while the *bottom panel* shows the lightcurves taken in Sloan-*r'* filter with GROND in previous observations, Bessel-R filter with DFOSC, and Gunn-*r* filter with the Euler 1.2m telescope at La Silla previously. *From Mancini et al. (2014b).*

	Mancini et al. (2014b)	Hellier et al. (2012)
M_* ($M_\odot$)	$0.829 \pm 0.050 \pm 0.037$	0.87 ± 0.04
R_* ($R_\odot$)	$0.817 \pm 0.019 \pm 0.012$	0.87 ± 0.04
$\log g_*$ (cgs)	$4.533 \pm 0.014 \pm 0.007$	4.50 ± 0.03
ρ_* ($\rho_\odot$)	1.522 ± 0.049	1.32 ± 0.15
M_p (M_J)	$0.406 \pm 0.033 \pm 0.012$	0.42 ± 0.04
R_p (R_J)	$1.091 \pm 0.043 \pm 0.016$	$1.4^{+0.3}_{-0.2}$
g_* (ms^{-2})	8.45 ± 0.83	$5.0^{+1.2}_{-2.3}$
ρ_p (ρ_J)	$0.292 \pm 0.036 \pm 0.004$	0.16 ± 0.08
T_{eq} (K)	1003 ± 20	1040 ± 30
a (au)	$0.0510 \pm 0.0010 \pm 0.0008$	0.0517 ± 0.0008
Age (Gyr)	$8.7^{+12.7+5.5}_{-7.3-8.6}$	$2.0^{+1.6}_{-1.0}$

Table 5.5: WASP-67b: Comparison between the physical parameters measured by Mancini et al. (2014b) and the discovery paper by Hellier et al. (2012).

5.1.6 WASP-24b, WASP-25b, and WASP-26b

WASP-24, WASP-25, and WASP-26 were observed at the 1.54m Danish telescope with DFOSC in two pass-bands (Bessel-*R* and -*I*). WASP-24b and WASP-26b are two hot Jupiter planets, while WASP 26b belongs to a cluster of planets with mass between 0.5 and 0.7 M_J, known as hot Saturns. The results are presented in Southworth et al. (2014).

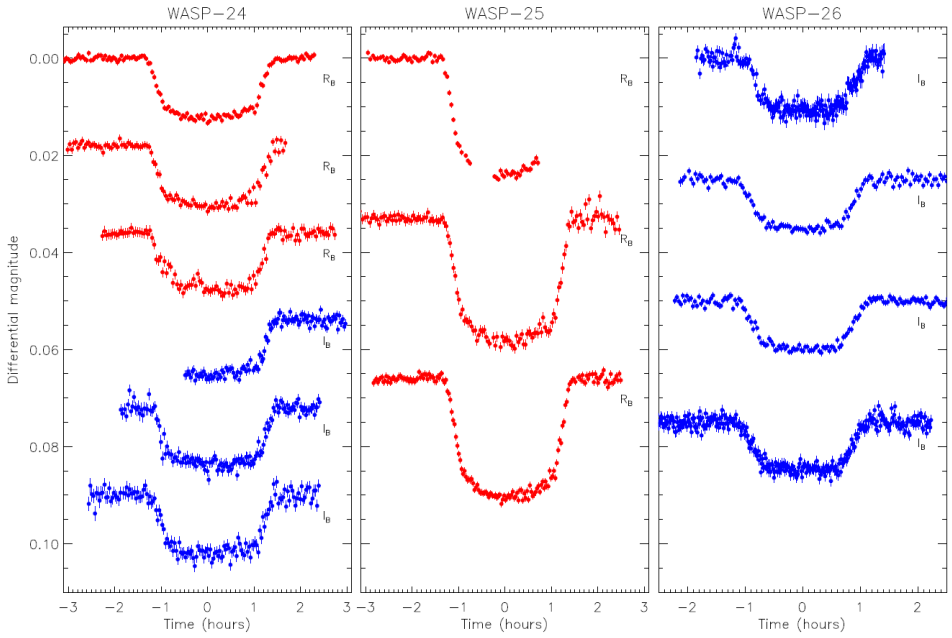

Figure 5.8: Lightcurves observed with DFOSC on 1.54m Danish telescope. The blue and red dots represent datasets in Bessel-*R* and -*I* filters, respectively. *From Southworth et al. (2014).*

	WASP-24b	WASP-25b	WASP-26b
M_* ($M_\odot$)	1.168 ± 0.056 ± 0.050	1.053 ± 0.023 ± 0.030	1.095 ± 0.043 ± 0.017
R_* ($R_\odot$)	1.317 ± 0.036 ± 0.019	0.924 ± 0.016 ± 0.009	1.284 ± 0.035 ± 0.007
log g_* (cgs)	4.267 ± 0.021 ± 0.006	4.530 ± 0.014 ± 0.004	4.260 ± 0.022 ± 0.002
ρ_* ($\rho_\odot$)	0.512 ± 0.034	1.336 ± 0.063	0.517 ± 0.037
M_p (M_J)	1.109 ± 0.043 ± 0.032	0.598 ± 0.044 ± 0.012	1.020 ± 0.031 ± 0.011
R_p (R_J)	1.303 ± 0.043 ± 0.019	1.247 ± 0.030 ± 0.012	1.216 ± 0.047 ± 0.006
g_* (ms^{-2})	16.19 ± 0.99	9.54 ± 0.80	17.1 ± 1.3
ρ_p (ρ_J)	0.469 ± 0.042 ± 0.007	0.288 ± 0.028 ± 0.003	0.530 ± 0.060 ± 0.003
T_{eq} (K)	1772 ± 29	1210 ± 14	1650 ± 24
a (au)	0.03635 ± 0.00059 ± 0.00052	0.04819 ± 0.00035 ± 0.00046	0.03966 ± 0.00052 ± 0.00021
Age (Gyr)	$2.5^{+9.6+1.8}_{-1.5-2.5}$	$0.1^{+5.7+0.2}_{-0.1-0.0}$	$4.0^{+5.7+1.4}_{-4.5-4.0}$

Table 5.6: Summary of the physical parameters for WASP-24b, WASP-25b, and WASP-26b measured by Southworth et al. (2014).

5.1.7 WASP-103b

This planet, discovered by Gillon et al. (2014), has been better characterised by Southworth et al. (2015) with observations taken with DFOSC and GROND. An additional lightcurve (which we are not showing here but can be found in Southworth et al. (2015)) was taken at the 2.15m Jorge Shade telescope located at the Complejo Astronómico El Leoncito in San Juan (Argentina). The very short orbital period (0.94 days) and small orbital radius ($\sim$ 0.02 au) make this planet particularly interesting for future studies on tidally-induced orbital decay. The planet has a Roche lobe filling factor of 0.58 and this leads to a significant asphericity. Values given in Table 5.7 for R_p and ρ_p suffer of a tidal correction of respectively +2.2% and 9.6%.

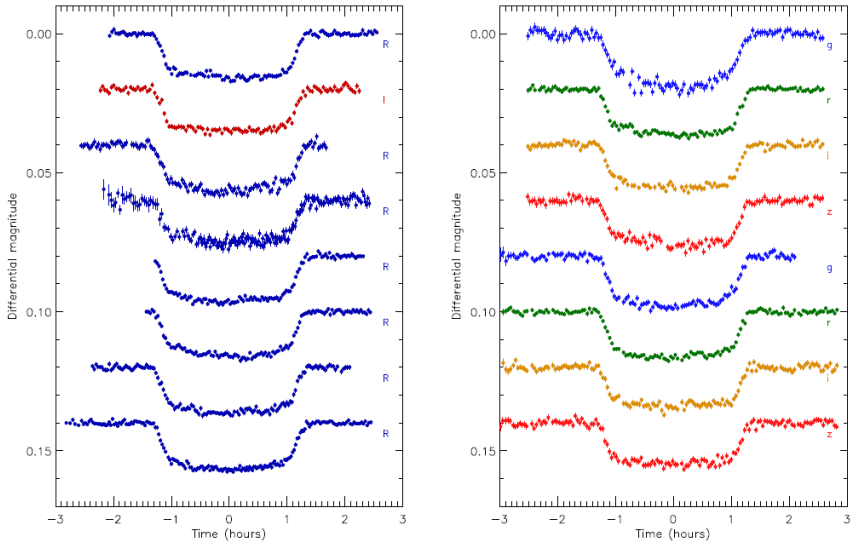

Figure 5.9: Lightcurves of WASP-103. The *left panel* shows the lightcurves taken with DFOSC, while the *right panel* shows the lightcurves taken with GROND. *From Southworth et al. (2015).*

	Southworth et al. (2015)	Gillon et al. (2014)
M_* ($M_\odot$)	$1.204 \pm 0.089 \pm 0.019$	$1.220^{+0.039}_{-0.036}$
R_* ($R_\odot$)	$1.419 \pm 0.039 \pm 0.008$	$1.436^{+0.052}_{-0.031}$
$\log g_*$ (cgs)	$4.215 \pm 0.014 \pm 0.002$	$4.22^{+0.12}_{-0.05}$
ρ_* ($\rho_\odot$)	0.421 ± 0.013	$0.414^{+0.021}_{-0.039}$
M_p (M_J)	$1.47 \pm 0.11 \pm 0.02$	1.490 ± 0.088
R_p (R_J)	$1.554 \pm 0.044 \pm 0.008$	$1.528^{+0.073}_{-0.047}$
g_* (ms^{-2})	15.12 ± 0.93	15.7 ± 1.4
ρ_p (ρ_J)	$0.367 \pm 0.027 \pm 0.002$	$0.415^{+0.046}_{-0.053}$
T_{eq} (K)	2495 ± 66	2508^{+75}_{-70}
a (au)	$0.01978 \pm 0.00049 \pm 0.00010$	0.01985 ± 0.00021
Age (Gyr)	$3.8^{+2.1+0.3}_{-1.6-0.4}$	$3to5$

Table 5.7: WASP-103b: Comparison between the physical parameters measured by Southworth et al. (2015) and the discovery paper by Gillon et al. (2014).

6

Discussion

"...angelheaded hipsters burning for the ancient heavenly connection
to the starry dynamo in the machinery of night..."
Howl - Allen Ginsberg

Since we have already presented the results and conclusions for the two main subjects of the thesis at the end of Chapters 2 and 4, we leave this short last chapter for some personal considerations on the work just described.

This thesis was inspired by two works, involving both the theoretical and the practical aspects of gravitational microlensing. Beside their scientific relevance, these works are the results of a fruitful collective job and gave me the opportunity of being introduced to the microlensing community and to take part in every single aspect of the exciting field of the search for exoplanetary systems. The results of both the morphology classification and the modelling of OGLE-2013-BLG-1394 have been presented to the annual microlensing international conference in Santa Barbara, CA (2013) and Annapolis, MD (2014) receiving a positive feedback from the community.

We have presented the first complete catalogue of equal-mass binary microlensing lightcurves with even final considerations about the theoretical occurence rate of each isopeak lightcurve. The results from this theoretical work have highlighted the complexity of a scenario which stems by the presence of only two deflectors. The classification required the use of heavy computational tools like the inverse ray shooting in order to simulate a huge number of lighcurves. Nevertheless it was necessary to carry out a very detailed work to look into and classify each iso-peak region. The immediate application of the work involves the real-time modelling, which is of crucial importance during the microlensing observing season, when we need to select, among the thousands of ongoing events, the most promising ones aiming at discovering exoplanets. The catalogue could then improve the efficiency of modelling codes.

My involvement was complete, since I have also carried out personally microlensing observations from different sites, having the opportunity of being part of big international collaborations. The main effort has certainly been lavished in the observations of OGLE-2103-BLG-1394 with the 0.35m Salerno University Observatory telescope and with the 1.54m Danish telescope at La Silla in Chile. I followed this target for the entire duration of the microlensing event and I had the opportunity of leading the modelling of one of the most puzzling events of that season, which lasted until 2014. Unfortunately, the MCMC modelling did not bring to the discovery of a new planetary system, as we were hoping along the course of the season, but anyway it brought to an interesting discussion on the contamination of microlensing events by the presence of binary sources and we are confident to present the results in a scientific paper very soon.

I personally developed the contour integration code for simulating the numerous lightcurves used as examples in this thesis. Together with the morphological classification, the development of a contour integration code which can reproduce binary and triple lens microlensing lightcurves has been of great relevance in order to understand the physics of the phenomenon and has been of great inspiration for developing new useful ideas during my scientific investigation.

As a last remark, we can remind the importance of searching for exoplanets with different techniques, in order to find planets in zones outside the sensitivity range of microlensing. Transiting exoplanets have also been treated in this work, by a brief report of the observations carried out as parallel projects.

Since we have treated microlensing since its dawn until the last observing seasons and in some sense we have depicted all the stages of the scientific work of a “microlenser” who is hunting for new Earths, even mentioning the parallel fields and methods for achieving this fascinating task, we can consider the purpose of making an insight into microlensing and the search for exoplanetary systems concluded and I can dare to define the complete achievement of my personal goals.

Bibliography

Abt, H. A. (1983), *ARA&A*, **21**, 343. 56

Albrow M. D., Beaulieu J.-P., Caldwell J. A. R., DePoy D. L., Dominik M., Gaudi B. S., Gould A., Greenhill J., Hill K., Kane S., Martin R., Menzies J., Naber R. M., Pogge R. W., Pollard K. R., Sackett P. D., Sahu K. C., Vermaak P., Watson R., Williams A., and PLANET Collaboration, (1999), *ApJ*, **522**, 1022–1036. 20

Bouchy, F., Hebb, L., Skillen, I., et al. (2010), *A&A*, **519**, AA98. 99, 100

Bozza V. (2010), *MNRAS*, **408**, 2188. 16

Buchhave, L. A., Bakos, G. Á., Hartman, J. D., et al. (2010), *ApJ*, **720**, 1118. 97, 98

Calchi Novati, S., Gould, A., Udalski, A., et al. (2014), arXiv:1411.7378. 68

Ciceri, S., Mancini, L., Southworth, J., et al. (2013), *A&A*, **557**, AA30. 97, 98, 99, 100

Di Stefano R., Perna R., (1997), *ApJ*, **488**, 55. 20

Dominik M., Hirshfeld A. C., (1996), *A&A*, **313**, 841. 20

Dominik M., (1999a), *A&A*, **341**, 943. 20

Dominik M., (1999b), *A&A*, **349**, 108. 11, 12

Dominik, M., Rattenbury, N. J., Allan, A., et al. (2007), *MNRAS*, **380**, 792 66

Dominik, M. (2009), *MNRAS*, **393**, 816 69

Dominik, M. (2010), *General Relativity and Gravitation*, **42**, 2075 56, 69

Dominik, M., Jørgensen, U. G., Rattenbury, N. J., et al. (2010), *Astronomische Nachrichten*, **331**, 671 66

Dyson, F. W., Eddington, A. S., & Davidson, C. (1920), *Royal Society of London Philosophical Transactions Series A*, **220**, 291. 2

Eddington, A. S. (1919), *The Observatory*, **42**, 119. 2

Eddington, A. S., Jeans, J. H., Lodge, O., Sir, et al. (1919), *MNRAS*, **80**, 96. 2

Einstein, A. (1911), *Annalen der Physik*, **340**, 898. 2

Einstein, A. (1916), "Die Grundlage der allgemeinen Relativitätstheorie", *Annalen der Physik*, **354**, 769. 1, 2

Einstein, A. (1936), *Science*, **84**, 506 6

Erdl, H., & Schneider, P. (1993), *A&A*, **268**, 453. 12

Gaudi, B. S. (2011), Exoplanets, edited by S. Seager. Tucson, AZ: University of Arizona Press, 2011, 526 pp. ISBN 978-0-8165-2945-2., p.79-110, 79. 69

Gillon, M., Anderson, D. R., Collier-Cameron, A., et al. (2014), *A&A*, **562**, LL3. 107, 108

Griest, K. (1991), *ApJ*, **366**, 412.

Han C. & Gaudi, B. S. (2008), *ApJ*, **689**, 53–58. 20

Hellier, C., Anderson, D. R., Collier Cameron, A., et al. (2012), *MNRAS*, **426**, 739. 103, 104

Ingrosso, G., Calchi Novati, S., De Paolis, F., et al. (2012), *MNRAS*, **426**, 1496 67

Kayser, R., Refsdal, S., & Stabell, R. (1986), *A&A*, **166**, 36. 15

Liebig C., (2014), PhD thesis, University of St Andrews 30

Liebig, C., D'Ago, G., Bozza, V., & Dominik, M. (2015), arXiv:1501.02219 (*in press on MNRAS*). 20, 46

Lodge, O. J., (1919), "Gravitation and Light", *Nature*, **104**, 354. 1

Mancini, L., Southworth, J., Ciceri, S., et al. (2014), *A&A*, **562**, AA126 101, 102

Mancini, L., Southworth, J., Ciceri, S., et al. (2014), *A&A*, **568**, AA127 103, 104

Mao S., Paczyński B., (1991), *ApJ*, **374**, L37-L40. 56

Mao S., Di Stefano R., (1995), *ApJ*, **440**, 22. 20

Mao, S., Witt, H. J., & An, J. H. (2014), *MNRAS*, **437**, 1554.

Marnach, S. (2010), *https:github.comsmarnachluckylensing*. 16, 28

Mollerach, S., & Roulet, E. (2002), "Gravitational lensing and microlensing" *World Scientific*. 6, 8

Moon, H.-K., Choi, Y.-J., Ishiguro, M., et al. (2011), *EPSC-DPS Joint Meeting 2011*, **1697** 65

Murray, C. D., & Correia, A. C. M. (2011), "Exoplanets", edited by S. Seager. Tucson, AZ: University of Arizona Press, 2011, 526 pp. ISBN 978-0-8165-2945-2., p.15-23, 15. 95

Night C., Di Stefano R., Schwamb M., (2008), *ApJ*, **686**, 785. 20

Paczyński, B., (1986), "Gravitational microlensing by the Glactic halo", *ApJ*, **304**, 1-4. 5, 55

Paczyński B., (1991), *ApJ*, **371**, L63-L67. 55

Petters, A. O., Levine, H., & Wambsganss, J. (2001), "Singularity theory and gravitational lensing", Birkhäuser, Boston, (*Progress in mathematical physics; v. 21*). 8

Rhie, S. H (2002), "How Cumbersome is a Tenth Order Polynomial?: The Case of Gravitational Triple Lens Equation", http://arxiv.org/abs/astro-ph/0202294. 15

Rhie, S. H (2003), "n-point Gravitational Lenses with 5(n-1) Images", http://arxiv.org/abs/astro-ph/0305166. 15

Sako, T., Sekiguchi, T., Sasaki, M., et al. (2008), *Experimental Astronomy*, **22**, 51 65

Schneider, P., & Weiss, A. (1986), *A&A*, **164**, 237.

Schneider, P., Ehlers, J., & Falco, E. E. (1992), "Gravitational Lenses", Springer-Verlag Berlin Heidelberg New York. 8

Soldner, J. (1801), "Über die Ablenkung eines Lichtstrahls von seiner geradlinigen Bewegung durch die Attraktion eines Weltkörpers, an welchem er nahe vorbeigeht", *Berliner Astronomisches Jahrbuch*, **1804**, 161-172. 2

Southworth, J., Hinse, T. C., Burgdorf, M., et al. (2014), *MNRAS*, **444**, 776. 105, 106

Southworth, J., Mancini, L., Ciceri, S., et al. (2015), *MNRAS*, **447**, 711. 107, 108

Triaud, A. H. M. J., Anderson, D. R., Collier Cameron, A., et al. (2013), *A&A*, **551**, AA80. 102

Valls-Gabaud, D. (2006), *Albert Einstein Century International Conference*, **861**, 1163. 2

Winn, J. N. (2011), "Exoplanets", edited by S. Seager. Tucson, AZ: University of Arizona Press, 2011, 526 pp. ISBN 978-0-8165-2945-2., p.55-77, 55. 94, 95

Witt, H. J. (1990), *A&A*, **236**, 311. 8, 9

Witt, H. J., & Mao, S. (1995), *ApJ*, **447**, L105. 9

Wolszczan, A., & Frail, D. A. (1992), *Nature*, **355**, 145 92

Woźniak, P., & Paczyński, B. (1997), *ApJ*, **487**, 55. 69

Wyrzykowski, Ł., Kostrzewa-Rutkowska, Z., Kozłowski, S., et al. (2014), *Acta Astron.*, **64**, 197 65

Yee, J. C., Han, C., Gould, A., et al. (2014), *ApJ*, **790**, 14.